NTNU
Norwegian University of
Science and Technology

University of Padua

Department of Industrial Engineering

Master Thesis in Electrical Engineering

Wave-to-Wire Model of a Wave Energy Converter equipped with an All-Electric Power Take-Off

Supervisor: Prof. Nicola Bianchi (UNIPD)

Co-Supervisor: Prof. Elisabetta Tedeschi (NTNU)

Majoring: Gabriele Casagranda

ACADEMIC YEAR 2014-2015

Problem description

Wave-to-Wire Model of a Wave Energy Converter equipped with an All-Electric Power Take-Off.

The purpose of the thesis will be to develop a detailed wave-to-wire model of a point absorber wave energy converter (WEC) with grid connection. The tool for carrying out the work will be MATLAB-Simulink. The first part of the project will be to test three representative energy sea states (low, medium and high respectively) using the passive loading control strategy in order to find the maximum attainable power from the waves. After which several constraints will be tested with the goal to reduce the size of the PTO (power take-off). An electrical machine driven by an ideal inverter will be chosen and subsequently the detailed wave-to-wire model of the point absorber WEC will be tested for each representative energy sea state. The corresponding average efficiency will be then calculated. The final part of the project includes the grid connection of the detailed wave-to-wire model with another inverter interfacing the DC-link with the grid side. The grid connection issues will be considered and the injection into the grid of only active power proved. The implementation of the simulations will be tested under irregular waves.

Assignment given: 05 March 2014
Supervisor: Nicola Bianchi, UNIPD
Co-Supervisor: Elisabetta Tedeschi, NTNU

Abstract

This thesis is focused to the production of electric energy by the sea waves. The point absorber WEC (wave energy converter) adopted has the same hydrodynamics characteristics of the one analysed in the following paper "Effect of the generator sizing on wave energy converter" [14]. The MATLAB-Simulink is the software used to implement the models and to run the simulations of the thesis. The passive loading control is the control strategy adopted to allow the power extraction from the sea and three representative energy sea state are tested, representing low, medium and high energy sea conditions. In the first part of the thesis an ideal generator without losses (with the electrical power equal to the mechanical power) is considered in the model. Because at the beginning the goal is to find the damping coefficient ($\boldsymbol{B_L}$) for each energy sea state, that gives the maximum average mechanical power, and other parameters like the maximum power and the maximum torque useful for the sizing of the electrical machine. Therefore several power limits are tested in order to reduce the size of the power take-off (hence the investment) and the peak to average power ratio.

Based on these preliminary studies, the most reasonable sizing for the PTO (power take-off) is selected, in order to proceed to the design and performance analysis of the electrical machine and power electronic interface. In accordance with the results obtained in the first part of the thesis, a permanent magnet synchronous generator (PMSG) with a high over-speed ratio and a wide constant power region is used. In the model also the torque limit, which corresponds to the maximum torque of the electrical machine, is applied. The generator works most of the time during the simulation in the field-weakening operation region and therefore a field-weakening control is made. An electric drive model (with an ideal three phase inverter) is implemented to control the torque of the generator. Then the wave-to-wire model of the point absorber WEC (up to the DC link) is tested for each energy sea state. The losses of the generator are calculated through a real time-model and with them the average efficiency obtained during the time of simulation. At this point a precise evaluation of the average electrical power produced by the considered WEC for each energy sea state is made.

The last part of the thesis regards the grid connection of the wave-to-wire model of the point absorber WEC. An inverter, a capacitor on the DC-link (between the two inverter) and a filter on the grid side of the converter are added to the model. The control strategy implemented for the grid connection does not involve the exchange of reactive power with the grid and the injection of grid current is made at the grid frequency. Furthermore, the power generated by the PTO is directly injected into the grid (the DC link voltage is maintained nearly constant). The control strategy

implemented is called voltage oriented vector control and it has been already used in a variety of applications. The grid connection of the wave-to-wire model of the WEC is tested for several seconds for one energy sea state. Hence the trends over the time of the most important electrical quantities of the system are plotted and analysed.

Sommario

Questa tesi è focalizzata sulla produzione di energia elettrica dalle onde del mare. Il WEC (wave energy converter) punto assorbitore adottato ha le stesse caratteristiche idrodinamiche di quello analizzato nel seguente articolo “Effect of the generator sizing on wave energy converter” [14]. MATLAB-Simulink è il programma utilizzato per implementare i modelli e per eseguire le simulazioni della tesi. Il passive loading control è la strategia di controllo adottata per consentire l'estrazione di potenza dal mare e tre rappresentativi stati di mare di energia sono testati, rappresentando la bassa, media e alta condizione di energia del mare. Nella prima parte della tesi un generatore ideale senza perdite (con la potenza elettrica pari alla potenza meccanica) è considerata nel modello. Poiché all'inizio l'obiettivo è di trovare il coefficiente di smorzamento ($\boldsymbol{B_L}$) per ogni stato del mare di energia, il quale dà la massima potenza meccanica media, e altri parametri come la massima potenza e la massima coppia utili per il dimensionamento della macchina elettrica. Pertanto diversi limiti di potenza sono testati per ridurre le dimensioni del power take-off (quindi l'investimento) e il rapporto tra la potenza massima e la potenza media.

Sulla base di questi studi preliminari il dimensionamento più ragionevole per il PTO (power take-off) è selezionato, al fine di procedere alla progettazione e all’analisi delle prestazioni della macchina elettrica e dell’elettronica di potenza. In accordo con i risultati ottenuti nella prima parte della tesi, viene utilizzato un generatore sincrono a magneti permanenti (PMSG) con un elevato rapporto tra la velocità massima e velocità nominale ed un’ampia regione a potenza costante. Nel modello è anche applicato il limite di coppia corrispondente alla coppia massima della macchina elettrica. Il generatore funziona la maggior parte del tempo durante la simulazione nella regione di funzionamento di indebolimento di campo, per cui viene effettuato un controllo in field-weakening. Il modello di un azionamento elettrico (con un ideale inverter trifase) è implementato per controllare la coppia del generatore. In seguito il modello da onda a filo del WEC punto assorbitore (fino al DC link) viene testato per ogni stato del mare di energia. Le perdite del generatore sono calcolate attraverso un modello in tempo reale e con esse il rendimento medio ottenuto durante il tempo di simulazione. A questo punto viene fatta una valutazione precisa della potenza elettrica media prodotta dal WEC preso in considerazione per ogni stato di mare di energia.

L'ultima parte della tesi riguarda il collegamento in rete del modello da onda a filo del WEC punto assorbitore. Un inverter, un condensatore sul DC link (tra i due inverter) e un filtro sul lato rete del convertitore vengono aggiunti al modello. La strategia di controllo implementata per il collegamento alla rete non comporta lo

scambio di potenza reattiva con la rete e l'iniezione della corrente viene effettuata alla frequenza di rete. Inoltre, la potenza generata dal PTO viene iniettata direttamente in rete (la tensione del DC link è mantenuta pressoché costante). La strategia di controllo implementata è chiamata voltage oriented vector control ed è già stata utilizzata in una varietà di applicazioni. Il collegamento alla rete del modello da onda a filo del WEC viene testato per alcuni secondi per uno stato di mare di energia. Quindi gli andamenti in funzione del tempo, delle più importanti grandezze elettriche del sistema, sono tracciati e analizzati.

Preface

This is my master thesis and hence my final work of the Master of Science in Electrical Engineering at the University of Padua. This project has been made during my Exchange Erasmus program of 9 months at the Norwegian University of Science and Technology (NTNU) in Trondheim (Norway).

I would like to thank my Supervisor Nicola Bianchi, for the availability and the opportunity given to me to go in Norway, and my Co-Supervisor Elisabetta Tedeschi for all the time that she spent for me, helping me and giving to me advice during my permanence in Trondheim.

A special thanks go to my family, which supported me and gave to me help in situations of difficulty in all of my years at the university, and to my girlfriend Silvia for the precious time spent together and the support given to me in the last year despite the distance.

Finally, I would like to thank all the people who supported and helped me during these years at the university, especially my friends.

Gabriele

Contents

List of Figures

List of Tables

Nomenclature

K	[N/m]	Hydrostatic stiffness
K_{rad}	[-]	Radiation impulse response function
S_{ζ}^{B}	[-]	Bretschneider spectrum
$\dot{s}$	[m/s]	Buoy speed
$\ddot{s}$	[m/s^2]	Buoy acceleration
ψ_m	[deg]	Phase margin
$\langle h_{0,vc}$	[deg]	Phase of the open loop transfer function (outer voltage controller)
$2p$	[-]	Poles number
a	[-]	Constant of the phase margin
A, B	[-]	Definition parameters
a, b, c	[-]	Field weakening coefficients
a_{∞}	[kg]	Added mass at infinite frequency
B	[T]	Magnetic flux density
B_L	[kg/s]	Added damping
C	[F]	Capacity of the DC link capacitor
c	[-]	Mechanical constant
$cos\varphi$	[-]	Load factor
f	[Hz]	Frequency
F_E	[N]	Excitation force
F_L	[N]	PTO force
g	[m/s^2]	Gravity constant
G_{CL}	[-]	Closed loop transfer function
G_{OL}	[-]	Open loop transfer function
h, Hs	[m]	Wave amplitude
$h_{0,cc}$	[-]	Open loop transfer function (current controller)
$h_{0,vc}$	[-]	Open loop transfer function (outer voltage controller)
I, i	[A]	Current
J	[-]	Inverter time delay transfer function
k_e	[-]	Eddy current constant
k_h	[-]	Hysteresis constant
k_i	[-]	PI regulator integral term
k_{iv}	[-]	PI regulator integral term (outer voltage controller)
k_p	[-]	PI regulator gain
k_{pv}	[-]	PI regulator gain (outer voltage controller)
L	[H]	Stator leakage inductance
L_f	[H]	Filter inductance

M	[kg]	Mass
$M_{0,cc}$	[-]	Closed loop transfer function (current controller)
$maxF_L$	[kN]	Maximum PTO force in module
M_L	[kg]	Reactive component
n	[rpm]	Generator speed
p	[-]	Pole pairs number
P, p	[kW]	Power
Q	[VAR]	Reactive power
R	[Ω]	Stator resistance
R_f	[Ω]	Filter resistance
s	[m]	Buoy position
S	[VA]	Apparent power
T	[Nm]	Torque
t	[s]	Time
Te	[s]	Energy period
T_{eq}	[s]	Equivalent time constant of the closed loop current controller transfer function
T_i	[s]	PI regulator time constant
T_{iv}	[s]	PI regulator time constant (outer voltage controller)
T_s	[s]	Inverter switching time delay
Tz	[s]	Zero crossing period
V, v	[V]	Voltage
$Volume$	[m^3]	Iron machine volume
β	[-]	Steinmetz constant
η	[-]	Efficiency
θ	[deg]	angle
ξ	[-]	Relative damping coefficient
ρ	[kg/m^3]	Water density
τ	[s]	Time constant of the generator system
τ	[s]	Time shift
τ	[s]	Time constant of the grid side system
Ψ_{pm}	[Vs]	Permanent magnet flux
ω	[rad/s]	Angular frequency
ω_0	[1/s]	Undamped resonance frequency
ω_c	[rad/s]	Crossover frequency
ω_e	[rad/s]	Electromechanical speed
ω_m	[rad/s]	Mechanical speed

1. INTRODUCTION

1.1 Ocean energy

Oceans cover 70 percent of the earth's surface and represent an enormous amount of energy in the form of wave, tidal marine current and thermal resources. Though ocean energy is still in a development stage, researchers are seeking ways to capture that energy and convert it to electricity. Marine technology was once considered too expensive to be a viable source of alternative clean energy, especially compared to already developed products such as wind and solar. However, with the increased price of oil and the issues of global warming and national security, the countries in the world are looking to add ocean energy to their renewable energy portfolios. There are two primary types of ocean energy: mechanical and thermal. The rotation of the earth and the moon's gravitational pull create mechanical forces. The rotation of the earth (not only the heat of the sun) creates wind on the ocean surface that forms waves, while the gravitational pull of the moon creates coastal tides and currents. Thermal energy is derived from the sun, which heats the surface of the ocean while the depths remain colder. This temperature difference allows energy to be captured and converted to electric power.

At the end of the 18th century people started to be fascinated with capturing ocean energy. In 1799 Monsieur Girard made a ship attached to shore with waves driving pumps and other machinery [1]. This device is the first recorded patent for wave energy conversion. After Girard there have not been developments, but only occasional attempts to harness the ocean's energy until the late 1960's. However, in 1966, the largest tidal power station in the world was built in St. Malo (France). This ocean tidal power station produces 240 MWh each year [1]. In 1973 an oil shortage crisis occurred. The year after an engineer from Scotland, Stephen Salter, took the first steps to develop an ocean-wave generator known as Salter's Duck. The duck moves up and down with wave motion and a turbine converts this movement to electrical energy. Typical dimensions for a single 2 MW Duck were 10 to 15 m stern diameter and 20 to 30 m wide (designed to match the North Atlantic conditions) [9]. The Salter Duck never made it to production (the initial cost of wave power was considered too high). The search for alternative energy resources is once again on the forefront, mainly because the fossil fuel prices are increasing and are expected to stay high in the future. In the past few years a growing interest emerged in ocean energy. The progress is being made to bring ocean energy technologies from development stages to the commercial market.

1.1.1 Technology Types

Four types of ocean energy conversion exist: wave energy, tidal energy, marine current energy and ocean thermal energy conversion. Ocean energy has great potential as a renewable energy resource: table 1 provides a summary of estimated ocean power resources [1].

table 1- Summary of estimated ocean power resources

Form of Ocean Energy	Estimated Global Resource (TWh/yr)
Tides	300+
Waves	80000
Tidal (marine) current	800+
Thermal gradient	10000

The estimated global resource of ocean energy is almost 2/3 of the world energy consumption that is around 151000 TWh/yr [2].

Wave energy: is generated by the movement of a device either floating on the surface of the ocean or moored to the ocean floor. Many different techniques for converting wave energy to electric power have been studied. Wave energy is proving to be the most commercially advanced of the ocean energy technologies with a number of companies competing for the lead. This kind of energy and the different types of converters will be explained and analyzed in the next chapters.

Tidal Energy: is due to the gravitational force of the moon and has a cycle that occurs every 12 hours. The difference in water height from low tide and high tide is potential energy. Tidal energy is similar to traditional hydropower generated from dams. The water can be captured in a barrage across an estuary during high tide and forced through a hydro-turbine during low tide. There are only approximately 20 locations on earth where is possible to capture sufficient power from the tidal energy potential (the height of the high tide must be at least 5 meters greater than low tide). The Bay of Fundy between Maine (USA) and Nova Scotia (Canada) - has the potential to produce 10 GW (there are the highest tides in the world, reaching 17 meters) [1].

Current energy: is ocean water moving in one direction. Tides also create currents that flow in two directions. The kinetic energy of - the Gulf Stream (a noted current) and of other tidal currents can be captured with submerged turbines that are very similar in appearance to miniature wind turbines. The constant movement of the marine current moves the rotor blades to generate electric power.

Ocean Thermal Energy Conversion (OTEC): uses ocean temperature differences from the surface to depths lower than 1000 meters, to extract energy (a temperature difference of only 20 °C can yield usable energy) [1]. There are two types of OTEC technologies to extract thermal energy and convert it to electric power: closed cycle

and open cycle. The first one uses a working fluid (such as ammonia) that is pumped through a heat exchanger and vaporized. The vaporized steam runs a turbine. The cold water found at the depths of the ocean condenses the vapor back to a fluid where it returns to the heat exchanger. In the open cycle system: the warm surface water is pressurized in a vacuum chamber and converted to steam to run the turbine. The steam is then condensed using cold ocean water from lower depths.

1.2 Wave Energy

Wave energy is derived from the winds as they blow across the oceans, and this energy transfer provides a convenient and natural concentration of wind energy in the waves. Once created, waves can travel thousands of kilometres with little energy loss. The power in a wave is proportional to the square of the amplitude and to the period of the motion. Therefore, long period (~7-10 s), large amplitude (~2m) waves have energy fluxes commonly averaging between 40 and 70 kW per meter width of oncoming wave [3]. Nearer the coastline the average energy intensity of a wave decreases due to interaction with the seabed. Energy dissipation in near shore areas can be compensated for by natural phenomena such as refraction or reflection, leading to energy concentration ('hot spots'). The wave power, of regular waves, under a wave crest 1 meter wide is given by [10]:

$$\boldsymbol{P = \frac{\rho g^2 h^2 T}{64\pi}} \quad [\boldsymbol{W/m}] \tag{1}$$

In the previous formula $\boldsymbol{\rho}$ is the water density in kg/m^3, $\boldsymbol{g}$ is the gravity constant, $\boldsymbol{h}$ is the wave amplitude in meter and $\boldsymbol{T}$ is the energy period in second [4]. As mentioned in [5] "the wave energy level" is usually expressed as power per unit length (along the wave crest or along the shoreline direction); typical values for 'good' offshore locations (annual average) range between 20 and 70 kW/m and occur mostly in moderate to high latitudes. As it can be seen in figure 1, wave energy is distributed unevenly around the world like most forms of the renewable energy sources.

Figure 1- Wave Energy Levels in kW/m Crest Length [1]

Increased wave activity is found between the latitudes of approximately 30° and 60° on both hemispheres, induced by the prevailing western winds blowing in these regions [6]. The following regions offer the highest wave energy potentials over the globe: the Western European coast, the coasts of Canada and United States, and the southwestern coasts of Australia, New Zealand, South America, and South Africa.

Recent studies [3] quantify available wave power resources of about 290 GW (annual average of the power level) for the area of the north-eastern Atlantic, including the North Sea. The long-term annual power level increases from about 25 kW/m off the southernmost part of Europe's Atlantic coastline (Canary Islands) up to 75 kW/m off Ireland and Scotland. When moving further north it decreases to 30 kW/m off the northern part of the Norwegian coast. In the Mediterranean basin, the annual power level off the coasts of the European countries varies between 4 and 11 kW/m, the highest values occurring in the area of the south-western Agean Sea. This area is characterized by relatively long fetch and high wind potential. The entire annual deep-water resource along European coasts in the Mediterranean is the order of 30 GW, the total wave energy resource for Europe resulting thus to 320 GW (annual average of the power level) [3].

When comparing wave energy with other major renewable energy sources (wind energy and photovoltaic), its biggest advantage is that it offers the highest energy density. Also an important factor is that it represents a more constant and predictable energy source. Compared with the above mentioned renewable energy sources, the negative environmental impact is also noticeably less for wave energy. In addition, waves have a unique feature, i.e., they can travel large distances with - little energy loss (if they do not encounter head winds) [6]. It is also important to appreciate the difficulties facing the wave power developments (in particular in wave power extraction). The large variation ranges in wave amplitude, frequency, phase and

direction are an important difficulty. It is difficult to obtain maximum efficiency of a device over the entire range of excitation frequencies. In the event of extreme weather conditions (such as hurricanes) the structural loading may be as high as 100 times the average loading. The coupling of the irregular, slow motion (frequency ~ 0.1 Hz) of a wave to electrical generators requires typically ~500 times higher frequency [3]. It becomes apparent, that the design of a wave energy converter has to be highly sophisticated to be operationally efficient and reliable on the one hand, and economically feasible on the other. As with all renewable energy sources, the available resource and variability at the installation site has to be assessed first.

1.2.1 Wave energy converters

Over 1000 wave energy conversion techniques have been patented in Japan, North America, and Europe. Despite this large variation in design, WECs (wave energy converters) are generally categorized by location, type and modes of operation [7].

Based on the **location** WECs can be classified by shoreline devices, nearshore devices and offshore devices. The *shoreline devices* have the advantage of being close to the utility network, are easy to maintain, and, as waves are attenuated as they travel through shallow water, they have a reduced likelihood of being damaged in extreme conditions. This leads to one of the disadvantages of shore mounted devices, as shallow water leads to lower wave power. Another disadvantage is the tidal range that can also be an issue. In addition there are generally site specific requirements including shoreline geometry and geology, and preservation of coastal scenery, so devices cannot be designed for mass manufacturing. *Nearshore devices* are defined as devices that are in relatively shallow water. Devices in this location are often attached to the seabed, which gives a suitable stationary base against which an oscillating body can work. Like the shoreline devices, the shallow water leads to lower wave power. *Offshore devices* are generally in deep water. There is little agreement about what constitutes ‘deep’ water: ‘tens of meters’ is one definition, with ‘greater than 40m’ and ‘a depth exceeding one-third of the wavelength’ being others. The advantage of the offshore devices is that they can harvest greater amounts of energy because of the higher energy content in deep water waves. However, offshore devices are more difficult to construct and maintain, and because of the greater wave height and energy content in the waves, they need to be designed to survive the more extreme conditions adding cost to construction. Despite these drawbacks, floating devices in deep water offer greater structural economy [7].

Type: there are three predominant types of WECs: Attenuator, Point absorber and Terminator.

The *Attenuator* WECs lie parallel to the predominant wave direction and 'ride' the waves. An example of an attenuator WEC is the Pelamis, developed by Ocean Power Delivery Ltd (limited company or public limited company-Plc) [7].

Figure 2- Attenuator device: Pelamis wave farm [7]

The Pelamis device is a semisubmerged, articulated structure composed of cylindrical sections linked by hinged joints. The floating system is moored to the sea bottom through a complicated mooring system to hold the Pelamis in one place, but it would let the device self-align to the incoming waves. From the wave-induced motion of the hinged joints (shown in the next figure), the hydraulic PTO (power take-off) extracts the power and transfers electricity to the grid.

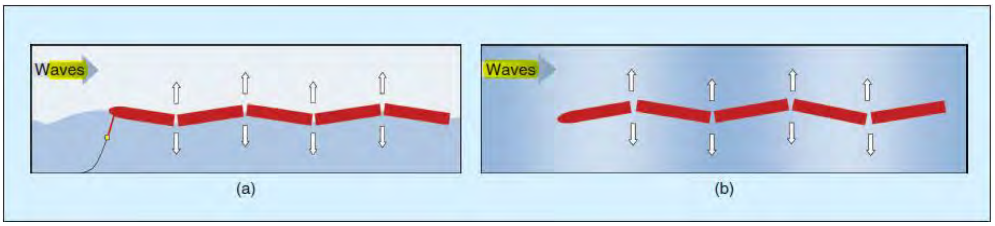

Figure 3- Illustrating the wave-induced motion of the Pelamis WEC [6]

The world's first commercial wave farm was created from three 750 kW (of power rated) Pelamis device in 2008, 5 km offshore from Povoa de Varzim in Portugal [6].

The *Point absorber* WEC is a device that has small dimensions relative to the incident wavelength. It can be a floating structure that heaves up and down on the surface of the water or submerged below the surface relying on pressure differential. Wave direction is not important for these devices (because of their small size and symmetry). An example of point absorber is Ocean Power Technology's Powerbuoy [7]. The next figure shows an artist's impression of wave farm using Powerbuoys.

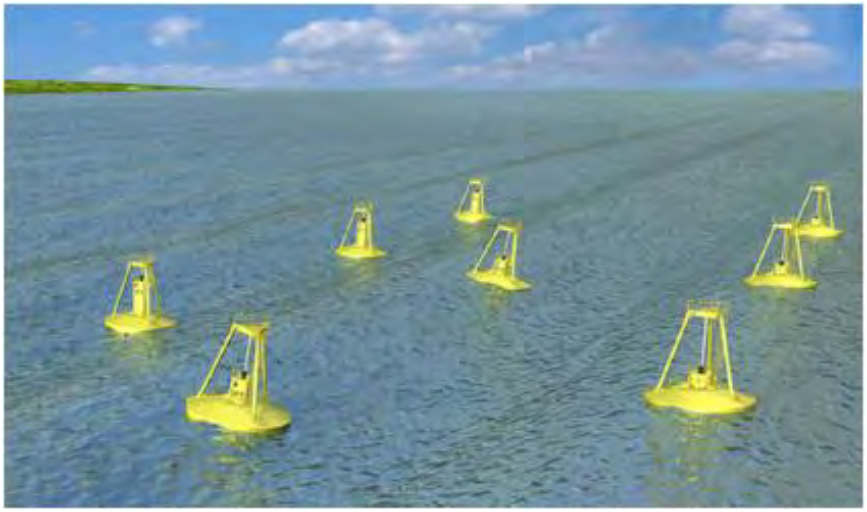

Figure 4- Point absorber device: OPT Powerbuoy [7]

The main projects are: 5 MW wave park deployed for the U.S. Navy in Oahu (Hawaii), 100 MW project in Coos Bay (Oregon) and from 2MW to 50MW wave park near Reedsport (Oregon) [1]. In 2005 in Atlantic City (New Jersey) the feasibility of wave power has been shown. The PowerBuoys installed in Hawaii and New Jersey have a rated power of 40kW each [1]. The wave power for use at US Navy bases (worldwide) has been demonstrated by the: testing, grid connection deployed for the U.S. Navy in Kaneohe Bay (Hawaii) and completed extensive environmental assessment.

The *Terminator* devices have their principal axis parallel to the wave front (perpendicular to the predominant wave direction) and physically intercept waves. One example of the terminator-type WEC is the Salter's Duck (developed at the University of Edinburgh) [7].

Figure 5- Terminator device: Salter's Duck [7]

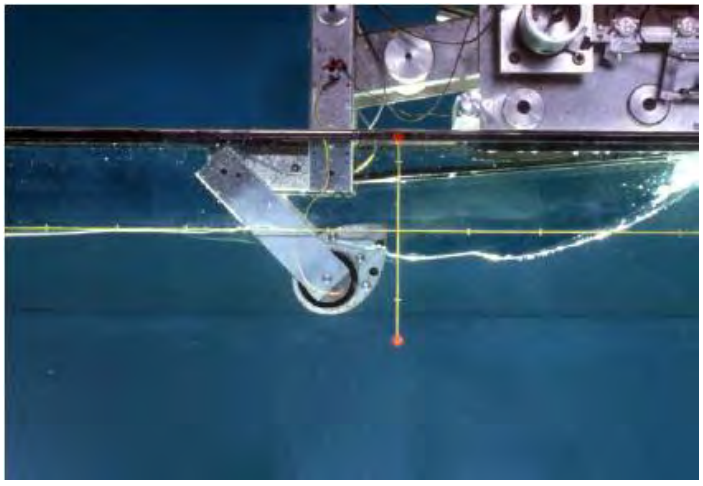

In that device the energy conversion is based on relative rotation (mostly pitch) rather than translation. The concept appeared in the 1974 and several versions were developed in the following years [9]. Basically it is a cam-like floater oscillating in pitch. The first versions consisted of a string of Ducks mounted on a long spine aligned with the wave crest direction, with a hydraulic-electric PTO system. Salter later proposed the solo duck, in which the frame of reference against which the nodding duck reacts is provided by a gyroscope. Although the Duck concept was object of extensive resource and development efforts for many years, including model testing at several scales, it never reached the stage of full-scale prototype in real seas [5].

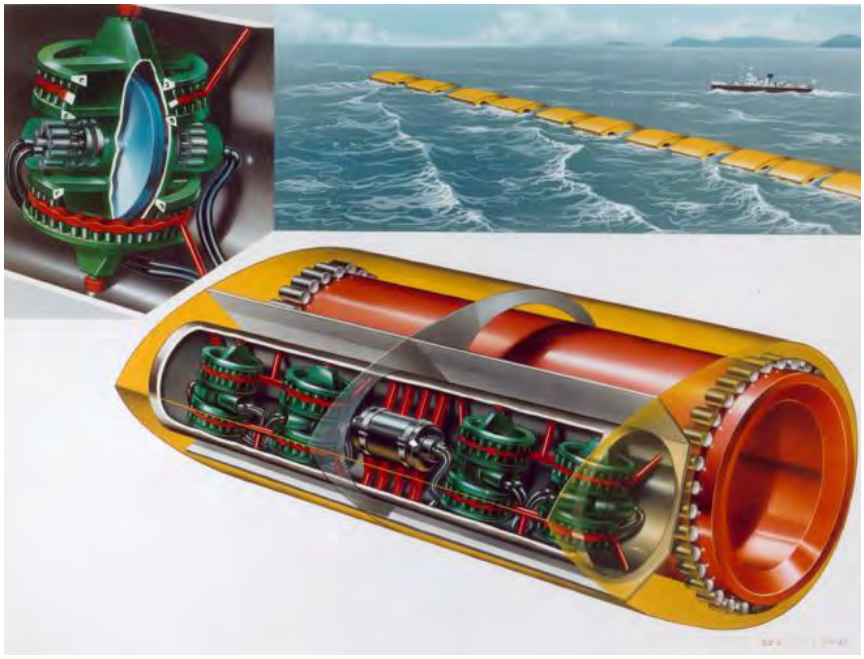

Figure 6- The Duck version of 1979 equipped with gyroscopes (courtesy of University of Edinburgh) [5]

Modes of operation: Within the categories identified above, there is a further level of classification of devices, determined by their mode of operation. Some significant examples are given below.

Submerged pressure differential device is a submerged point absorber. It uses the pressure difference above the device between wave crests and troughs. It comprises two main parts: a sea bed fixed air-filled cylindrical chamber with a moveable upper cylinder. When a crest passes over the device, the water pressure above the device compresses the air within the cylinder, moving the upper cylinder down. Instead when a trough passes over, the water pressure on the device reduces and the upper

cylinder rises. The submerged pressure differential device -is not exposed to the dangerous slamming forces experienced by floating devices and reduces the visual impact of the device (these are the main advantages). However, the maintenance of the device is a possible issue. Owing to part of the device being attached to the sea bed (for this reason these devices are typically located nearshore). The Archimedes Wave Swing (AWS), shown in the next figure, is an example of this device [7].

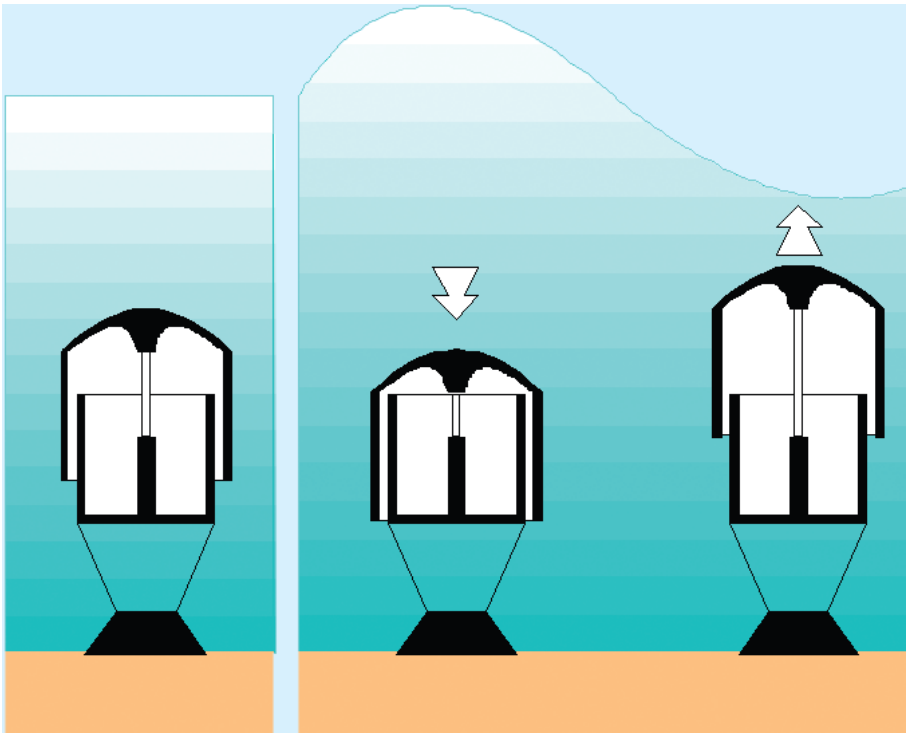

Figure 7- The operating principle of the Archimedes Wave Swing [6]

The AWS converter was developed by the Dutch company Teamwork Technology in 1993 [6]. The maximum energy can be extracted when the device is tuned in resonance with the waves. A direct-drive, permanent magnet linear synchronous (PMSL) generator -is used for energy conversion. The main reasons for choosing a PMSL generator are its high force density, -reasonable efficiency at low speeds and no contact with the translator. In the prototype, the maximum peak power was 2 MW while the maximum average power was 1 MW [6]. The prototype of the AWS was tested in 2004 on the northern coast of Portugal. However, during the end of testing, a severe failure occurred, and the device sank. Since then, the company moved to Scotland - and is currently developing the third generation of the AWS device-. This device is completely different from the prototype: the linear magnet generator was replaced by a hydraulic/pneumatic PTO, and the power rating of the device was increased considerably.

An *Oscillating wave surge converter* is generally comprised of a hinged deflector, positioned perpendicular to the wave direction (a terminator). It moves back and

forth exploiting the horizontal particle - velocity - of the wave. A noted example is the Aquamarine Power Oyster.

Figure 8- Oscillating wave surge converter: Aquamarine Power Oyster [7]

It is a nearshore device that is hinged - from the sea bed and has the top of the deflector above the water surface [7]. It uses the movement of a flap (12 meters by 18 meters) for wave power production. When waves come in and out to drive an oscillating wave surge converter, or pump, the pump delivers high-pressure water to drive a typical hydroelectric generator located on shore. The pilot testing started in 2008 off the Orkney - coast in Scotland. Each Oyster can produce from 300 kW to 600 kW peak power depending on location [1].

Figure 9- The Oscillator of the Aquamarine Power Oyster [1]

Oscillating water column (OWC): an OWC consists of a chamber with an opening to the sea below the waterline. As a wave approaches the device, water is forced into the chamber, applying pressure on the air within the chamber. This air escapes to atmosphere through a turbine. When the water retreats, air is then drawn back through the turbine. In this application a low-pressure Wells turbine- is often- used as

it rotates in the same direction irrespective of the flow direction (removing the need to rectify the airflow). It has been suggested -that one of the advantages of the OWC concept is its simplicity and robustness. There are examples of OWCs as point absorbers, as well as some being- built into the shoreline, where they act as a terminators [7]. The structure is made of concrete. The cross-sectional area of these OWCs (at mid water-free-surface level) lies in the range 80-250 m^2. Their installed power capacity is in the range 60-500kW. Smaller shoreline OWC prototypes (also equipped with Wells turbine) were built in Islay, UK (1991) [5]. An example of those shoreline mounted device is the Wavegen Limpet that is shown in figure 10. It is an OWC-type WEC developed by Wavegen Ltd in Ireland and the Queen's University of Belfast in the UK [3]. The device is installed on the Island of Islay, Western Scotland, and produces power for the national grid.

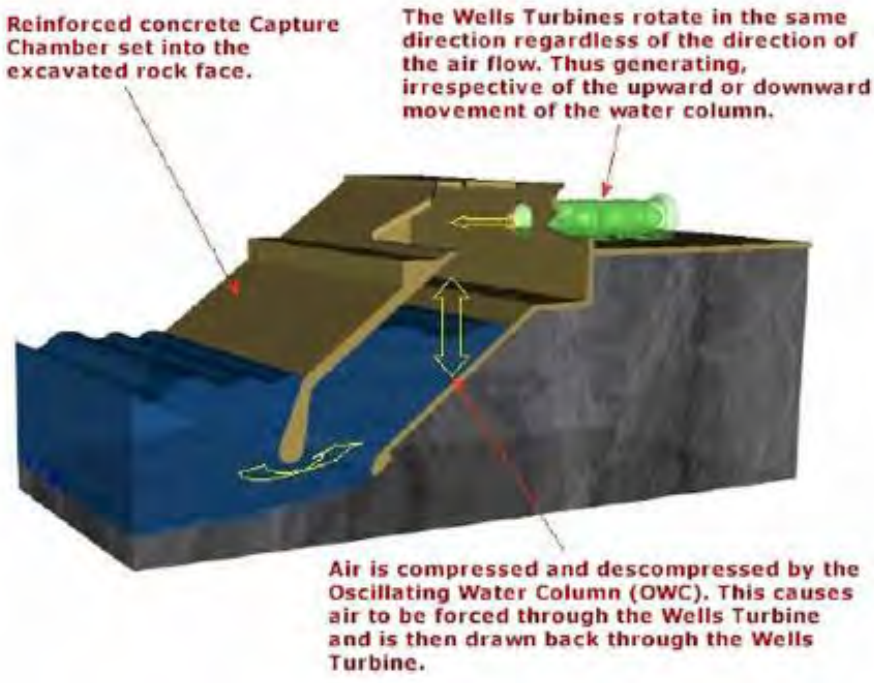

Figure 10 – OWC: the Limpet [7].

Overtopping device: an overtopping device captures sea water of incident waves in a reservoir above the sea level, then releases the water back to sea through turbines. An example of such a device is the Wave Dragon, which is shown in the figure 11. This device uses a pair of large curved reflectors to gather waves into the central receiving part, where they flow up a ramp and over the top into a raised reservoir, from which the water is allowed to return to the sea via a number of low-head turbines [7]. Wave Dragon is an offshore overtopping device which was invented by Friis-Madsen, Löwenmark F.R.I. Consulting Engineers, in 1999. This offshore terminator needs to be placed in water deeper than 20 m [6]. It has a one-step

conversion system, yielding to a very simple construction and has only the turbines and wave reflectors as moving parts.

(a)

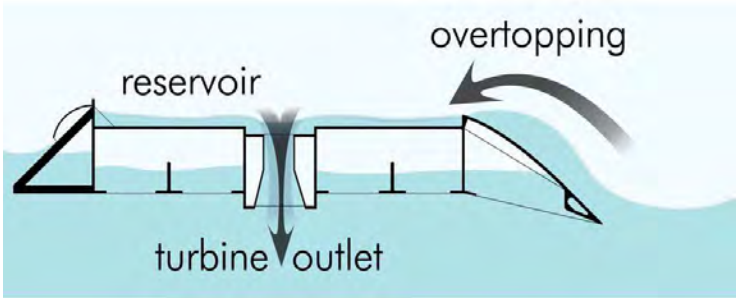

Figure 11- Overtopping WEC: the Wave Dragon [7]

The reservoir contains 1500 to 14000 cubic-meters of water. Device width is up to 390 meters [1]. Each unit can have a rated power of 4-7 MW depending on the wave climate at the deployment site [6]. The low-head turbines in the main structure extract the potential energy from water, which runs down from the reservoir to the sea. The efficient operation over the wide discharge range is ensured by using 16 relatively small turbines that can be switched on and off individually -rather than a few large turbines. The hydraulic efficiency of the turbine is 92% in the relevant head and flow ranges [6]. There are many challenges to be faced to design suitable low-head turbines: the turbines have to operate- at very low-head values ranging from 0.4 to 4.0 m (creating an exceptionally wide variation), they have to work from zero to full load frequently because of the wave distribution and the turbines have to operate in a very hostile environment (with only a minimum of maintenance being possible) [6]. To grant a high efficiency throughout the wide –head range, the turbines are operated at variable speed and directly- coupled to a generator. As mentioned in [6] three types of generator were compared for the Wave Dragon: a low-speed permanent magnet synchronous machine (PMSM) and a low-speed squirrel cage induction machine (SCIM) with or without a gearbox. The most

advantageous solution is a low-speed squirrel cage induction machine with a B2B (back-to-back, ac–dc–ac) converter, but also PMSM offers attractive solution for future devices.

1.2.2 Comparison and conclusions

The potential in wave energy is note-worthy. The previous survey introduces the current state of WEC technology and the major design problems and challenges that inventors and engineers face when building a WEC. It describes the major characteristics that can be used to categorize the devices.

	LIMP	PEL	WD	AWS
Operation principle	OWC	Attenuator	Overtopping terminator	Point absorber
Location	Onshore	Offshore floating	Offshore floating	Offshore submerged
PTO	Wells turbine	Hydraulic	Hydroturbine	PMSL
Power conversion system		6 AEM	16 B2B	B2B
Power quality	+	++	++	–
Cost of electricity (€/kWh)		0.07	0.11	0.03*
Development stage	++	++	+	0

*Price of the devices is not included.

Figure 12- Comparison of the Limpet (LIMP), Pelamis (PEL), Wave Dragon (WD) and Archimedes Wave Swing (AWS) [6]; asynchronous electric motor (AEM).

In the previous table several WECs are considered and evaluated based in important properties- such as type of PTO and prices of electricity (it is to be noted that we are considering prototypes, so the prices of the electricity are "optimistic"). Based on the comparison, the Pelamis WEC is the leading candidate of WECs, although -other technologies show promising features for the future. Despite significant research and development, the concepts for converting the motion of the waves into electricity still do not show any signs of converging to a single favoured solution. The present technology is not able to present a reliable, functioning device that would be commercially used. Moreover, it is not clear which prototype will prevail and how a WEC needs to be chosen for specific locations. A significant problem arises regarding optimizing- the WECs. All the subsystems need to be taken into account to reach an efficient operation and also the possible layout of the farm where the device will be deployed needs to be considered [6].

1.2.3 Initiatives and programmes in Europe

In several European countries research and development on wave energy is underway. The engagement in wave energy utilization depends strongly on the available wave energy resource. Countries with moderate, though exploitable resources, could utilize wave energy supplementary to other available renewable and/or conventional sources of energy (this is the case of Italy). In countries with high resources, wave power could cover a significant part of the energy demand in the country and even become a primary source of energy. In the following the main programs of the countries in Europe where wave energy has a high potential (the first part of the paragraph) and the initiatives carried out in Italy (in the last part of the paragraph) are described.

Denmark, Ireland, Norway, **Portugal, Sweden, Spain** and the **United Kingdom -** considered wave power as a feasible energy source a long time ago. These countries have been actively engaged in wave energy utilization under governmental support for many years and have significant wave power resources. This has led over the past 25 years to a large amount of RTD (research and technological development) work and considerable progress in wave power conversion [3].

Denmark lies in a sheltered area in the southern part of the North Sea. However -in the North-western regions of Denmark the wave energy resource is relatively favourable for potential developments. The annual wave power is between 7 and 24 kW/m coming from a westerly direction [3]. In paragraph 1.2 it is mentioned that a good location has a power potential only between 20 and 70 kW/m, but the annual wave power in Denmark is still a "good value" for a location in Europe. The annual wave energy resource of Denmark has been estimated to be about 30 TWh/yr, a-wave energy resource that has not been ignored by the Danish people [3]. In fact the "Danish Wave Energy Programme" started in 1996 with Energy 21, by assigning 5.3 MECU (Millions of European Currency Unit) for a period between 1998–2002 [3]. The objective was to promote wave energy technology following the successful Danish experience of wind energy. In 1997 a Danish Wave Energy Association was formed to disseminate information and arrange meetings [3]. Denmark's goal in the energy agreement (that was released by the Government in March 2012) to be 100 per cent renewable by 2050 is driven by concerns around security of supply, climate impact and green growth [12]. The energy agreement contains an allocation of € 3.3 million for wave energy installations and demonstration projects in the period 2014-2015 [12]. Energinet.dk, which manages the key funding programmes for wave energy research, has been the key driver of wave energy development in Denmark. It has fostered a collaborative approach to research efforts, which are funded by a mix of public and private investment. Despite coordinated activities, it is expected that wave energy technologies emanating from Denmark will not be ready for commercialisation until the early 2020s [12] .

Ireland is one of the countries in Europe that has significant wave power resources. According to Lewis [8], the wave energy resource of Ireland is 375 MWh/m at the 20 m contour location, while the total incident wave energy is around 187.5 TWh (a wave annual energy resource unique in the world). The policy of the Minister for Marine and Natural Resources is to encourage offshore electricity generation resources. In 1997 wave energy was supported under AER-3 (Alternative Energy Requirement) [3]. One project was selected for the offer of a Power Purchase Agreement and an EU grant-aid. However, the offer of the grant-aid was withdrawn by the EU on the basis that wave technology had not advanced sufficiently beyond the research stage to justify assistance under the European Infrastructure Operational Programme and the project did not proceed.

In the *2012-2020 Strategy for Renewable Energy* (published in May 2012) is contained the Government's strategy for reducing its reliance on foreign energy imports, addressing climate change and supporting the growth of renewable industries [12]. One of the five strategic goals is the fostering research and development in renewable such as wave and tidal. Since 2005 the Government has released policy and planning initiatives in support of its ocean energy industry. Several initiatives are: *Ocean Energy Strategy for Ireland* (2005), SEAI (Sustainable Energy Authority of Ireland) *Ocean Energy Roadmap* (2010) and *Harnessing Our Ocean Wealth: An Integrated Marine Plan for Ireland* (2012) [12]. An interdepartmental MCG (Marine Coordination Group) was established in April 2009 [12]. The goal of the group is to progress marine energy and other issues. The group meets monthly, bringing together representatives of departments with an involvement in marine issues to discuss issues that require interdepartmental action. In 2012, the MCG published "*Harnessing Our Ocean Wealth: An Integrated Marine Plan for Ireland*" which has three key goals: a thriving maritime economy, healthy ecosystems and engagement with the sea [12]. The plan also has two key targets: exceeding an annual turnover of € 6.4 billion from Ireland's maritime sectors by 2020, and doubling the marine sector's contribution to GDP to 2.4 percent per annum by 2030 [12]. Similarly, the SEAI *Ocean Energy Roadmap (2010)* identified potential cumulative economic benefits of a thriving ocean energy industry of the up to € 120 billion by 2050 and potential employment of up to 70000 jobs [12].

Norway has a long coastline facing the Eastern Atlantic with prevailing west winds and high wave energy resources of the order of 400 TWh/year [3]. Even though there is high wave energy availability, due to the economics and the uncertainties of the available technology, the conclusion of Energy and Electricity Balance towards 2020 are that 0.5 MWh will be the wave energy contribution to the Norwegian electricity supply, mainly from small-scale developments [3]. All of Norway's electricity supply has traditionally been renewable hydropower, but the increased electricity demand of recent years has not been met by an equal increase in power plants, due to public opposition to large hydropower developments.

The government is promoting land based wind and biomass plants, with particular focus on hydrogen as an energy carrier and gas fuel cell pilot projects. The environmental concern of high CO_2 emission from power generation for oil and gas offshore installations could create the basis for a potential wave energy market.

Norway started its involvement in wave energy in 1973 in the Norwegian University of Science and Technology (NTNU), and had official governmental support from 1978. In the 1980s two shoreline wave converters were developed, the Multi-Resonant Oscillating Water Column (OWC) and the Tapered Channel (Tapchan) of 500 and 350 kW respectively [3]. The OWC was built by Kvaener Brug A/S (a stock-based company) and the Tapchan by Norwave A/S in Toftestallen about 35 km north-west of Bergen (both were built in 1985). The plants were seriously damaged during storms in 1988 and 1991, but there are plans for re-opening the TAPCHAN plant [3].

The **United Kingdom** has considerable potential for generating electricity from wave power. It has prevailing wind direction from the west, and it is surrounded by stormy waters. The available wave energy resource is estimated to be 120 GW (annual average of power level) [3].

Like it has been said previously, wave energy RTD started in Scotland at the University of Edinburgh when the oil crisis in 1973 hit the whole world. In 1974 S. Salter published his initial research work on wave power [3]. The research on the offshore wave energy converter, the Salter Ducks, was started. In the meantime at least another ten wave energy projects were initiated in the UK. The government supported and funded extensively wave energy research until 1983 [3].

In 1999 the UK government declared a renewed favourable position in supporting R&D on wave energy with a budget of about £3 million over the following three years until the 2003 [3]. Furthermore, the success of the initial LIMPET OWC project and its full decommissioning in 1999, has created the basis for including three wave energy projects (of a total of 2 MW capacity) in the third Scottish Renewable Obligation (SRO-3): the Limpet, the Pelamis and the Floating Wave Power Vessel [3].

'The Energy from the Sea' by the Marine Foresight Panel outlines the 'roadmap' (1999) for the development of wave energy in Scotland towards 2020 [3]. A Commission for Wave Power in Scotland was launched in 1999, which involved representatives from the government, the industry and the utility company [3]. The Commission will work in order to create the basis for development of wave energy.

Two organisations involved with wave energy are going to be formed in the near future. The first one is the 'Marine Energy Technology Network' (METN). It will be a virtual network incorporating Universities and companies, consultants etc. The other is the 'Sea Power Association' which will work closely with METN and also with the British Wind Energy Association (BWEA) [3].

UK governments have been active in developing policy and putting in place incentives to foster market conditions conducive to supporting the growth of ocean

energy. The initiatives that have been made by the Government are: the establishment of the Energy Technologies Institute (ETI, 2007), the *Low Carbon Industrial Strategy* (2009), the *Marine Energy Action Plan* (MEAP, 2010), the establishment of the Marine Energy Programme Board (MEPB, 2011), *UK Renewable Energy Roadmap* (RER, 2011) and *Future of Marine Renewables in the UK* (2012) [12]. All the previous initiatives and established institutions are useful for the development of wave energy in the future. They help the resolution of the problems that has wave energy in our days- (the lack of fund in research and development, the problems of the "electric market of wave energy" and so on).

Spain's northern coastline and Canary Islands are endowed with strong wave resources that in recent years have motivated a number of milestone projects. In November 2011 there was the deployment of the first grid-connected wave power plant (an oscillating water column wave energy converter) in Spain in the port of Mutriku [12]. That project set a benchmark for the on-going development of wave energy in Spain. Also, the construction of the BIMEP (Biscay Marine Energy Platform) test facility is expected to provide national and international wave energy stakeholders the opportunity to "learn through doing" [12]. It is intended to encourage the development of complementary industries to assist the growth of Spain's wave energy sector.

The "*2011-2020 plan"* was approved in November 2011 by the outgoing Zapatero Government. The plan includes Spain's first ever wave installation targets, with 10 MW expected by 2016. Based on an annual growth rate of 20-25 MW from 2016 to 2020, a target of 100MW has been set for 2020 [12].

Due to political reasons, mainly the focus on other energy sources, or lack of exploitable resources, wave energy conversion has not undergone significant development in **Belgium, Finland, France, Germany, Greece, Italy** and **Netherlands** in the past years.

Italy has a long coastline in relation to its land area. Especially for this reason it would appear suitable for utilisation of ocean energy. However, wave studies around the coastline show that, in general, the annual average of power level is less than 5 kW/m [3]. There are a number of offshore islands and specific locations (mainly in the south of Italy, such as Sicily or Sardinia) where the mean wave energy is higher, up to approximately 10 kW/m [3].

R&D on ocean energy exploitation is conducted mainly in the 'La Sapienza' University of Rome, by Ponte di Archimede nello Stretto di Messina S.p.A. (Società per Azioni) and by Enel Green Power (using a wave energy converter developed by 40South Energy).

In the University of Rome a novel wave energy device is developed, which is particularly suitable for closed seas of moderate wave power. The system utilizes a floating gyroscopic converter, that is excited to oscillations by the waves and provides mechanical power to an electrical machine. Ponte di Archimede nello Stretto di Messina S.p.A. is developing the ENERMAR plant, utilizing marine

currents. It consists of a floating Kobold turbine, which drives an alternator. A 130 kW prototype with a 6 m diameter turbine is currently being constructed. It will be deployed 1.50 m offshore Messina [3].

As mentioned in [13] the initial testing phase for the R115 wave energy converter (nominal capacity of 150 kW) at Punta Righini in Tuscany is successfully completed. There is a partnership between the companies Enel Green Power and 40th South Energy. The goal of their technological partnership is to increase the number and capacity of the converters that will be launched from the Port of Livorno towards Punta Righini (Castiglioncello). The new converter was designed and built for Enel Green Power (EGP) by 40South Energy, one of the most innovative companies at the international level in the marine energy sector. Once fully operating, each of the R115 family converters will be able to generate around 220 MWh/yr (enough power to meet the needs of more than 80 households) [13]. The two companies are continuing to work on optimising the materials and structure of the machine with the goal of soon installing other machines of the same class in the Mediterranean Sea and in an ocean environment. EGP and 40South Energy have further strengthened their technological partnership in order to develop a new wave energy converter with a nominal capacity of 2 MW, building upon the operational systems employed and maintaining the essential features of the model R115 [13].

2. MODEL DESCRIPTION

The model is the same that Alessandro Bozzetto used in the simulations of his master's thesis [11] and very similar to the model described in [14]. It is composed of a cylindrical point absorber in heave with a hemispherical bottom (buoy), which is directly coupled to a rotating electrical machine via a gearbox. The radius and the draught of the point absorber are both equal to 5 m. Its mass is M=670140 kg. The gear ratio is equal to 20 and the pinion radius is 0.1 m [14]. The considered system is schematically represented in the next figure.

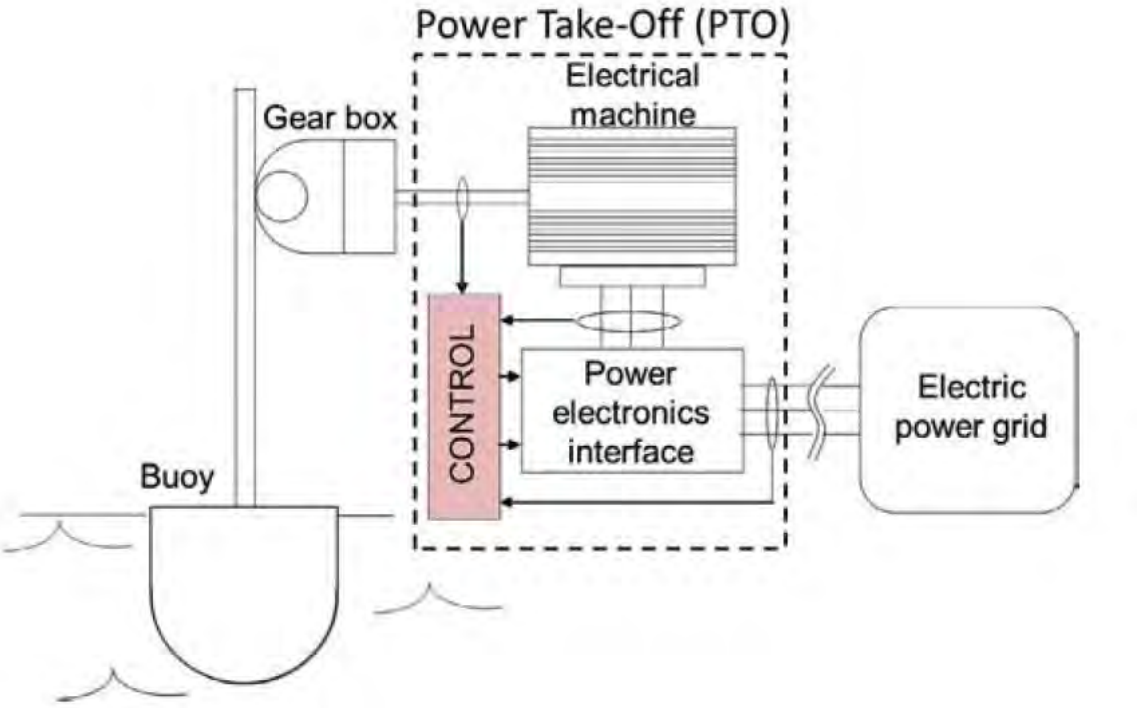

Figure 13- Simplified model of the wave energy converter [14].

The electrical machine (PMSM) and the power electronics converters, which are required both to control the electrical machine and to potentially allow the grid interconnection of the whole system, compose the PTO. In the first part of the thesis the model the power electronics converters and also the electrical machine are not included (thus neglecting corresponding losses). The goal of the simulations of the first part of the thesis is to find several magnitudes (as for instance the average mechanical power, the maximum power and the maximum torque) in function of the the $\boldsymbol{B_L}$ coefficient with the goal to analyse the performances of the passive loading control with several constraints.

2.1 The hydrodynamic model

The aim is to properly represent the interaction between the sea waves and the point absorber, which is a single degree of freedom device. The Cummins equation can be used [15]:

$$\boldsymbol{F_E(t) + F_L(t) = (M + a_\infty)\ddot{s}(t) + \int_\infty^t K_{rad}(t-\tau)\dot{s}(\tau)d\tau + Ks(t)} \quad \textbf{(2)}$$

Where **s** is the position of the buoy and $\boldsymbol{\dot{s}}$ is its speed, $\boldsymbol{F_E}$ is the excitation force applied by the waves to the point absorber and $\boldsymbol{F_L}$ is the force applied by the PTO. The radiation force that represents the effect of radiated waves produced by the oscillation needs also to be taken into account. In (2) it is expressed by the convolution integral, $\boldsymbol{K_{rad}}$ being the radiation impulse response function. Moreover, **M** is the mass of the device including the contribution due to the PTO inertia, **K** is the hydrostatic stiffness and $\boldsymbol{a_\infty}$ represents the value of added mass at infinite frequency [14].

2.2 Control of the point absorber

The goal is obtain energy from sea waves and this can be realized creating a destructive interference among the waves generated by the vertical motion of the point absorber and the incident waves. The waves generated by the vertical motion of the buoy depend on the force applied on it by the electrical machine which can be controlled. Therefore the device can be tuned in accordance with the sea state with the aim to obtain the maximum power extraction. The complex-conjugate (reactive) and the passive loading control are the most well-known control strategies for the point absorbers, indeed they have been thoroughly studied especially with ideal sinusoidal incident waves (regular waves) [40] [41]. The passive loading control involves the use of equation (3). Which means that the force applied by the PTO is equal to the actual velocity of the buoy multiplied a constant $\boldsymbol{B_L}$ coefficient [14]:

$$\boldsymbol{F_L(t) = B_L\dot{s}(t)} \quad \textbf{(3)}$$

Using the passive loading control the instantaneous power extracted by the buoy is always positive. In the case of complex-conjugate control the equation (3) is not anymore valid and the equation (4) is true. As it can be seen, beyond the component which is proportional to the actual velocity of the point absorber, the force exerted by the PTO has a component that is equal to the buoy acceleration multiplied the $\boldsymbol{M_L}$ coefficient [14]:

$$\boldsymbol{F_L(t) = B_L\,\dot{s}(t) + M_L\,\ddot{s}(t)} \quad \textbf{(4)}$$

With the complex-conjugate control the instantaneous power extracted by the buoy is not always positive. Because, with the goal to maximize the overall power extraction, some energy must be given to the sea during some ranges of time. As consequence the electrical machine works as generator in some intervals and as motor in others. This can be made with the utilization of a 4-quadrant power electronics converter. In [11] a different control strategy has been applied, which implies the $\boldsymbol{F_L}$ force to be constant and to have sign concordant with the speed of the buoy. Also with this control strategy the instantaneous power extracted by the buoy is always positive.

Beyond the control strategies there can be different types of modes of operation of the point absorber: the "unidirectional case" and the "bidirectional case". In the first case it is assumed that the buoy is a single-capture device, i.e. which it only extracts power during the upward motion of the floater (i.e. when the waves lift the buoy up) while during the downward movement no torque is applied by the PTO. Instead, when the "bidirectional case" is applied, the double-capture point absorber is considered. It extracts power during both the upward and the downward movement of the buoy [16]. In this thesis only the passive loading control, in mode of operation "bidirectional case", has been used in the simulations and in the next chapters the results of the simulations are shown and explained.

2.3 Wave profile generator

For having more realistic results it is necessary a wave profile of 900 s, which is considered representative of a sea state. The energy of a sea state is often represented as a function of the frequency of the incident waves by an energy spectrum, which can be analytically modelled starting from one or more parameters. In the following it is assumed that the sea state can be represented by a Bretschneider spectrum [15].

$$\boldsymbol{S_\zeta^B(\omega) = \frac{A}{\omega^5} e^{-\frac{B}{\omega^4}}} \quad \textbf{(5)}$$

In the previous equation it is expressed the Bretschneider spectrum. **A** and **B** are definitions parameters, functions of the wave system features and $\boldsymbol{\omega}$ is the angular frequency. As explained in [17], the excitation forces exerted by the waves on the WEC can be calculated from the energy spectrum and by knowing the physical and geometric properties of the considered point absorber. In the next figure is plotted an example of wave profile over time, ***Te*** is the energy period and ***Hs*** is the wave height as defined in [23].

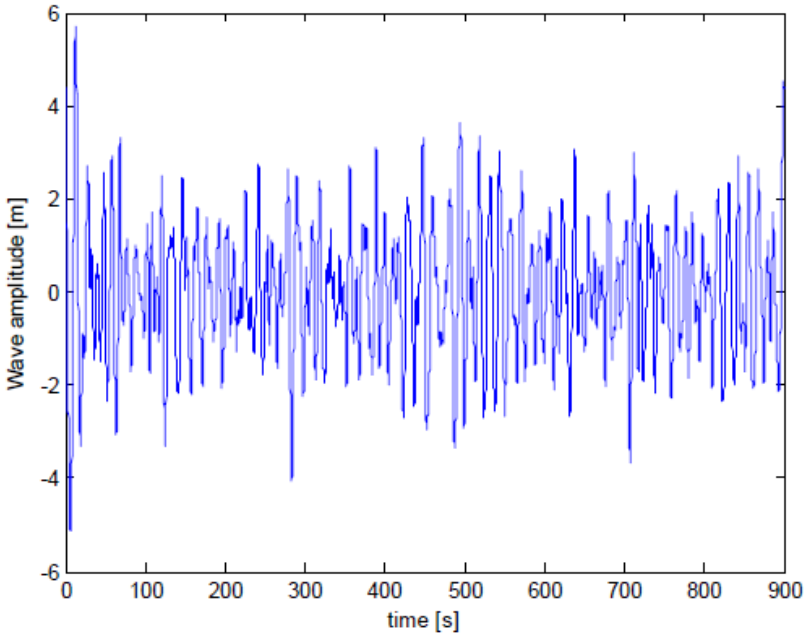

Figure 14- Example of an incident wave profile, *Hs*=5.75 m, *Te*=12.5 s [11].

2.4 Simulink model and introduction of the power limit

In [11] a program in Matlab is written and a Simulink model is implemented which is composed by a hydrodynamic model, a block for the passive loading control and the bidirectional/unidirectional case and visualization part with a lot of scope blocks. Therefore in [11] the modes of operation of the point absorber that have been used are the "bidirectional case" and the "unidirectional case". As control strategy the passive loading control has been used. In the following figure it is shown the hydrodynamic model adopted.

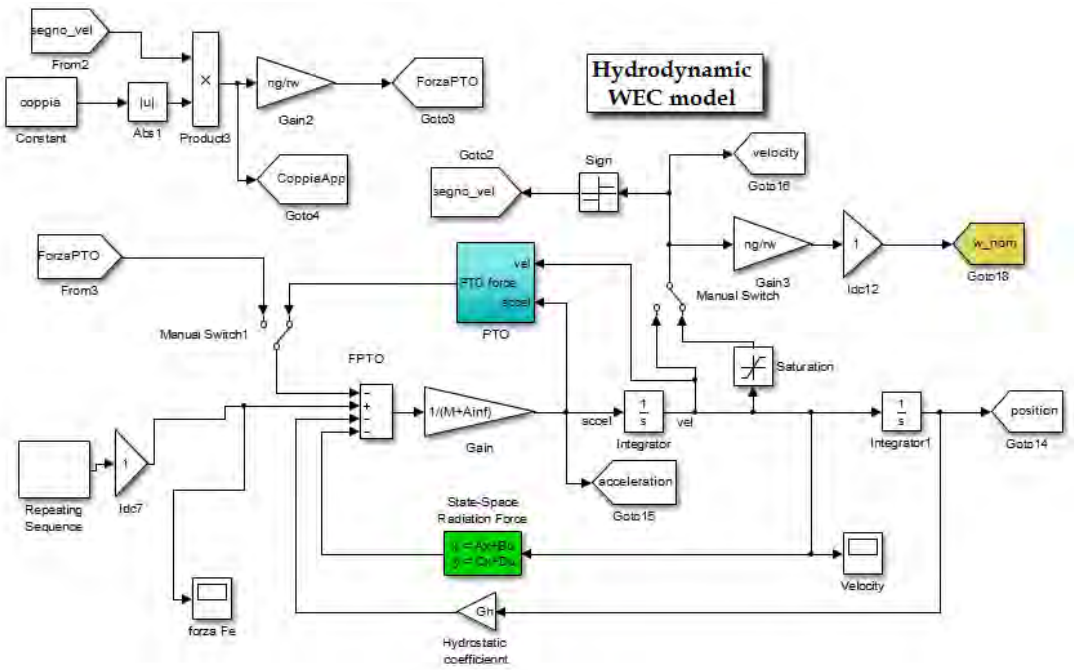

Figure 15 - Hydrodynamic model in Simulink of the different types of the control of the point absorber (unidirectional, bidirectional and passive loading) [11]

With an appropriate setting of the switches the different cases can be implemented (if the switches are set like in the figure 15 and $\boldsymbol{M_L}$ is equal to 0, the passive loading is applied): this model is very flexible and the mechanical power is calculated as product of PTO force and velocity of the buoy. This hydrodynamic model implements the equation (2), and the most important components of the model are the block of the State-Space Radiation Force and the PTO block for the (control) , which is shown in the figure 16. It represents respectively the equations (3) and (4), for this reason it is so important. Setting $\boldsymbol{B_L}$ and $\boldsymbol{M_L}$ it is possible to change the control strategy of the point absorber, passive loading and complex-conjugate respectively. As explained previously in the paragraph 2.2 in this thesis $\boldsymbol{M_L}$ is always equal to zero because only the passive loading control is used.

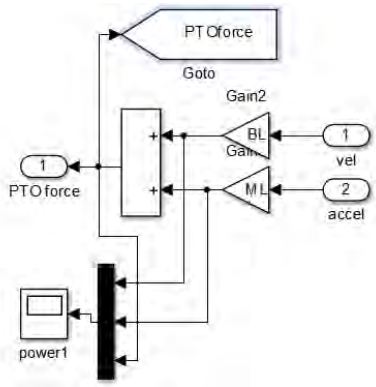

Figure 16- PTO block for the WEC control

The first goal of this thesis is to apply the power limit to the passive loading control. The power limit is introduced to obtain a more realistic model, because it is useful to

understand better the behaviour of the power trend under realistic condition of constrained PTO. Then it is possible to obtain money savings and lower losses of power inside the electrical machine because the performance is better, consequently the power converted from mechanical to electrical can be higher with a small size machine rather than with a larger machine operating at low load [22]. In figure 17 it is shown the power limit applied to the passive loading control.

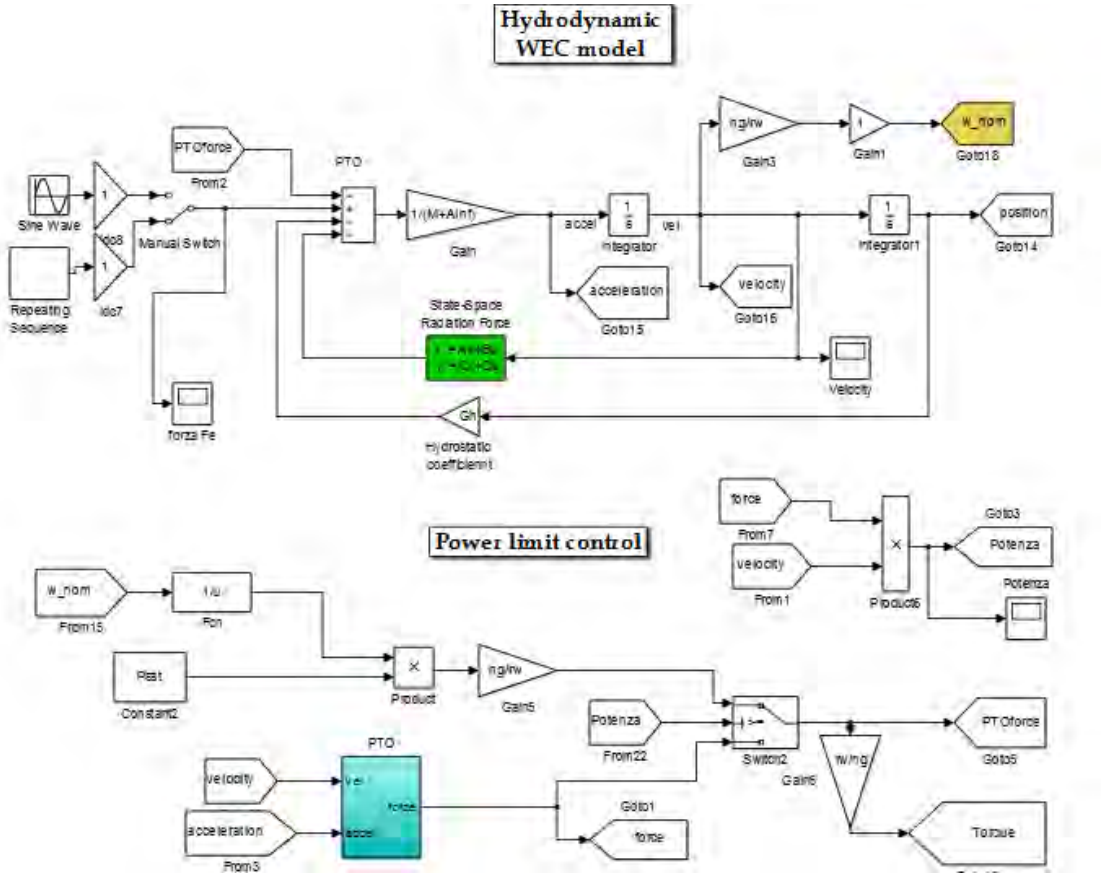

Figure 17- Hydrodynamic model in Simulink of the passive loading control constrained

If the power limit set isn't exceeded (mechanical power lower or equal to the power limit), the Simulink model works as the passive loading unconstrained control. Instead whether the mechanical power is becoming higher than the value of the power limit, the power limit is activated and the force applied to the PTO is not anymore calculated using (3). It is obtained from the power limit control as it is shown in figure 17 and as it is explained by the equation (6) (***Psat*** = ***Plim*** = power limit).

$$\boldsymbol{F_L(t) = \frac{Plim}{\dot{s}(t)}} \qquad \textbf{(6)}$$

3. RESULTS OF THE PASSIVE LOADING CONTROL

3.1 Energy sea state and scatter diagram

Before to show and analyze the results obtained using the passive loading control strategy it is mandatory explain what a scatter diagram is and its correlation with the sea states. The scatter diagram is a matrix that has on the x-axis the wave energy period (***Te)*** and on the y-axis the significant wave height (***Hs***). Sometimes there is the zero crossing period (***Tz***) on the x-axis which is correlated to ***Te*** through the following equation [23]:

$$Te = 1.2\,Tz \tag{7}$$

Each marine location has a different scatter diagram which usually is referred to one year. Inside the diagram usually can be found the wave data occurrences, the extracted power or the yearly energy.

Hs \ Te	2,5	3,5	4,5	5,5	6,5	7,5	8,5	9,5	10,5	11,5	12,5	13,5	14,5	15,5	Sum	Acc	Te ave	dP
0,25															0	0		0,00
0,75				1	5	6	1								13	13	7,04	0,03
1,25				8	28	44	23	7							110	123	7,44	0,63
1,75				8	38	48	45	24	5						168	291	7,82	1,98
2,25				1	28	37	30	33	14	3					146	437	8,32	3,03
2,75					7	34	30	25	18	6	1				121	558	8,79	3,96
3,25					1	16	28	20	18	9	1				93	651	9,24	4,47
3,75					0	4	21	17	15	12	5	1			75	726	9,89	5,14
4,25						1	14	19	14	10	5	2			65	791	10,13	5,86
4,75						0	4	15	14	10	5	3			51	842	10,62	6,02
5,25						0	1	9	13	9	4	2	1		39	881	10,91	5,78
5,75							0	3	11	9	5	2	1		31	912	11,34	5,72
6,25								2	7	6	5	2	1		23	935	11,54	5,11
6,75									4	5	4	2	1		16	951	11,94	4,29
7,25									2	4	3	2	1		12	963	12,17	3,78
7,75								0	1	3	4	2	1		11	974	12,41	4,04
8,25										2	2	2	1		7	981	12,79	3,00
8,75									0	1	2	2	1		6	987	13,00	2,94
9,25									0	0	1	1			2	989	13,00	1,10
9,75											1	1	1		3	992	13,50	1,90
10,25										0		2	1		3	995	13,83	2,15
10,75													1		1	996	14,50	0,83
12,75																		
Sum	0	0	0	18	107	190	197	174	136	89	48	26	11	0	996			71,74

Figure 18 – Joint probability diagram (*Hs* and *Te*) for Belmullet location (54° N; 12° W); probability of occurrence in parts per thousands , all directions, all year [24].

Figure 18 is an example of scatter diagram of a location in Ireland and the probability of occurrence in each box (for particular values of ***Hs*** and ***Te***) is given in parts per thousands without decimal points. In fact, as it can be seen, the sum of occurrence is

not 1000 (but 996). The data are results from the ECMWF (European Centre for Medium-Range Weather Forecasts) wind-wave WAM (Wave Atmospheric Model), covering an 8-year period (1987-1994). In each cell the frequency of occurrence can also be given in hours per year or in percent. As it can be seen each cell represents an interval which is long 1 second for the energy period ***Te*** and is 0,5 metre for the significant wave height ***Hs***. In column "Sum" the total probability of each ***Hs*** is shown and in column "Acc" the accumulated probability is represented. Close to it there is the column "Te ave" which shows the average period $T_{e\,ave}$ for each ***Hs*** row ($T_{e\,ave}$ is the most likely energy period associated for a ***Hs*** value). Finally there is the column "dP" within which can be found the values of the power contribution of each row. The annual average power level kW/m of the site is represented by the last cell of the column "dP" and is obtained by summing the power contribution of each row. Each combination of ***Te*** and ***Hs*** corresponds to a different sea state, they are 115 in the scatter diagram of figure 18. So if for example it is wanted an evaluation of the energy in MWh which can be extracted in one year in the specific location of the scatter diagram all the sea states represented in the scatter diagram should be taken into account and 115 sea states should be simulated. But this is not a goal of the thesis. The aim of this thesis is more addressed to the control of the electrical machine and to the connection to the electric grid of the PTO, it isn't a study of the extracted energy from a specific location. For this reason only three representative energy sea states will be considered in this thesis. They are the same that have been used in [11] and they are shown in table 2. Increasing the significant weight height and the wave energy period the energy of the sea state increases, because, as it is defined in [24], the global power level (from all direction, in deep water) of a sea state is given by:

$$P_w(H_s, T_e) = \frac{\rho g^2}{64\pi} H_s^2 T_e \sim 0,49\, H_s^2\, T_e \qquad [kW/m] \tag{8}$$

ρ is the density of the ocean water in Mg/m^3 and g is the gravity constant. Each combination of ***Te*** and ***Hs*** corresponds to a different sea state with a own Bretschneider spectrum $S_\zeta^B(\omega)$ (equation (5)). The wave energy spectrum, according to [17], allows to obtain the excitation force $F_E(t)$ in the time domain during the simulation and resolve the Cummins equation (equation (2)).

Hs **significant weight height**	***Te*** **wave energy period**	**Energy sea state**
1.414 m	7.713 s	low
3.75 m	9.5 s	medium
5.75 m	12.5 s	high

Table 2- Three representative energy sea states used in the thesis

Also the incident wave profile over the time is obtained from the Bretschneider spectrum. It is different for each energy sea state and in the following figures the

wave elevation profile is represented for every case. As it has been mentioned in paragraph 2.3 the simulation time is 900 seconds for having more realistic results of the considered sea state.

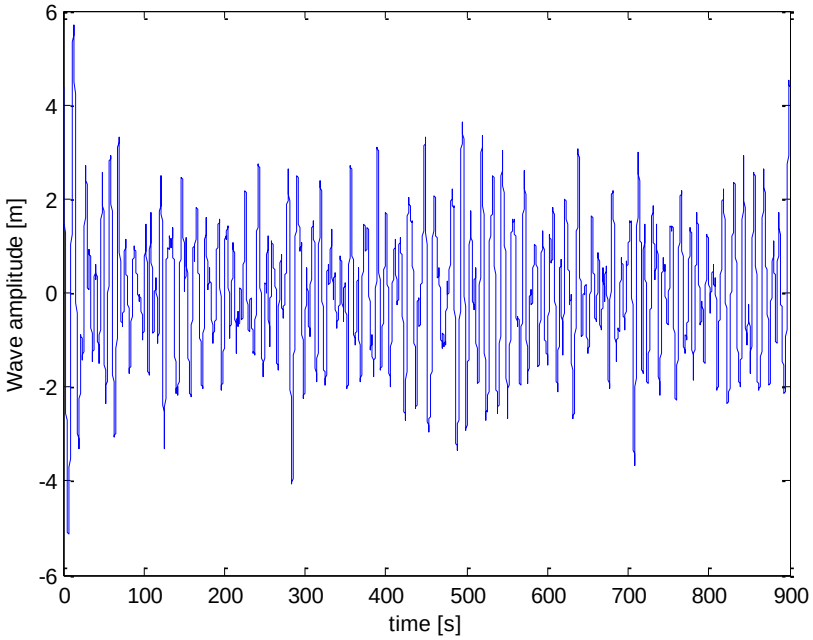

Figure 19 – *Hs* = 5.75 m, *Te* = 12.5 s, incident wave profile of the high energy sea state [11]

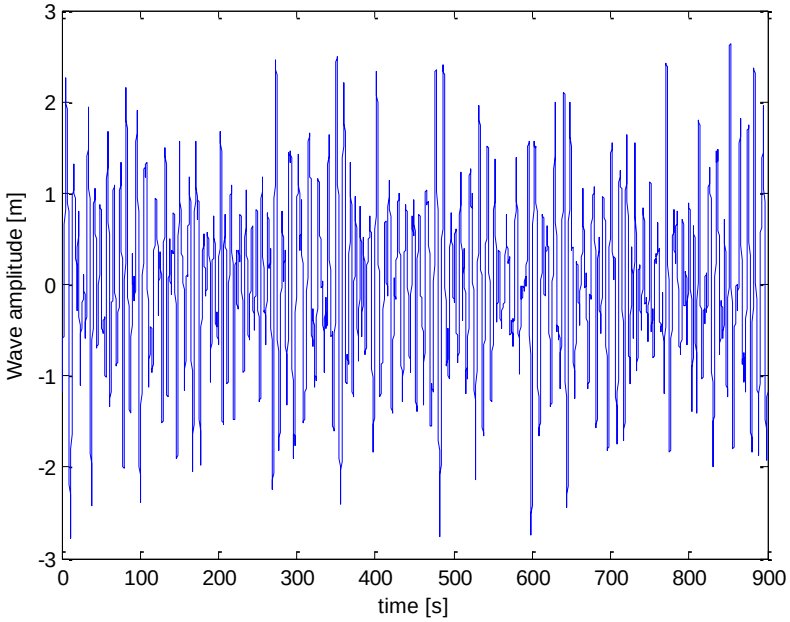

Figure 20 - *Hs* = 3.75 m, *Te* = 9.5 s, incident wave profile of the medium energy sea state [11]

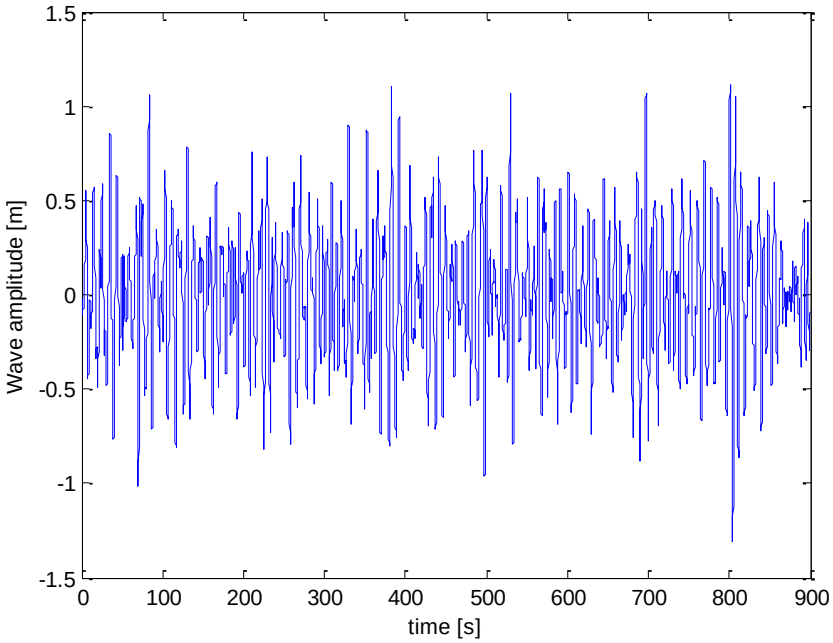

Figure 21 - *Hs* = 1.414 m, *Te* = 7.713 s, incident wave profile of the low energy sea state [11]

For all the simulations these sea states are used every time, since it is important to use the same incident wave profiles for the repeatability of the results. In general, for the same ***Hs*** and ***Te*** used, the Bretschneider spectrum generator would give different incident waves. In fact some parameters, like the phase used in the program, are generated randomly every time the wave generation is run [17].

3.2 Results with no constraints

In this paragraph all the simulations are made without constraints, therefore there aren't limits of power, torque, PTO force, buoy velocity and position. It is an ideal situation and it is useful to understand the basic operations of the system. In this paragraph and in all the simulations described in this chapter the electrical machine there isn't in the Simulink model. It is like to have in the system an ideal generator without losses (with the electrical power equal to the mechanical power) which has the electrical torque perfectly equal to the mechanical torque of the point absorber in each instant of the simulation. The goal is to find the $\boldsymbol{B_L}$ coefficient for each energy sea state, that gives the maximum average mechanical power, and other parameters like the maximum power and the maximum torque useful for the sizing of the electrical machine. The results of the passive loading without constraints (obtained in [11]) have been calculated and confirmed in this paragraph. They are shown and described in order to make easier the comparison with the results with constraints that will be described in the following paragraphs. As it has been said previously in this thesis only the passive loading control is used in the simulations.

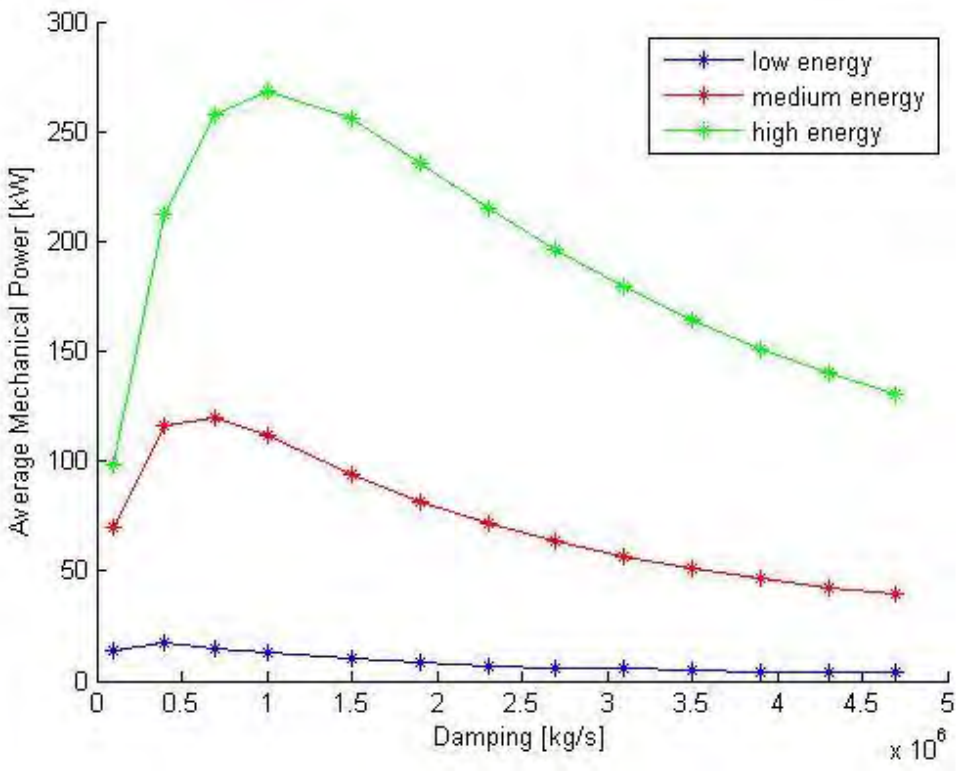

Figure 22- Diagram Mechanical Power-Damping

In the previous figure the average mechanical power for different values of the damping coefficient ($\boldsymbol{B_L}$) is shown. For each energy sea state there is a peak of the average power corresponding to a value of the damping coefficient applied. For values of the damping coefficient lower or higher than this the mechanical power decreases. In the low energy sea state the peak of average mechanical power is achieved with a $\boldsymbol{B_L}$ equal to 400000 kg/s, in the medium with $\boldsymbol{B_L}$ equal to 700000 kg/s and in the high energy sea state with $\boldsymbol{B_L}$ equal to 1000000 kg/s.

Thus an increment of the energy content in the sea state implies an increase of the $\boldsymbol{B_L}$ that must be applied to extract the maximum average mechanical power.

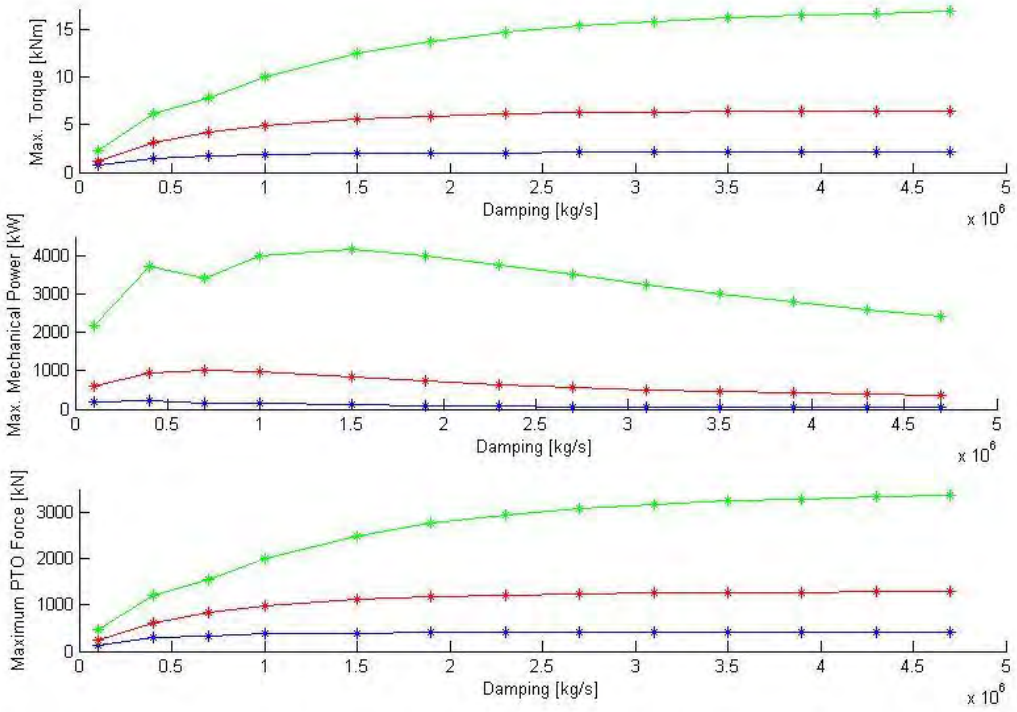

Figure 23 - Diagram Maximum values of Torque, Mechanical Power, PTO force

Figure 23 shows the behaviour of the maximum torque in module, maximum mechanical power and maximum PTO force in module reached during the 900 seconds of simulation. The trend of the torque is equal to the PTO force, because the PTO force multiplied for the pinion radius (rw=0.1 m) and divided the gear ratio (ng=20) is equal to the torque. Increasing the $\boldsymbol{B_L}$ coefficient, the PTO force increases and achieves an asymptote (different for each energy sea state). The diagram of the maximum mechanical power is different, in fact for each energy sea state a peak of mechanical power is achieved and for different values of the $\boldsymbol{B_L}$ coefficient the maximum mechanical power is lower. The decrease of the average mechanical power and of the maximum mechanical power for high values of the $\boldsymbol{B_L}$ coefficient is justified by the fact that when $\boldsymbol{B_L}$ is very high the buoy is damped too much and as consequence the actual speed and movement of the buoy is reduced. This involves a reduction of the power because the mechanical power is directly proportional to the square of the velocity of the buoy as it is justified by equation 8. The legend in the previous figure is the same of the figure 22: the green line represents the high energy sea state, the red one the medium energy sea state and the blue one the low energy sea state. The diagrams in figure 23 are useful to understand better the sizing of the electrical machine and thanks them a preliminary selection of the electrical machine can be made. Indeed whether the machine is sized for values of torque and power lower than the maximum values shown in the diagrams, there is a possibility that it will work in overload with serious consequences in life time and performance. Thus

the machine must be dimensioned for the maximum values of torque and power or made able to withstand predefined overloads.

When the B_L coefficient is greater than 500000 kg/s in the high energy sea state very high values of torque (15 kNm) and PTO force (3000kNm) are reached. An electrical machine that is dimensioned with a nominal torque of 15 kNm is useless and very expensive, on the contrary it can be useful to downsize the electrical machine so that has a torque close to 1 kNm if the rated power is around to 100kW. It happens the same in the low and medium energy sea state, but the difference between the maximum value of the torque and 1 kNm is smaller. From these considerations it appears obvious that a torque limit or a power limit is needed, which allows to reduce the maximum torque, therefore the electrical machine can be dimensioned for a lower rated torque with a saving of money as consequence. In figure 24 the maximum values of buoy position and velocity are shown.

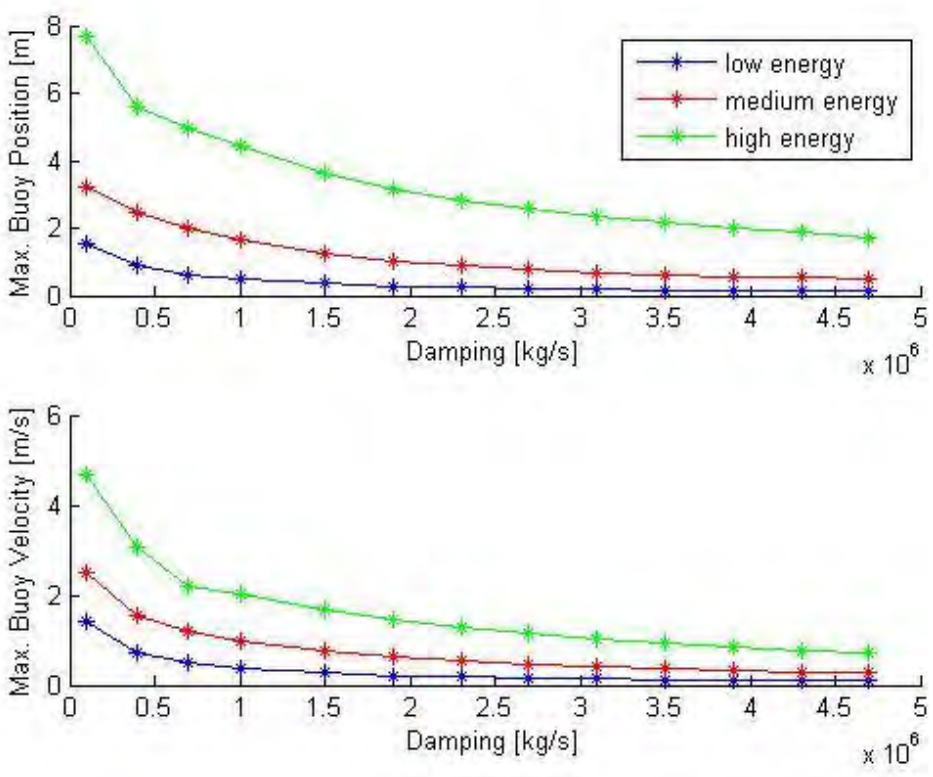

Figure 24 - Diagram Maximum Values of Buoy Position and Velocity

As expected if the damping coefficient increases the position and the velocity of the buoy decrease, this effect is due to high values of PTO force applied that force the buoy to have a lower oscillation.

Table 3 – Main results of the simulations with no constraints

	Max average power [kW]	Damping [kg/s]	Max PTO Force [kN]	Max Torque [kNm]	Max Power [kW]	Max Buoy Position [m]	Max buoy velocity [m/s]	Peak to average power ratio
low energy sea state	17	400000	294.3	1.47	216.6	0.88	0.74	12.74
medium energy sea state	120	700000	838.4	4.2	1004	2	1.2	8.37
high energy sea state	270	1000000	2000	10	4005.2	4.41	2	14.83

In the table 3 the main results are summarized. For each energy sea state the $\boldsymbol{B_L}$ coefficient with which the maximum average mechanical power is obtained is taken into consideration: in fact it is in that point where it is theoretically more convenient to operate the system, but it is necessary to add the electrical machine in the model with the goal of veryfying the corresponding production of the electrical energy, which should also be maximized. Also the peak to average power ratio is shown in the table for each energy sea state. It is better that is as low as possible with the aim to exploit better the investment of the electronic devices and the electrical machine [42]. As a matter of fact the electronic devices and the electrical machine are dimensioned for the peak value of power, this must be considered because if the power electronics equipment and the electrical machine are sized for a great value of power, when the average power is much less than this, the system mostly operates in low conditions, with low efficiency and consequent waste of money. Without limitations in the model the maximum torques and the peak to average power ratios in the previous table for all the energy sea states are inappropriate and too high. For this reason in the next paragraphs several power limits (75kW, 100 kW and 200kW) will be tested, that correspond to the maximum power which can produce an electrical machine without consequences in life time and performance, with the goal to reduce the values of the maximum torque and the peak to average power ratios.

3.3 Results with 75kW as power limit

In this paragraph there are the results of the simulations of the passive loading control with power limit of 75 kW. In figure 25 the average mechanical power is represented as a function of the $\boldsymbol{B_L}$ coefficient.

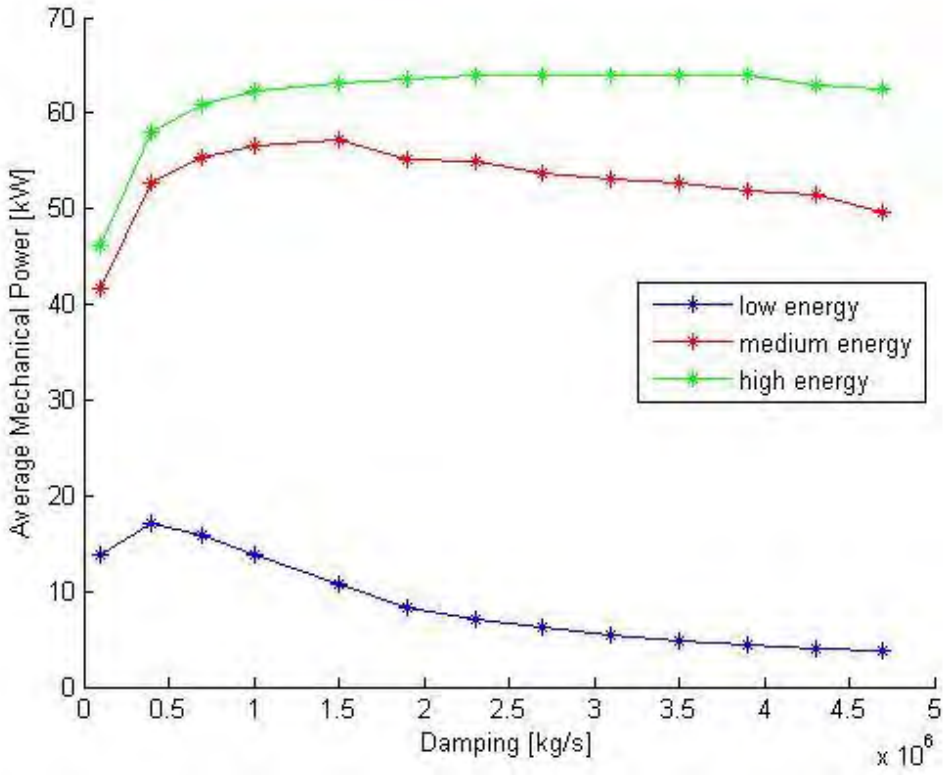

Figure 25 - Diagram Mechanical Power-Damping with 75 kW as power limit

There are the three cases of low, medium and high energy (sea states) respectively. Like the previous case without constraints- for each energy sea state there is a peak of the average power corresponding to a specific damping coefficient applied. But in this case the peak of average mechanical power has been reduced, a lot in the medium and high energy sea state, of almost nothing in the low energy sea state. The $\boldsymbol{B_L}$ coefficient that allows to obtain the maximum average mechanical power changes (in particular increases) in the high and medium energy sea state, instead, in the low energy sea state, it doesn't change. In the next figure the maximum torque in module, the maximum average mechanical power and the maximum PTO force in module are shown using different values of the damping coefficient as it has been done in the previous paragraph. The red line of the medium energy sea state is not visible because it is overlying by the high energy sea state for all the $\boldsymbol{B_L}$ coefficients taken into consideration.

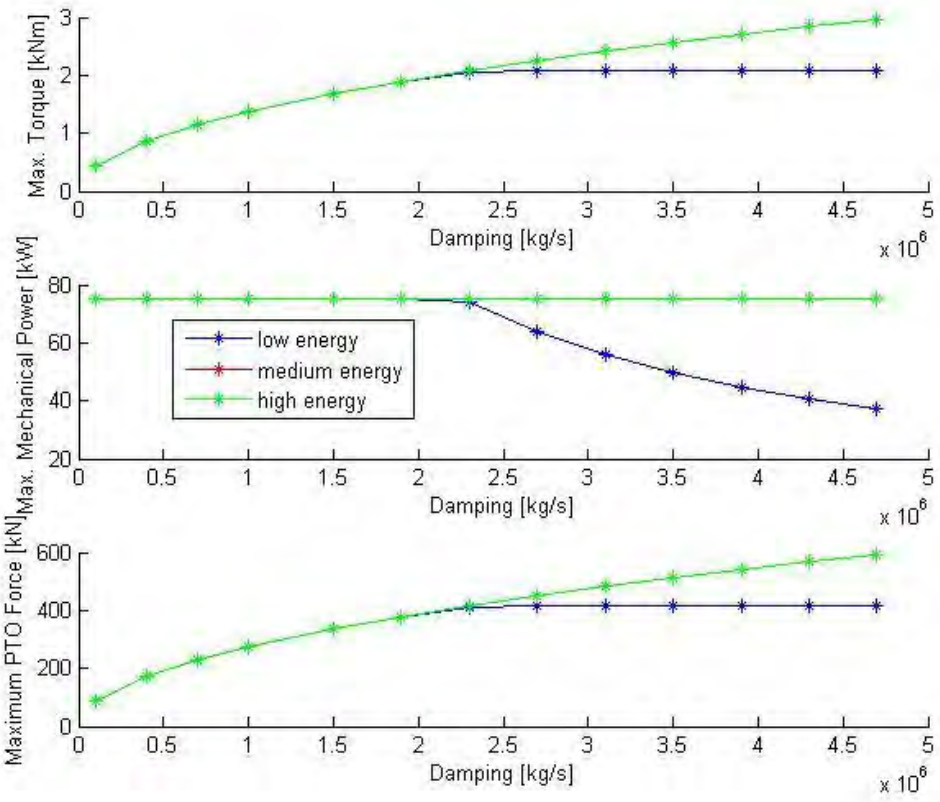

Figure 26 - Diagram Maximum values of Torque, Mechanical Power, PTO force with 75kW as power limit

The diagram of the maximum average mechanical power gives useful information about the effect of the power limit. Therefore it is deduced that for the low energy sea state the power limit is reached up to $\boldsymbol{B_L}$ =2*10^6 kg/s and after that value, for greater values of the $\boldsymbol{B_L}$ coefficient, the maximum mechanical power decreases. Instead, in the other energy sea states, the power limit of 75 kW is reached for all the $\boldsymbol{B_L}$ coefficients applied. In the previous figure it can be noticed that the maximum PTO force in module increases, if the power limit during the 900 seconds of simulation is achieved, increasing the damping coefficient applied (the values of the torque are equal to the values of the force divided 200). This concept is justified by the following equations considering one energy sea state. $\boldsymbol{P_{mecc}}$ is the mechanical power and, as explained in the second chapter, $\boldsymbol{F_L}$ is the PTO force. The equation (9) is valid when the power limit is not achieved and the (10) when the power limit is reached during the simulation.

$$\boldsymbol{P_{mecc}} = \mathbf{F_L(t)} * \boldsymbol{\dot{s}(t)} = \mathbf{B_L} * (\boldsymbol{\dot{s}(t)})^2 \quad \textbf{(9)}$$

$$\mathbf{F_L}(\boldsymbol{B_L}, \boldsymbol{t_{1\ldots x}}) = \frac{\boldsymbol{P_{lim}}}{|\boldsymbol{\dot{s}}(\boldsymbol{B_L}, \boldsymbol{t_{1\ldots x}})|} = \boldsymbol{max}\mathbf{F_L}(\boldsymbol{B_L}) \quad \textbf{(10)}$$

As it is confirmed by figure 38 in the next chapter for a $\boldsymbol{B_L}$ coefficient applied the maximum module of the PTO force ($\boldsymbol{max}\mathbf{F_L}(\boldsymbol{B_L})$) is reached exactly when the power limit is activated or deactivated during the 900 seconds of simualtion (in these istants $\boldsymbol{t_{1\ldots x}}$). Thus $|\dot{\boldsymbol{s}}(\boldsymbol{B_L}, \boldsymbol{t_{1\ldots x}})|$ is the module of the velocity of the buoy when the maximum module of the PTO force is achieved for a $\boldsymbol{B_L}$ coefficient. Whether the $\boldsymbol{B_L}$ coefficient increases, the power limit is reached for a lower velocity (the equation (9) justified it). Therefore a lower value of $|\dot{\boldsymbol{s}}(\boldsymbol{B_L}, \boldsymbol{t_{1\ldots x}})|$ involves a higher value of the maximum PTO force ($\boldsymbol{max}\mathbf{F_L}$). This justified the fact that the module of the maximum PTO force increases with an increment of the $\boldsymbol{B_L}$ coefficient.

Another interesting observation of figure 26 is that, excluding the points when the power limit is not achieved in the low energy sea state, the maximum PTO force in module is equal for all the energy sea states. The next equations confirm this concept. When $\boldsymbol{P_{mecc}}<\boldsymbol{P_{lim}}$ the equation (9) is confirmed. Thus the velocity of the buoy, in the instants in which the power limit is activated or deactivated, is directly proportional to the root of the power limit through the following equation:

$$\dot{\boldsymbol{s}}(\boldsymbol{B_L}, \boldsymbol{t_{1\ldots x}}) = \pm\sqrt{\frac{\boldsymbol{P_{lim}}}{\boldsymbol{B_L}}} \tag{11}$$

The equation (11) can be inserted in the equation (10) and, after several semplifications, it is obtained:

$$\boldsymbol{maxF_L}(\boldsymbol{B_L})=\sqrt{\boldsymbol{P_{lim}} * \boldsymbol{B_L}} \tag{12}$$

It is proved that the maximum module of the PTO force is equal for each energy sea state and it depends on the power limit and on the $\boldsymbol{B_L}$ coefficient (obviously if the power limit is reached during the 900 s of the simulation). The consideration that have been made are the same for the maximum module of the torque (the values of the torque are equal to the values of the force divided 200). Below the dimensional analysis of the previous equation is shown:

$$\sqrt{\left(\boldsymbol{W} * \frac{\boldsymbol{Kg}}{\boldsymbol{s}}\right)} = \sqrt{\left(\boldsymbol{N} * \frac{\boldsymbol{m}}{\boldsymbol{s}}\right) * \frac{\boldsymbol{Kg}}{\boldsymbol{s}}} = \sqrt{\boldsymbol{N} * \boldsymbol{Kg} * \frac{\boldsymbol{m}}{\boldsymbol{s^2}}} = \sqrt{\boldsymbol{N^2}} = \boldsymbol{N} \tag{13}$$

In figure 27 the diagrams of the maximum buoy position and maximum buoy velocity are shown. Also here the trend is different compared to the case without power limit. The maximum buoy position in the case of low energy (sea state) tends to be very low when the damping coefficient overcomes 2*10^6 Kg/s. For this reason exceeding the value of 2*10^6 Kg/s, in the case of low energy (sea state), hasn't real physical meaning.

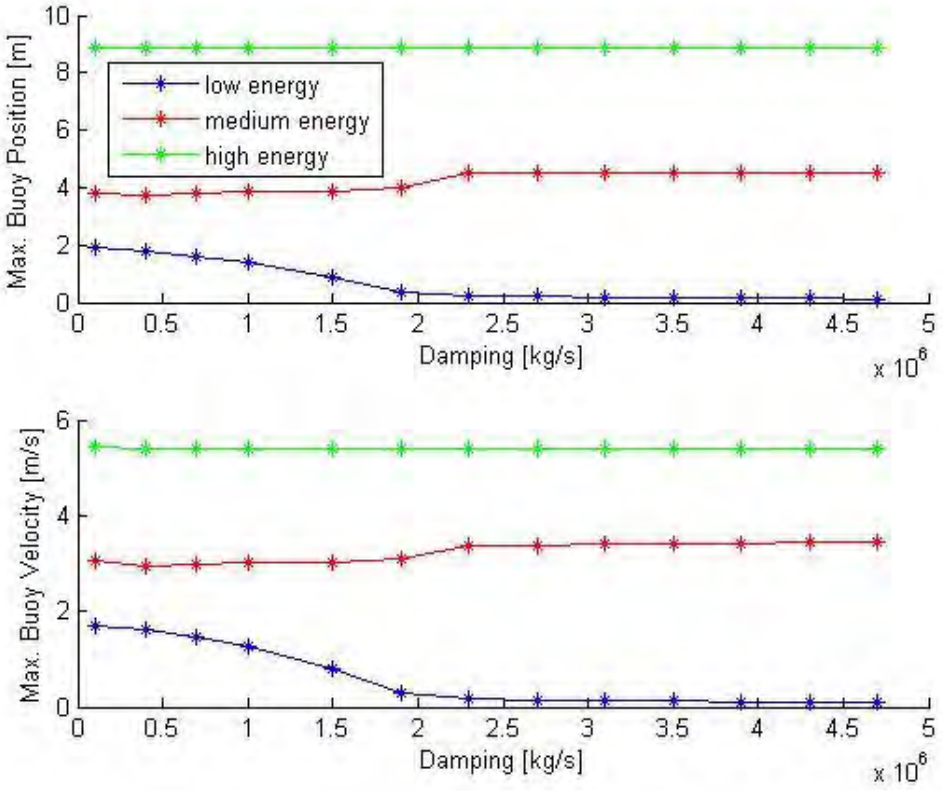

Figure 27 - Diagram Maximum Values of Buoy Position and Velocity with 75kW as power limit

Instead in the high and medium energy sea state increasing the $\boldsymbol{B_L}$ coefficient the maximum position and velocity of the buoy is more or less steady.

With the addition of the power limit it has been measured also the root mean square (RMS) of the PTO force during the 900 seconds of simulation. It is shown in figure 28. It can be seen that the RMS PTO force of the high energy (sea state) is lower than the RMS PTO force of the medium energy (sea state). This is due to the fact that in the high energy sea state the power limit is reached more times compared the medium energy sea state during the 900 seconds of simulations. Consequently the equation (6), during the 900 seconds of simulation, is almost always valid (in the high energy sea state) reducing the RMS of the PTO force. Instead in the medium energy sea state the power limit is achieved fewer times compared the high energy sea state and as consequence the equation (3) will be valid for more time during the 900 seconds of simulations. Therefore it can be said that the effect of the power limit is more evident in the high energy sea state compared the medium energy sea state, the lower value of the RMS of the PTO force (and also the RMS of the Torque) is a consequence.

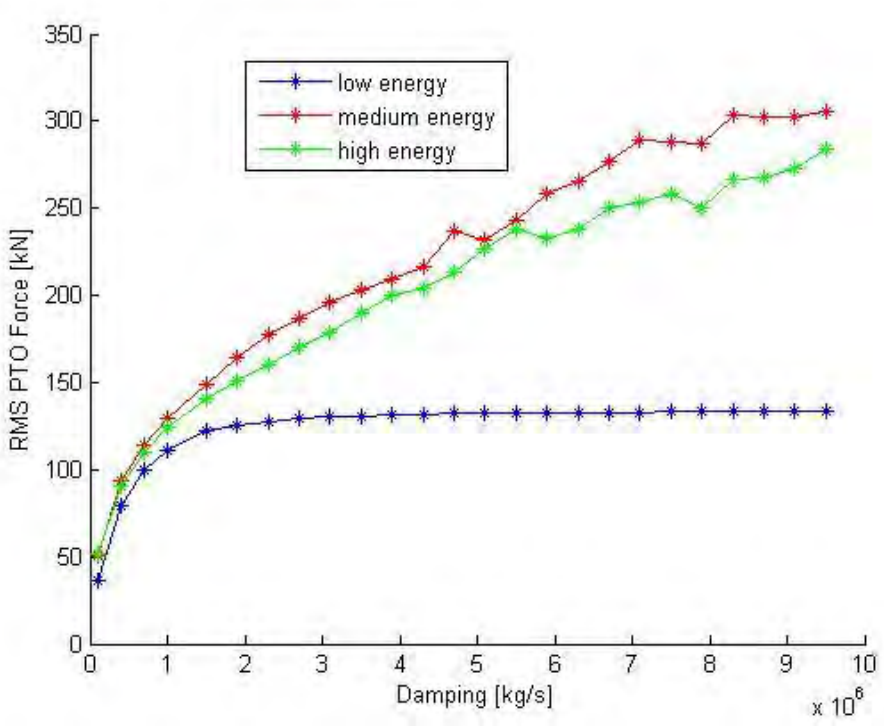

Figure 28 – Diagram of the root mean square of the PTO force with 75kW as power limit

In the next page there is a table that summarizes the main results of the simulations with 75kW as power limit. Like in the case without constraints for each energy sea state the B_L coefficient with which the maximum average mechanical power is obtained is taken into consideration. The power limit implies a reduction of the average mechanical power around the 75 % in the high energy sea state and around the 50 % in the medium energy sea state. This disadvantage is compensated by the fact that the peak to average power ratio and the maximum torque reached have been reduced a lot for all the energy sea states. In the low energy case the peak to average power ratio is still high and a lower power limit is suggested. For the other two energy sea states the electronic devices and the electrical machine can be dimensioned for the peak values of power, the peak to average power ratios are close to one. The only inconvenient is the maximum torque that is too high for an electrical machine of 75kW as rated power. The addition of the torque limit could be a solution. In the next paragraphs the power limit will be increased with the goal to increase the average power and at the same time try to keep the peak to average power ratio low.

Table 4 – Main results of the simulations with 75 kW as power limit

	Max average power [kW]	Damping [kg/s]	Max PTO Force [kN]	Max Torque [kNm]	Max Power [kW]	Max Buoy Position [m]	Max buoy velocity [m/s]	Peak to average power ratio
low energy sea state	17	400000	173.2	0.866	75	1.8	1.6	4.41
medium energy sea state	57.3	1500000	335.4	1.677	75	3.9	3	1.31
high energy sea state	64	2700000	450	2.25	75	8.85	5.4	1.17

3.4 Results with 100 kW as power limit

Also the power limit of 100 kW has been applied and the diagrams are shown in this paragraph. Figure 29 shows the average mechanical power for different values of the $\boldsymbol{B_L}$ coefficient.

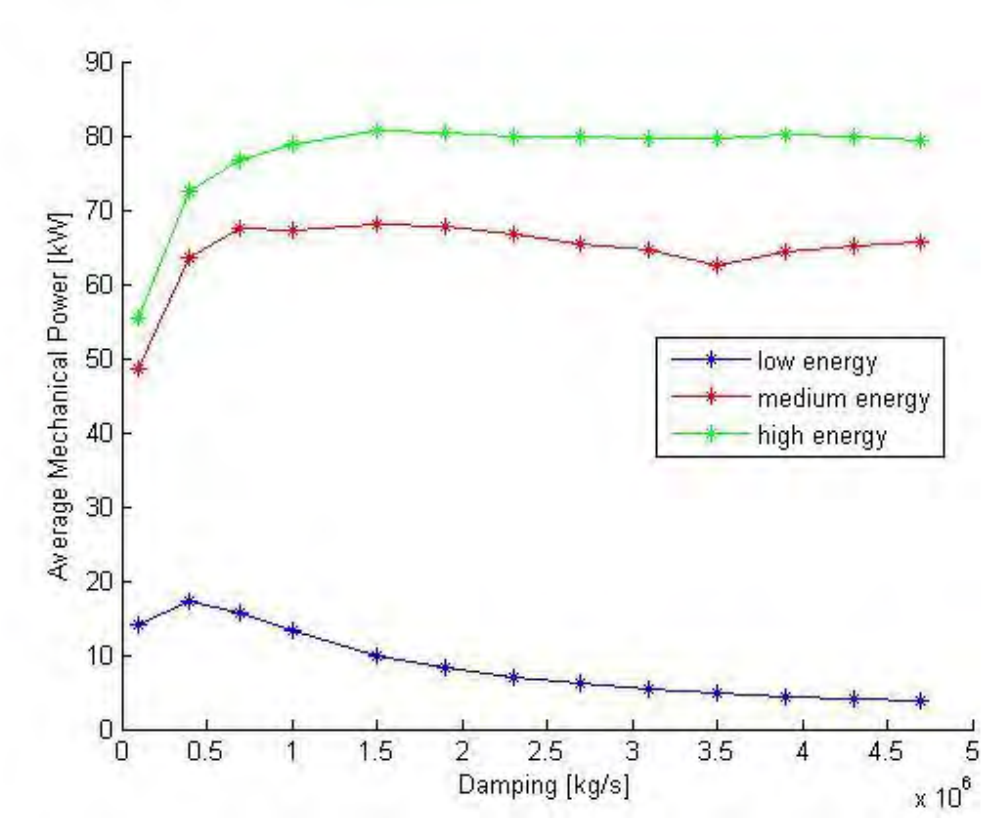

Figure 29 - Diagram Mechanical Power-Damping with 100 kW as power limit

The situation is unchanged, compared the previous power limit, in the low energy sea state. Instead, in the medium and high energy sea state the peaks of average mechanical power are greater. In the high energy case the $\boldsymbol{B_L}$ coefficient that allows to obtain the maximum average mechanical power (it is 1500000 kg/s as in the medium energy sea state) also changes. Subsequently in the next figure the diagram of the maximum PTO force in module, maximum mechanical power and maximum torque with the damping coefficient on the x axis are shown. The trend of the diagrams is as in the previous power limit and then also the considerations that have been made in the previous paragraph are valid. Obviously the maximum mechanical power is not anymore 75kW, but 100kW and the power limit is not achieved in the low energy case for values of the $\boldsymbol{B_L}$ coefficient greater than 1500000 kg/s. From figure 30 it can be noticed that if the power limit is reached for each damping coefficient the maximum PTO force (and torque) is increased compared the previous power limit. The equation (12) justifies it: for a given $\boldsymbol{B_L}$ coefficient if the power limit is greater also the maximum PTO force (torque) is greater.

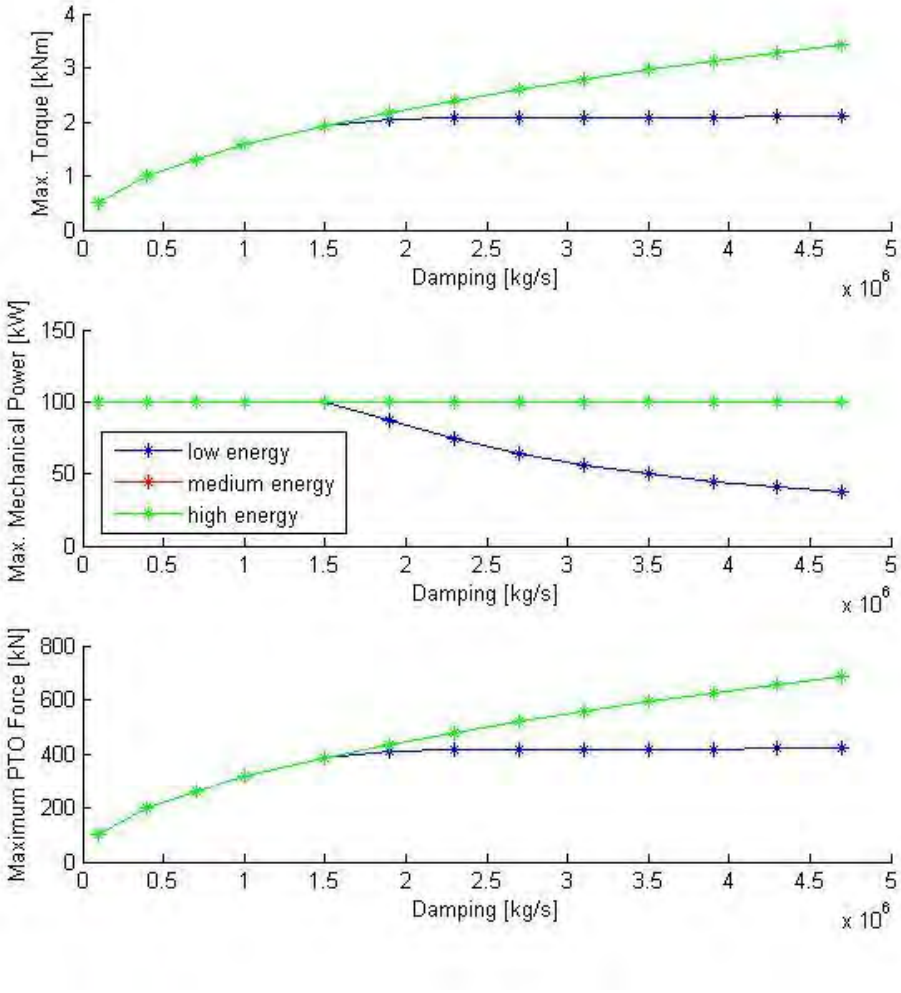

Figure 30 - Diagram Maximum values of Torque, Mechanical Power, PTO force with 100kW as power limit

Also in this paragraph the graphs of the maximum position of the buoy and maximum velocity of the buoy are plotted and are shown in figure 31. The considerations are the same that have been made with 75 kW as power limit.

Another interesting diagram is plotted in the next page in figure 32 which regards the root mean square of the PTO force considering the 900 seconds of simulation. The values of the RMS in the high and medium energy sea state are much greater compared the previous power limit. This is a consequence of the increment of the power limit and it confirms that the power limit is active for less time compared the previous paragraph and then the force is reduced for less time (in the medium and high energy sea state). The situation remains more or less unchanged in the low energy case. The trend of the RMS of the torque is not shown because it is the same as the RMS PTO force.

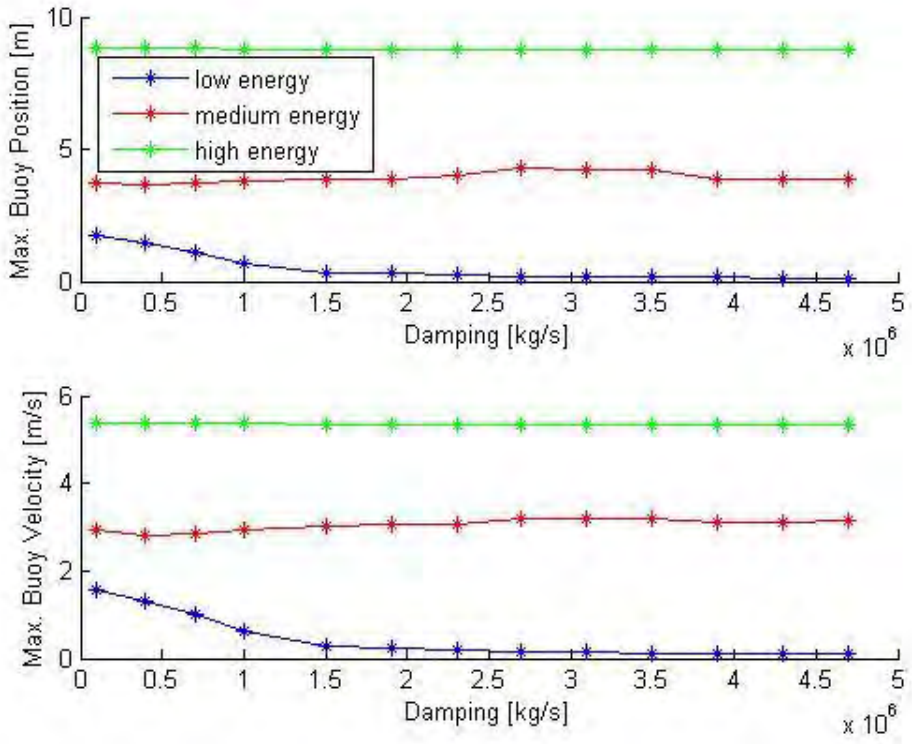

Figure 31 - Diagram Maximum Values of Buoy Position and Velocity with 100kW as power limit

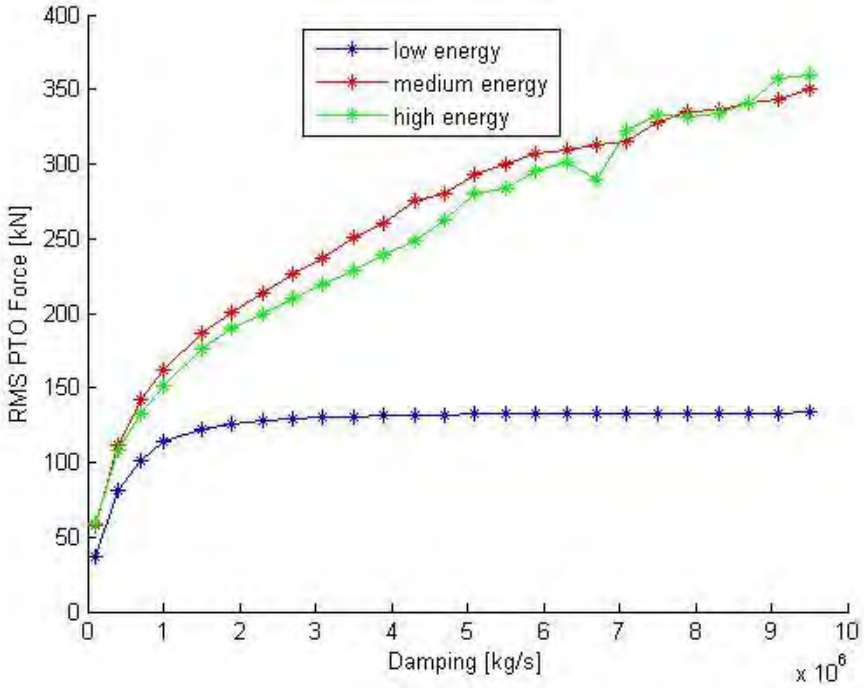

Figure 32 - Diagram of the root mean square of the PTO force with 100kW as power limit

Table 5 – Main results of the simulations with 100 kW as power limit

	Max average power [kW]	Damping [kg/s]	Max PTO Force [kN]	Max Torque [kNm]	Max Power [kW]	Max Buoy Position [m]	Max buoy velocity [m/s]	Peak to average power ratio
low energy sea state	17.34	400000	200	1	100	1.5	1.3	5.77
medium energy sea state	67.9	1500000	387	1.936	100	3.8	3	1.47
high energy sea state	80.7	1500000	387	1.936	100	8.8	5.35	1.23

Also with 100 kW as power limit the table that summarizes the main results has been made and it is shown in the previous page. There are the data of the $\boldsymbol{B_L}$ coefficient that imply the maximum average mechanical power for each energy sea state. For the low energy case the value of the peak to average power ratio is worse than with the lower power limit. Instead, in the medium and high energy sea state, it is more convenient this power limit than 75kW because the average mechanical power is increased and also here the peak to average power ratio is still close to one. The only disadvantage in the medium and high energy case is the value of the maximum torque (almost 2 kNm) which is quite high for a common electrical machine of 100 kW as rated power. The machine would be feasible, but it involves a much higher investment. A limitation of the torque could resolve this problem and allows the addition of the electrical machine without a waste of money. Subsequently it will be applied a greater limit of power (200kW) with the aim to obtain higher values of the average mechanical power.

3.5 Results with 200 kW as power limit

In this paragraph the results of the simulations of the greater value of power limit are shown. The first graph is the average mechanical power in function of the $\boldsymbol{B_L}$ coefficient

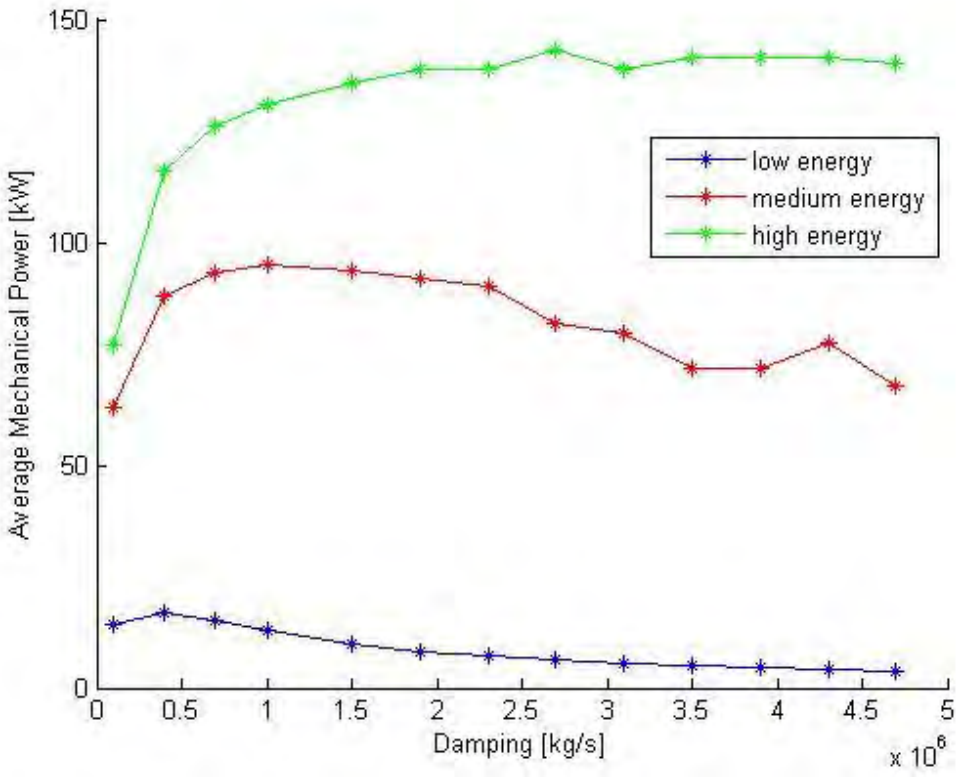

Figure 33- Diagram Mechanical Power-Damping with 200 kW as power limit

In the low energy sea state the values are almost unchanged compared the previous power limit. Instead, in the other two energy cases, the values of average mechanical power are greater and in the high energy sea state overcome 100 kW. As previously also with the power limit of 200 kW the diagrams of the maximum PTO force, of the maximum mechanical power and of the maximum torque are plotted and they are shown in figure 34. It can be noticed that the power limit of 200 kW in the low energy sea state is achieved only with the first two $\boldsymbol{B_L}$ coefficients applied. Regarding the high and medium energy cases the trend of the maximum PTO force in module is the same of the previous power limits, therefore the considerations are equal. The only difference is that the module, for each $\boldsymbol{B_L}$ coefficient, is greater as it is justified by the equation (12). Also as in the previous paragraphs the diagram of the maximum PTO force is the same for the maximum torque, only the values on the y axis changes (they are divided by 200).

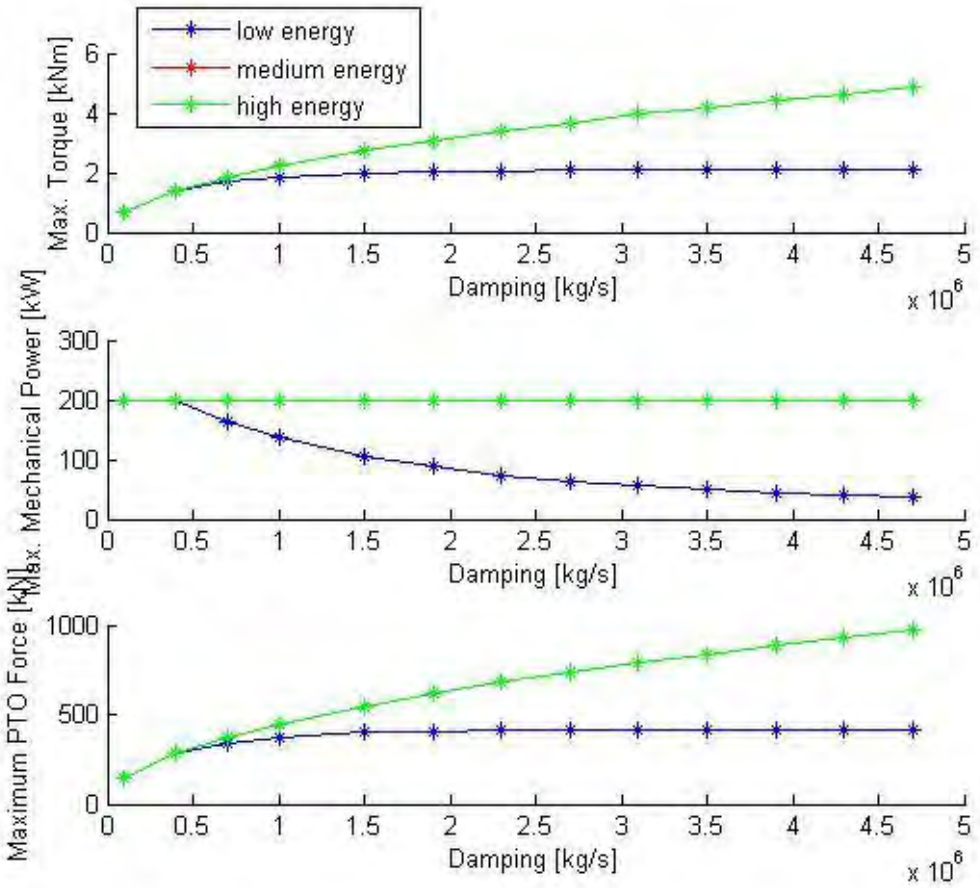

Figure 34 - Diagram Maximum values of Torque, Mechanical Power, PTO force with 200kW as power limit

The diagrams of the maximum buoy position and velocity are plotted in figure 35. The trend is akin to the power limits of 75 and 100 kW. Excluding the case of low energy, the maximum position and maximum velocity tend to be constant varying the $\boldsymbol{B_L}$ coefficient applied during the 900 seconds of simulation. To understand better the behaviour of the system, like it has been made with the other power limits, it is shown the diagram of the root mean square of the PTO force in figure 36. Unlike in the other cases it can be noticed that, for all the $\boldsymbol{B_L}$ coefficients applied, the RMS PTO force of the high energy case is greater than the RMS PTO force of the medium energy case. Like it would be without constraints. It means that the increase of the power limit involves a reduction of the time in which (during the 900 seconds of simulation) the power limit is active and the PTO force is reduced especially in the high energy sea state. Instead previously, with 75 and 100 kW as power limit in the high energy sea state, the time of activation of the power limit was very high compared the medium energy case and as consequence the RMS PTO force of the high energy case was lower than the RMS PTO force of the medium energy case.

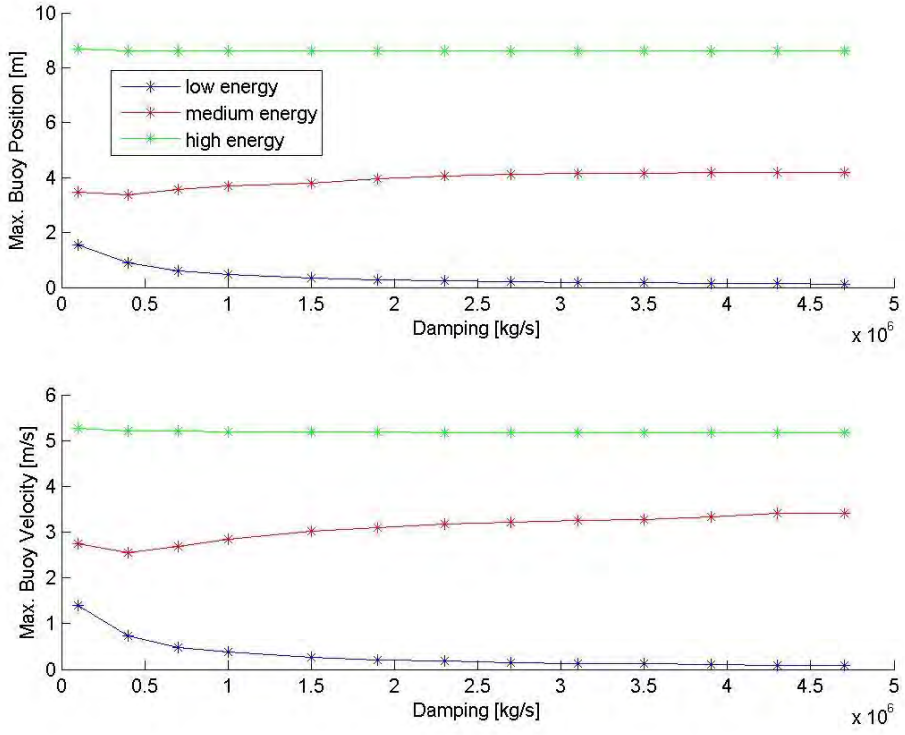

Figure 35 - Diagram Maximum Values of Buoy Position and Velocity with 200kW as power limit

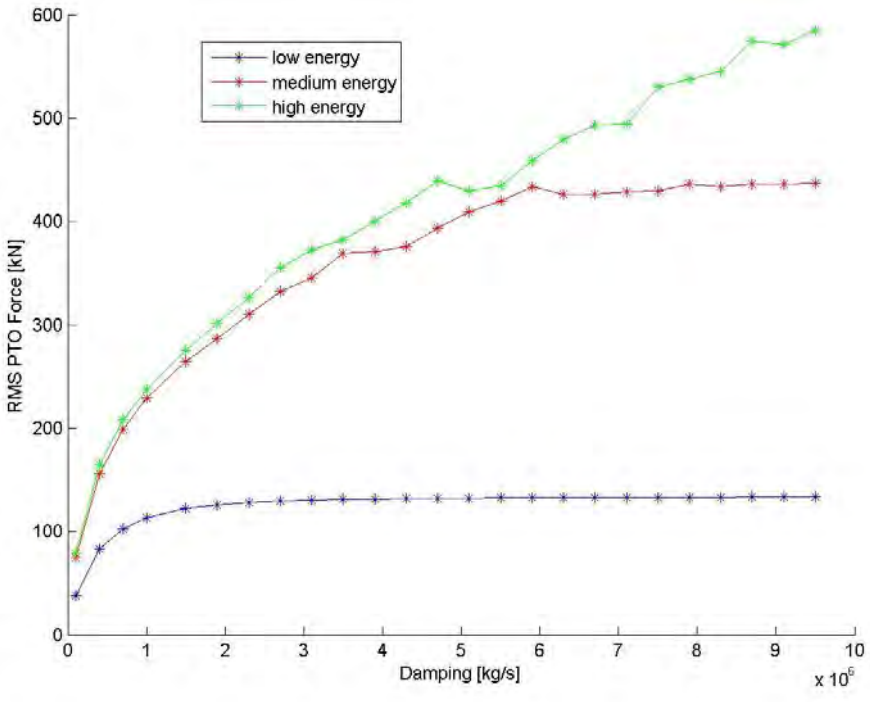

Figure 36 – Diagram of the root mean square of the PTO force with 200kW as power limit

Table 6 - Main results of the simulations with 200 kW as power limit

	Max average power [kW]	Damping [kg/s]	Max PTO Force [kN]	Max Torque [kNm]	Max Power [kW]	Max Buoy Position [m]	Max buoy velocity [m/s]	Peak to average power ratio
low energy sea state	17.1	400000	283	1.415	200	0.9	0.7	11.7
medium energy sea state	95	1000000	447	2.24	200	3.7	2.9	2.1
high energy sea state	143	2700000	735	3.68	200	8.6	5.2	1.4

From the table of the previous page can be made interesting observations (the data of the $\boldsymbol{B_L}$ coefficient, that imply the maximum average mechanical power for each energy sea state, are shown). The peak to average power ratio overcomes 10 in the low energy sea state, as consequence if in a location the low energy sea states prevail over the medium and high energy ones for sure this power limit would not be convenient. In the medium energy case the average power is increased of the 40 percent compared the previous power limit (100kW), but the peak to average power ratio is great and overcomes 2. For this reason, in a location with most of the sea states of medium energy, it is not convenient to use an electrical machine with 200 kW as maximum power. As a matter of fact the electronic devices and the electrical machine would be sized for a double power compared the average mechanical power. Instead in the high energy sea state the average mechanical power is increased of -almost the 80 percent, compared the previous power limit, and the peak to average power ratio is kept close to 1. Therefore, in a location with a lot of high energy sea states compared the medium and low energy ones, the power limit of 200 kW is the most advantageous as power limit: it allows to obtain a greater average mechanical power without oversize the electronic devices and the electrical machine (because they are dimensioned for the peak value of power that is 200 kW). Also here as previously the maximum value of the torque is an issue, because it is too high (almost 4 kNm) and it should be decreased with a torque limit equal to the value of the maximum torque of the electrical machine.

3.6 Final considerations

At this point some considerations must be done. All the power limits applied are not convenient for a specific location with many low energy sea states, because the peak to average power ratio is very high. A reduction of the value of the power limit could be a solution, but it is not made in this thesis. If in the scatter diagram of the location the medium energy sea states prevail over the low and the high energy ones the first two power limits are feasible, in fact in the medium energy sea state the peak to average power ratio is close to one for both the cases. But the more convenient is the second one (100kW as power limit), because the average mechanical power is much higher. Lastly in a specific location wherein the high energy sea states prevail over the medium and low energy ones, even if all the power limits are feasible, the best is the case with 200 kW as power limit because it gives the highest values of average mechanical power and at the same time keeps the peak to average power ratio low. The next step will be to add a torque limit in the Simulink model that matches the maximum torque that can be provided by the electrical machine. Obviously this step can be done only if the data of the machine are known.

4. THE ELECTRICAL MACHINE (PMSG)

4.1 Introduction

In this chapter the electrical machine has been added to the Simulink model. Design the generator, control the electrical machine to obtain a certain behaviour and evaluate the performance for each energy sea state of such generator are the goals. In figure 37 a general overview of the model used in all the simulations of this chapter (except in the simulations of paragraph 4.2) is shown. As it can be seen, the connection to the electric grid is not considered and only an inverter has been used. On the DC (direct current) side of the inverter an ideal DC voltage source is present. In the figure 37 the reference value of $\boldsymbol{F_L}$ is represented by $\boldsymbol{F_L}^*$.

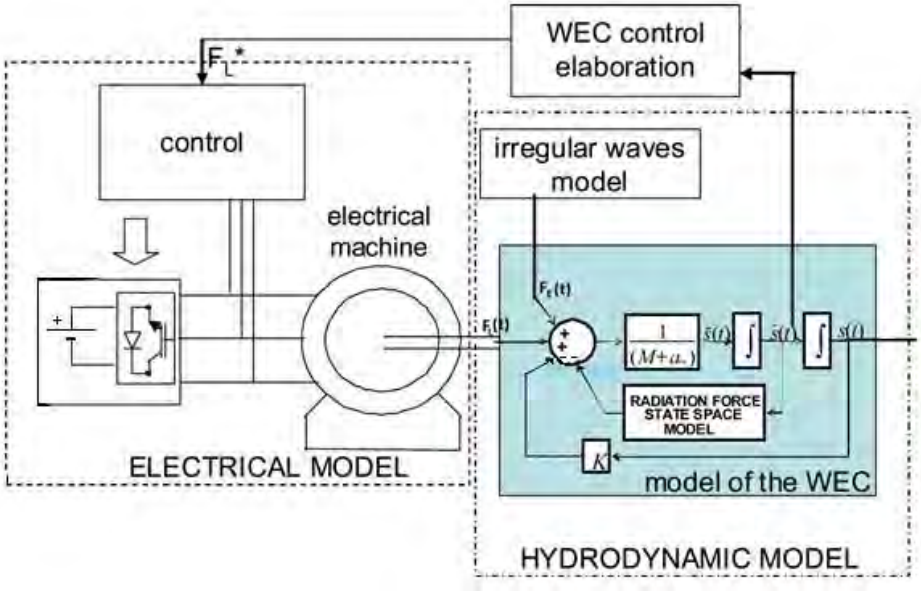

Figure 37- Hydrodynamic and electric model of the WEC [34]

With the goal to produce electric energy 100 kW has been chosen as a trade-off for the power limit. The table 5 shows the data of the maximum values for which the electrical machine must be dimensioned for the low, medium and high energy sea state respectively. As a reference case (for the sizing of the generator) the medium energy sea state has been chosen. The value of the maximum torque is quite high for a common electrical machine that has the rated power around 100kW. It is possible to size the electrical machine for 2 kNm as nominal torque, but it involves a remarkable increment of the investment (compared a common generator with 100 kW as rated power). Furthermore it involves a waste of money because, as it is shown in figure 38, the maximum values of torque are achieved for short time during the period of a the wave (this happens for all the waves in the 900s of simulation and for any $\boldsymbol{B_L}$ coefficient).

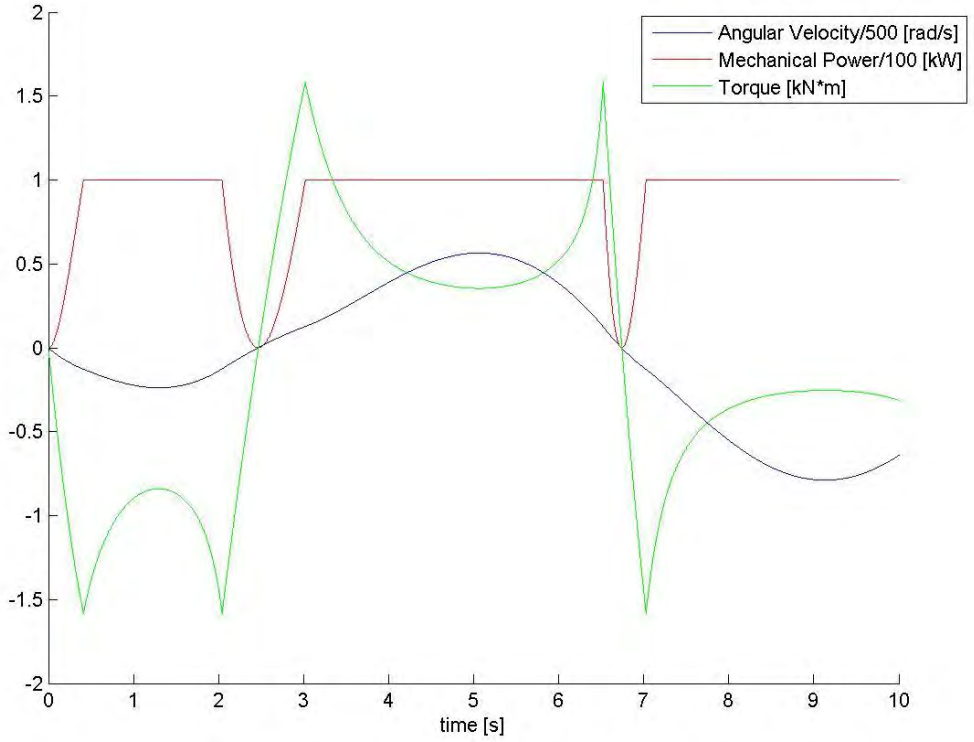

Figure 38 – Angular velocity, mechanical power and torque during 10 seconds of simulation with 100 kW as power limit and B_L=1000000 kg/s (medium energy case)

For that reason an electrical machine with a nominal torque (850 Nm) lower than the maximum value of torque (2 kNm), achieved during 900 s of simulation, has been chosen. The data and information of the generator used in this thesis are shown in paragraph 4.3 in table 8. Before showing the results obtained of the model represented by figure 37, in the following paragraphs the limitation of the torque will be introduced and the control of the electrical machine explained.

4.2 Limitation of the torque

In the model, in accordance with [14], a torque limit equivalent to the value of the maximum torque capability of the electrical machine must be introduced. The torque limit in the Simulink model is introduced simply adding a saturation block (with the upper limit equal to 850 Nm and the lower limit equal to -850 Nm) to the torque which is applied by the PTO, irrespective of the power limit. Up to now the torque limit and the power limit has never been applied at the same time. For this reason, before introducing the electrical machine in the model, the module of the torque limit equal to 850 Nm and the power limit of 100 kW applied at the same time have to be tested for each energy sea state considering the generator ideal as in the previous chapter. In this paragraph the results of the simulations are shown with the goal to

understand better the behaviour of the system and to find the B_L coefficient for each energy sea state that gives the maximum average mechanical power. In this chapter only in the simulations of this paragraph the electrical machine is not considered in the Simulink model and it is like to have in the system an ideal generator without losses able to follow perfectly the torque reference.

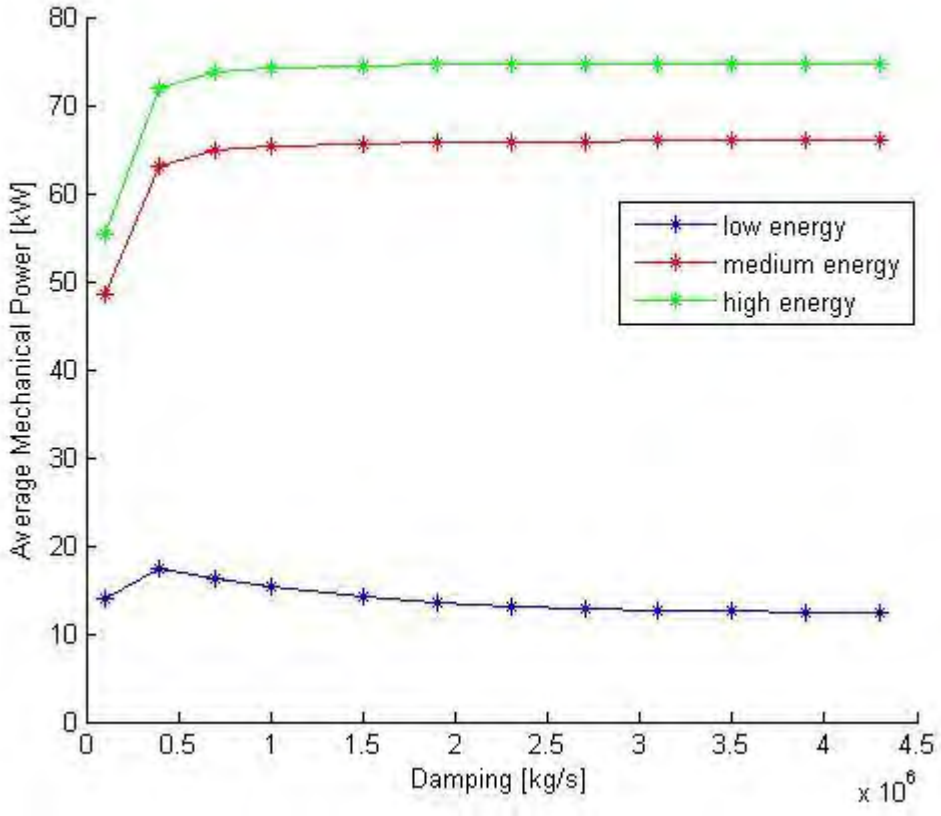

Figure 39 - Diagram Mechanical Power-Damping with 100 kW as power limit and 850 Nm as module of the torque limit

Figure 39 represents the average mechanical power for several damping coefficients applied. In the medium and high energy cases the trend is similar to the average mechanical power in the case with only the power limit applied, but the average power is more steady from B_L equal to 700000 kg/s. Also in the low energy sea state the trend is akin to figure 29, but in this case the addition of the torque limit imposes the average mechanical power to be higher than 10 kW also for high B_L coefficients. Subsequently in figure 40 the maximum PTO force, the maximum mechanical power and the maximum torque are plotted. In the three diagrams the three energy sea states are overlying. The maximum torque has a value always equal to 850 Nm, excluding the first B_L coefficient, it means that the torque limit is activated from the second damping coefficient. The maximum mechanical power is always 100 kW for all the energy sea states, which means that the power limit is (at least partly) activated during all the energy sea states and for all the B_L coefficients.

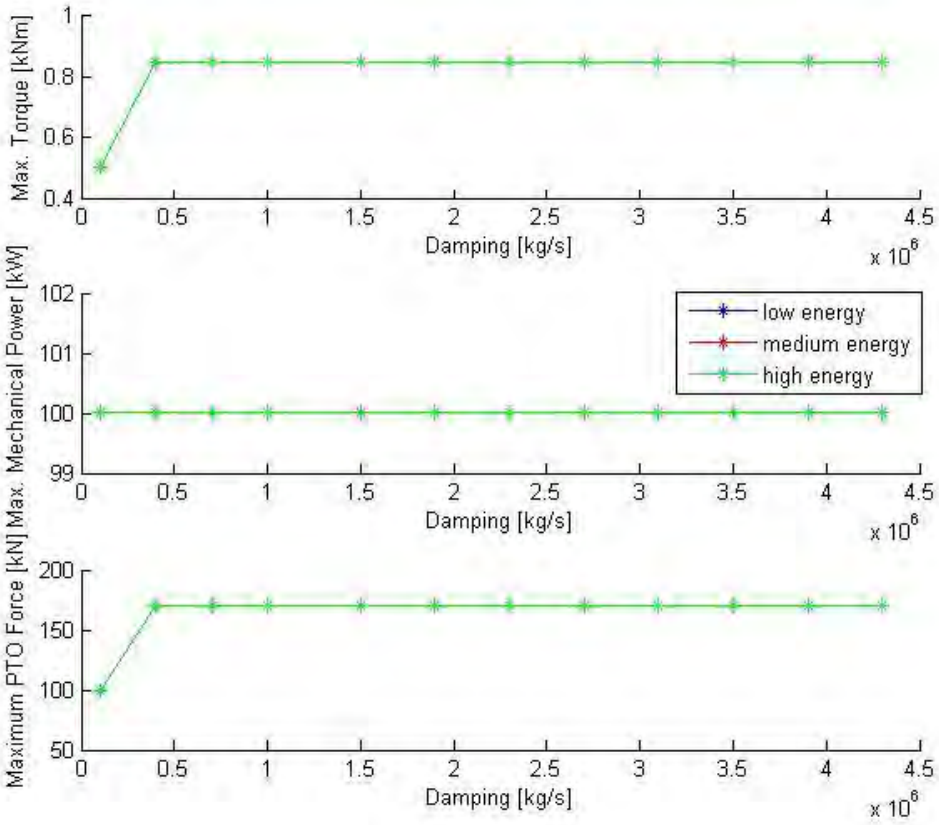

Figure 40 - Diagram Maximum values of Torque, Mechanical Power, PTO force with 100 kW as power limit and 850 Nm as module of the torque limit

In figure 41 in the next page the diagrams of the maximum buoy position and maximum buoy velocity are plotted as it has been done without the torque limit. The addition of the torque limit involves a constant trend for all the energy sea states. Another interesting graph, which is important to analyze, is the percentage of torque limit active figure 42 (the percentage of 900 s of simulation that represents the time in which the module of the torque is limited and then equal to 850 Nm). As it can be noticed the highest percentages are in the medium energy sea state, they overcome 20 %. Instead in the high energy case the torque limit is active for less time. This is due to the fact that the addition of the power limit reduces the torque in the high energy sea state for much more time than the medium energy sea state, then the torque limit is activated for fewer time in the high energy case compared the medium energy case.

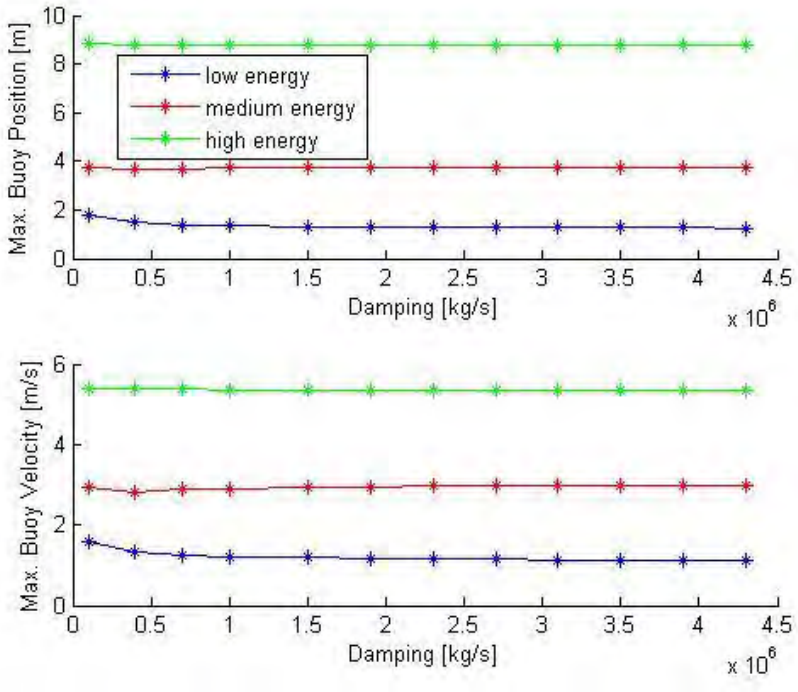

Figure 41 - Diagram Maximum Values of Buoy Position and Velocity with 100kW as power limit and 850 Nm as module of the torque limit

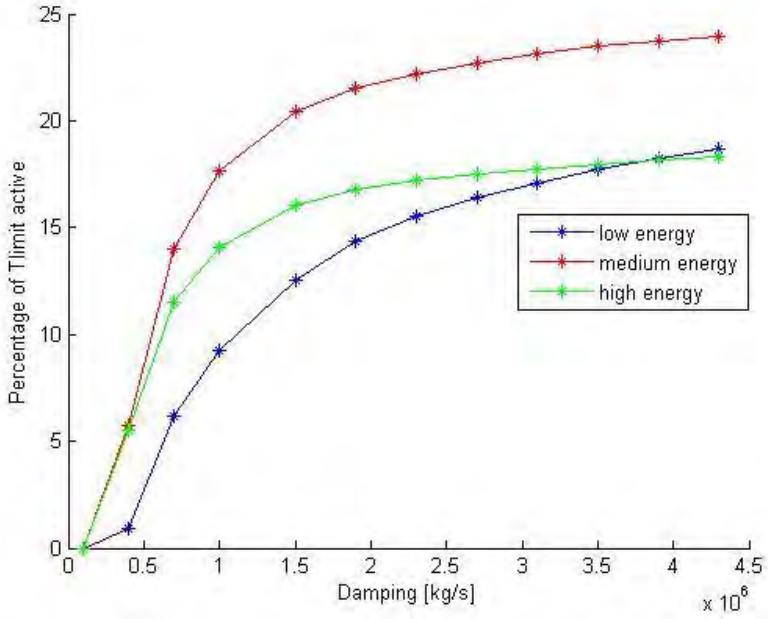

Figure 42 - Diagram Percentage of Torque limit active with 100kW as power limit and 850 Nm as module of the torque limit

Table 7 - Main results of the simulations with 100 kW as power limit and 850 Nm as module of the torque limit

	Max average power [kW]	Damping [kg/s]	Max PTO Force [kN]	Max Torque [Nm]	Max Power [kW]	Max Buoy Position [m]	Max buoy velocity [m/s]	Peak to average power ratio
low energy sea state	17.34	400000	170	850	100	1.5	1.3	5.77
medium energy sea state	66	4300000	170	850	100	3.8	3	1.5
high energy sea state	74.6	3100000	170	850	100	8.8	5.4	1.34

In table 7 for each energy sea state the data of the damping coefficient applied, which involves the highest average mechanical power, are shown. In the low energy sea state the maximum average mechanical power is obtained with the same B_L coefficient as in the paragraph 3.4 and doesn't change with the addition of the torque limit. As consequence the peak to average power ratio is unchanged. The important thing is that the maximum torque, reached during the 900 seconds of simulation, is equal to the value of the maximum torque of the electrical machine. In the high and medium energy sea states the B_L coefficient, that gives the highest value of average mechanical power, changes and it is equal to 4300000 kg/s (in the medium energy case) and 3100000 kg/s (in the high energy case). With the addition of the torque limit the maximum average mechanical power is a little bit lower (in the medium and high energy cases) and as consequence the peak to average power ratio is slightly increased. This is a disadvantage that has to be accepted with the goal to match the maximum torque (reached during the 900 seconds of simulation) with the maximum torque of the electrical machine.

4.3 Control of the permanent magnet synchronous generator (PMSG)

In this thesis a permanent magnet synchronous generator has been used, which is currently the most used solution for the point absorber wave energy converters. Therefore the rotor field is excited by permanent magnets (PMs) and as consequence there aren't copper losses in the rotor. The permanent magnet synchronous generators have also others numerous advantages: high torque to current ratio, large power to weight ratio, high efficiency, high power factor and robustness [18].

Figure 43 – Surface PM rotor (a) and interior PM rotor (b); both the configurations have four poles [19]

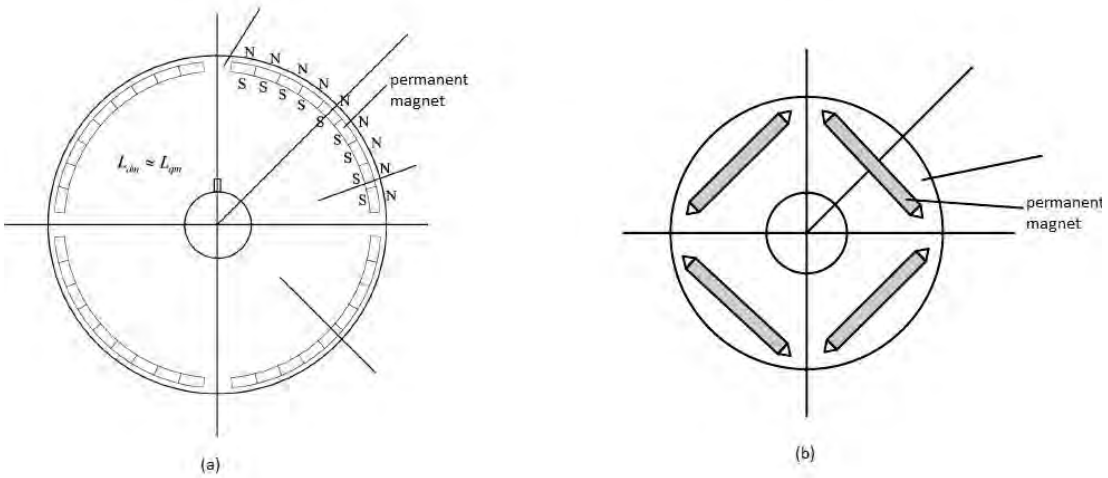

As it is shown in the previous figure, the PMSG (permanent magnet synchronous generator) can have the rotor with *surface permanent magnets* (SPMs – nonsalient pole rotor) or with *interior permanent magnets* (IPMs – salient pole rotor) [19]. The centre of the magnetic pole represents the d-axis (direct axis), which is 90 degrees out of phase behind the q-axis (quadrature axis). The particularity of the SMPMG (surface mounted permanent magnet generator) is that the direct and quadrature-axes inductances are approximately equal, since permeability of the path, that the flux crosses between the stator and the rotor, is equal all around the stator circumference. Instead the quadrature axis inductance ***Lq*** in the interior PMSG can be much larger than the direct axis inductance ***Ld*** [20]. In this thesis a surface mounted PMSG has been used and the data of the generator are shown in table 8.

Table 8 – Data of the generator

Quantity	Value
Nominal power, P_n	80 kW
Nominal torque, T_n	850 Nm
Nominal voltage, V_n	400 V
Nominal current, I_n	120,2 A
Nominal speed, n_n	900 rpm
Number of poles, $2p$	4
Permanent magnet flux, Ψ_{pm}	1,7324 Vs
Stator leakage inductance, L	0,0106 H
Stator resistance, R	0,1 Ω
Maximum power, P_{max}	110 kW
Limit of peak current, I_{lim}	170 A
Limit of peak phase voltage, V_{lim}	470 V

The addition of the power limit involves not only a lower peak to average power ratio, but also less fluctuation in power production and the utilization of an electrical machine with a higher overspeed ratio (the ratio between the maximum speed and the nominal speed of the electrical machine) [25]. As it is shown in figure 38 the electrical machine during the 900 s of simulation must work most of the time in the constant power region of the mechanical characteristic. For this reason an electrical machine with a wide constant power range, as it is shown in the figure 44, has been chosen and as consequence a field-weakening control is needed. The overspeed ratio of the PMSG used in this thesis is almost 6 and is quite high compared a common electrical machine. The reduction of the rated power of the PTO and the utilization of a generator with a high overspeed ratio in a Wave Energy Converter with all electric Power Take Off system is not new. In fact in [25] it has been proposed in a study called “overspeed optimization” (referred to a scatter diagram of a location) which is performed by creating generator models for several overspeed ratios (from 1 up to 50). The study says that the utilization of a PMSG with an overspeed ratio quite high

(between 5 up to 10) involves a high reduction of the investment of the PTO and at the same time a little loss of the energy produced in one year in the specific location.

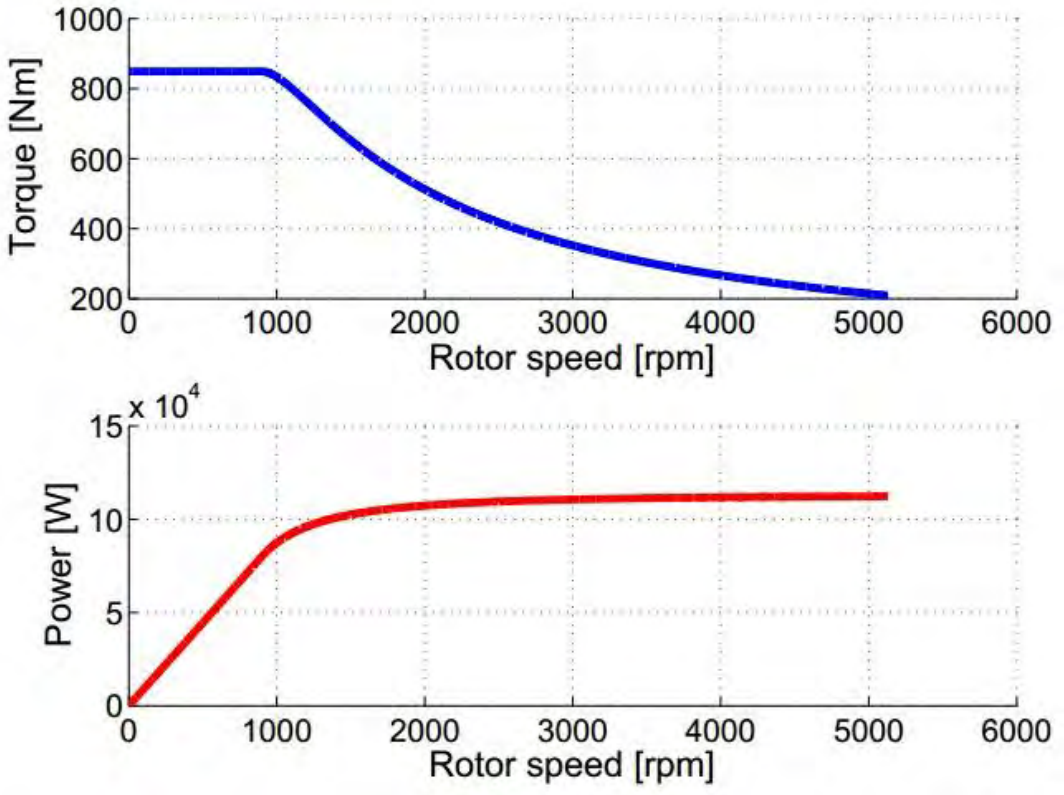

Figure 44 – Mechanical characteristic of the SMPMSG (surface mounted permanent magnet synchronous generator) used in the thesis

4.3.1 Equations and Simulink model

In figure 44 the rotor speed is represented in revolutions per minute ($\boldsymbol{n}$) and it is linked with the angular velocity of the generator ($\boldsymbol{\omega_m}$) by the following equation:

$$\omega_m = \frac{2\pi}{60} n \quad \left[\frac{rad}{s}\right] \tag{14}$$

Before introducing the equations of the control of the PMSG the electromechanical speed ($\boldsymbol{\omega_e}$) in rad/s must be defined:

$$\omega_e = \omega_m p \left[\frac{rad}{s}\right] \tag{15}$$

$\boldsymbol{p}$ is the number of pole pairs, which is equal to 2 in the electrical machine that has been used in the thesis. The equations of the generator are projected on a reference coordinate system rotating synchronously with the magnet flux (the d-q axes), because the goal is to get a dynamical model for the electrical generator which easily

allows to define the control system of the PMSG. As in [21] the dynamic model of electrical machine is equal to:

$$v_d = -R\, i_d - L\, \frac{di_d}{dt} + L\, \omega_e i_q \tag{16}$$

$$v_q = -R\, i_q - L\, \frac{di_q}{dt} - L\, \omega_e i_d + \omega_e \Psi_{pm} \tag{17}$$

L is the generator inductance, R the generator resistance, Ψ_{pm} the permanent magnet flux, ω_e is the electromechanical speed of the generator, v_d is the direct voltage and v_q is the quadrature voltage. Through the applied voltage, as it is shown by the previous equations, it is possible to control the direct (i_d) and quadrature current (i_q). The equation (18) proves which the generator torque can be directly controlled by the i_q [21].

$$T = \frac{3}{2}\, p\, \Psi_{pm} i_q \tag{18}$$

T is the torque of the generator. In the following figure the circuits of the equivalent d and q axes of the generator are shown with the conventions of equation (16) and (17).

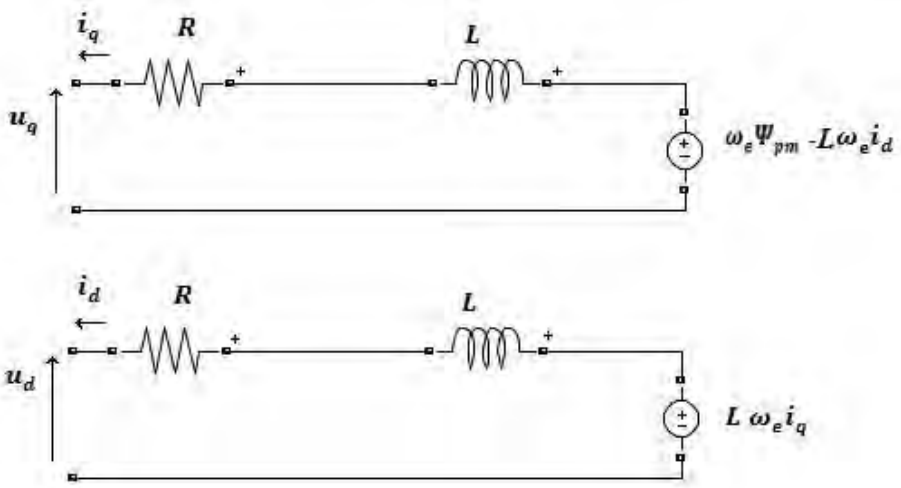

Figure 45 – Equivalent *d* and *q* axes generator circuit

With the goal to control the PMSG a MATLAB-Simulink model has been made, it is shown in figure 46. The torque (T), that has to produce the electrical machine, is represented as ***Torqueref*** and the angular velocity of the generator (ω_m) is expressed as ***ω_nom.*** They are the inputs of the model. The angular velocity of the generator is equal to the buoy velocity divided by the pinion radius (**rw**=0.1 m) and multiplied the gear ratio (**ng**=20).

Figure 46 – Simulink model of the control of the PMSG

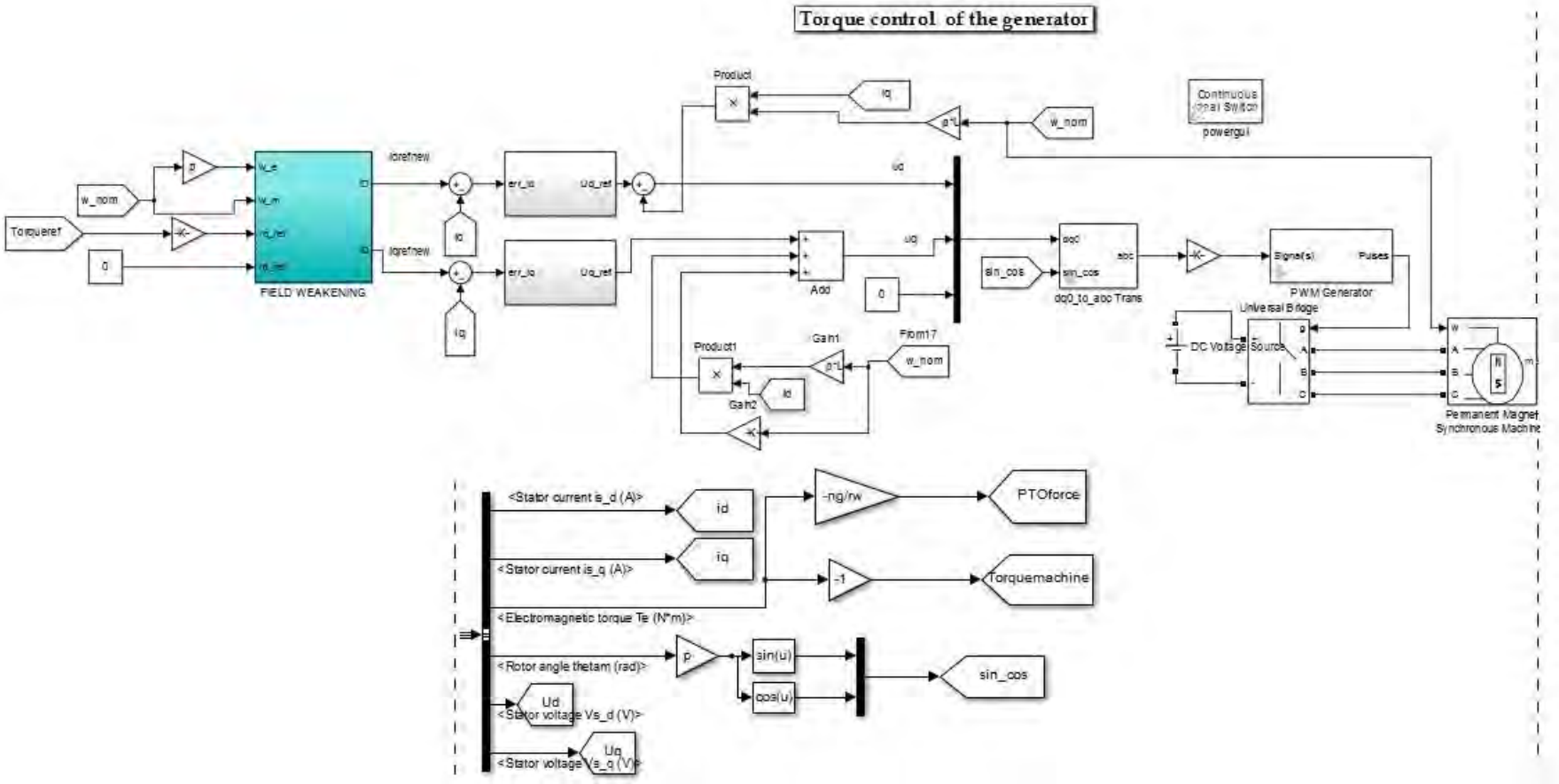

The block of the permanent magnet synchronous machine used in Simulink works as generator when the torque and the angular velocity are different of sign and as motor when they are concordant of sign. For this reason the "motor convention" is applied in the Simulink model: the torque is changed in sign with the aim to use the machine as generator. The equations (16) and (17) in “motor convention” are equal to:

$$\boldsymbol{v_d = R\, i_d + L\, \frac{di_d}{dt} - L\, \omega_e i_q} \quad \textbf{(19)}$$

$$\boldsymbol{v_q = R\, i_q + L\, \frac{di_q}{dt} + L\, \omega_e i_d + \omega_e \Psi_{pm}} \quad \textbf{(20)}$$

In the Simulink model these are the equations used and an ideal three phase inverter (with ideal switches) has been utilized to feed the PMSG. The three phase voltages of the inverter in the reference coordinate system rotating synchronously with the magnet flux are represented by the $\boldsymbol{v_d}$ and $\boldsymbol{v_q}$. They allow to control the direct and quadrature current and therefore also the torque of the electrical machine (which has to be equal to the ***Torqueref*** in each instant of the simulation). The inverter has to be controlled in a way that it imposes to the electrical machine the direct and quadrature voltages required (for the control of the electrical machine). To do it, the field-weakening subsystem and the current control loop (with two PI controllers) have been made (they will be explained and deepened in the next two paragraphs 4.3.2 and 4.3.3). The equations (19) and (20) have been applied in the model and the $\boldsymbol{v_d}$ and $\boldsymbol{v_q}$, that the inverter has to give to the electrical machine, are obtained. They are converted to the reference coordinate system abc (that correspond to the phase voltages which the inverter has to give to the PMSG), after which the three voltages are normalized respect ***Vdc/2*** (half of the voltage of the DC side of the inverter, DC= direct current). These three signals normalized are the input of the block “PWM (Pulse Width Modulation) generator” that has the task to command the switches of the inverter. The DC side of the inverter is supplied by an ideal DC voltage source of 800 V (the connection to the grid will be considered in the next chapter). The value has been chosen in accordance with [22] and with the goal to satisfy the voltage request of the PMSG (the electrical machine has a rated voltage of 400 V). The mechanical input of the electrical machine is $\boldsymbol{\omega_m}$ and the torque of the generator is controlled with the goal to follow the reference torque (***Torqueref***). It means that, in regard the equilibrium of the torques of the system, the viscous friction (**B**) of the electrical machine and the inertia of the rotor (**J**) should be taken into account in the equation of the hydrodynamic model (equation (2)). The inertia of the electrical machine is considered in **M**, that was defined as the mass of the device including the contribution due to the PTO inertia. The viscous friction of the PMSG should be a term directly proportional to the velocity of the buoy, but it is not considered in the model of this thesis.

.

4.3.2 Current control loop and PI controllers

Before introducing the block diagram of current control loop it is mandatory to explain some equations, that allow to obtain the block diagram, and introduce some definitions which help to understand better the system. In equation (19) and (20) there is a cross coupling among the d and q axes because of the terms $\boldsymbol{L\,\omega_e i_q}$ and $\boldsymbol{L\,\omega_e i_d}$. The feed-forward technique allows to avoid the cross coupling, defining the following reference voltages [27] :

$$\boldsymbol{v_{d,ref} = v_d + L\,\omega_e i_q} \quad \textbf{(21)}$$

$$\boldsymbol{v_{q,ref} = v_q - L\,\omega_e i_d - \omega_e \Psi_{pm}} \quad \textbf{(22)}$$

As consequence two independent current loops are obtained, which correspond to two equations of the first order: one of the d-axis and the other one of the q-axis. As in [27] the equations are the following:

$$\boldsymbol{v_{d,ref} = R\,i_d + L\,\frac{di_d}{dt}} \quad \textbf{(23)}$$

$$\boldsymbol{v_{q,ref} = R\,i_q + L\,\frac{di_q}{dt}} \quad \textbf{(24)}$$

The transfer function from the current ***i*** to the voltage ***v*** is defined as [27]:

$$\boldsymbol{\frac{i(s)}{v(s)} = \frac{1}{1+\frac{L}{R}s}\,\frac{1}{R}} \quad \textbf{(25)}$$

$\boldsymbol{\tau}$ is the time constant of the system and it is equal to the ratio between the inductance and the resistance of the PMSG [28] ($\boldsymbol{\tau = L/R}$).
Each current loop is controlled by a PI regulator, which is composed by a proportional gain (***kp***) and an integral term in parallel (***ki/s***) [28]:

$$\boldsymbol{PI = k_p + \frac{k_i}{s} = \frac{k_p\,s + k_i}{s} = k_p\left(\frac{1+\frac{k_p}{k_i}s}{\frac{k_p}{k_i}s}\right) = k_p\left(\frac{1+T_i s}{T_i s}\right)} \quad \textbf{(26)}$$

$\boldsymbol{T_i}$ is defined as the time constant of the controller and it is equal to $\boldsymbol{k_p/k_i}$. The inverter controlled by the PWM involves a time delay which is taken into account by the following transfer function [28]:

$$\boldsymbol{J = \frac{1}{1+Ts}} \quad \textbf{(27)}$$

$\boldsymbol{T_s}$ is the switching time delay of the inverter in seconds and $\boldsymbol{T}$ is defined as $\boldsymbol{T_s/2}$ [28]. In the simulations of the thesis, for the control of the PMSG, a inverter with a switching time delay equal to 0,0005 s has been used. But it must be said also that, as it has been made in [11] [27], the time delay of the inverter could be neglected, due

to the slow variation of the waves, and set to be equal zero (without compromise the control of the electrical machine and therefore also the results). At this point the block of current control loop can be introduced, it is shown in the next figure. As it can be seen the loop is equal for both the d-q axes.

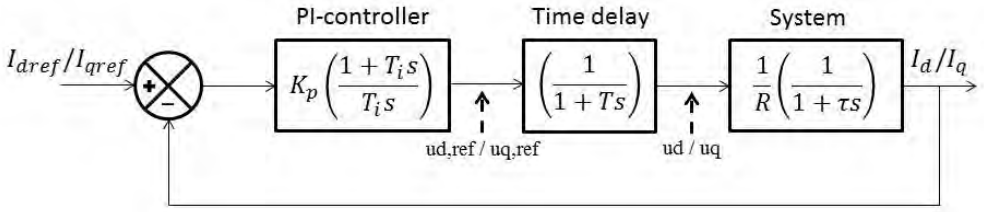

Figure 47 – Block diagram of current control loop

Hence as in [28], the open loop transfer function can be defined and it is equal to:

$$\boldsymbol{G_{OL} = k_p\left(\frac{1+T_i s}{T_i s}\right)\frac{1}{1+Ts}\ \frac{1}{1+\tau s}\ \frac{1}{R}} \quad \textbf{(28)}$$

The tuning of the current controller has been made using the **modulus optimum** technique. That can be applied to low order transfer function (minor of 3) and involves a crossover frequency as high as possible. The first step of this technique is the cancellation of the dominant pole $\boldsymbol{(1+\tau s)}$ [28], setting $\boldsymbol{T_i = \tau}$. Therefore the open loop transfer function can be written as in equation (29).

$$\boldsymbol{G_{OL} = \frac{k_p}{\tau R}\ \frac{1}{s(1+Ts)}} \quad \textbf{(29)}$$

Hence, the closed loop transfer function can be obtained:

$$\boldsymbol{G_{CL}(s) = \frac{G_{OL}(s)}{G_{OL}(s)+1} = \frac{k_p}{k_p+\tau R\, s(1+Ts)}} \quad \textbf{(30)}$$

After several simplifications the following equation is obtained [28]:

$$\boldsymbol{G_{CL}(s) = \frac{1}{1+\frac{\tau R}{k_p}s+\frac{\tau R T}{k_p}s^2}} \quad \textbf{(31)}$$

The standard second order transfer function is equal to [28]:

$$\boldsymbol{h(s) = \frac{\frac{1}{k}}{1+2\,\xi\frac{s}{\omega_0}+\left(\frac{s}{\omega_0}\right)^2}} \quad \textbf{(32)}$$

$\boldsymbol{\omega_0}$ is the undamped resonance frequency and $\boldsymbol{\xi}$ is the relative damping coefficient. Equating equation (31) with (32) and after several simplification, $\boldsymbol{\omega_0}$ and $\boldsymbol{\xi}$ are obtained and are shown in the next page in equation (33) and (34) respectively.

$$\omega_0 = \sqrt{\frac{k_p}{\tau R T}} \quad (33)$$

$$\xi = \frac{1}{2}\sqrt{\frac{\tau R}{k_p T}} \quad (34)$$

The modulus optimum imposes $G_{CL}(s)$ to be equal to 1 between zero frequency and a frequency as high as possible in the frequency spectrum. If $G_{CL}(s) \approx 1$, the **id/iq** follows **id,ref/iq,ref** and the controller circuit works as wanted. Therefore:

$$|G_{CL}(s)| = 1 \quad (35)$$

Substituting $s=j\omega$, it is obtained:

$$|G_{CL}(s)| = 1 = \frac{k_p}{\sqrt{\left(k_p - \tau R T \omega^2\right)^2 + (\tau R \omega)^2}} \quad (36)$$

After several simplifications and rearranging, the proportional gain is expressed as:

$$k_p = \frac{\tau R (T^2 \omega^2 + 1)}{2T} \quad (37)$$

For $\omega \ll \frac{1}{T} = 4000\ rad/s$, $(T\omega)^2$ can be neglected and k_p is equal to [28]:

$$k_p = \frac{\tau R}{2T} \quad (38)$$

k_i can be obtained from T_i, it is shown in equation (39).

$$k_i = \frac{R K_p}{L} \quad (39)$$

4.3.3 Torque control and field-weakening

When the rotor velocity is less than the nominal speed of the PMSG (n_n= 900 rpm) the reference direct current $i_{d,ref}$ is always equal to 0 and the reference quadrature current $i_{q,ref}$ is directly proportional to the torque reference (T_{ref} = ***Torqueref***) as it is shown by equation (40).

$$i_{q,ref} = \frac{2T_{ref}}{3p\,\Psi_{pm}} \quad (40)$$

Therefore if the rated speed of the generator is not overcome there is not the necessity of a field-weakening control. But, as it has been said previously, the addition of power limit involves the utilization of a PMSG with a wide constant power region (with a high overspeed ratio, the mechanical characteristic of the electrical machine is plotted in figure 44). The generator will work most of the time, during the 900 s of simulation, with $n \geq n_n$ in the constant power range and as

consequence a field-weakening control is needed. When $n \geq n_n$ the field-weakening control must be activated and the current of the d-axis becomes negative. In figure 48 the quadrature and direct currents as a function of the rotor velocity, which imply the maximum available torque for each velocity of the generator, are plotted.

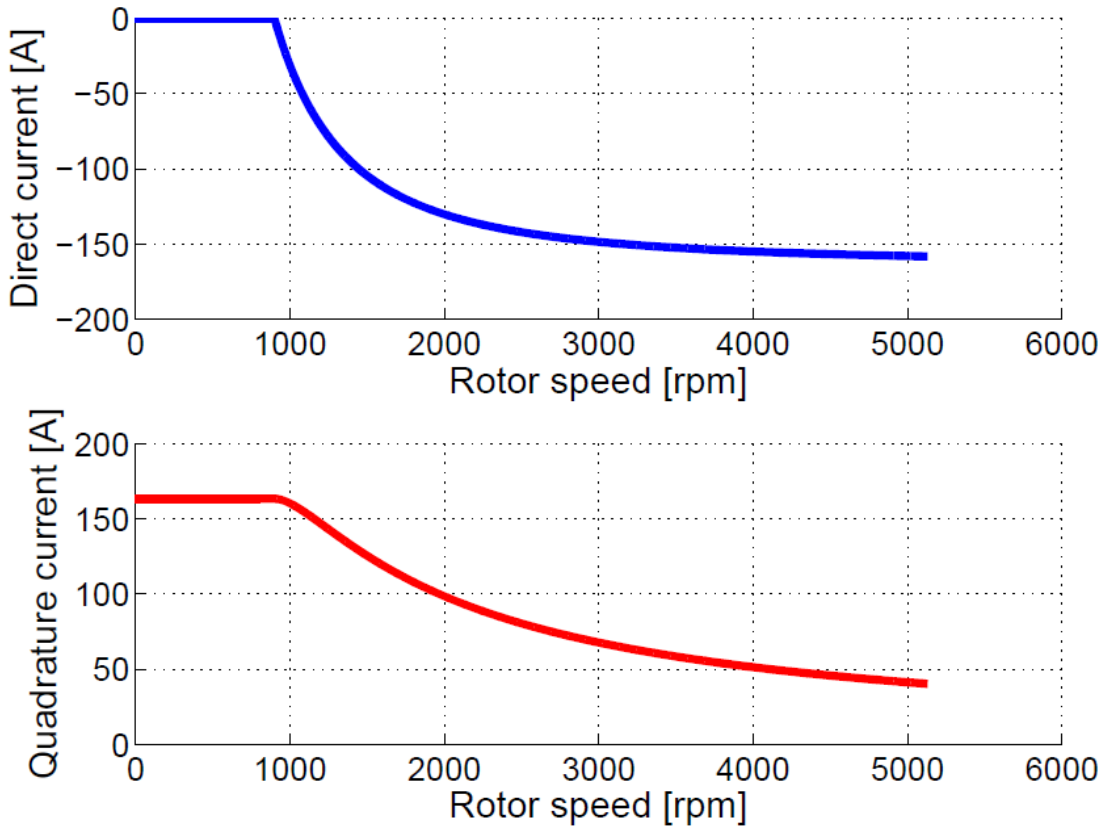

Figure 48 – Quadrature and direct current as a function of the generator speed

$i_{d,ref}$ and the $i_{q,ref}$ must be recalculated by a field-weakening block that has been implemented in MALAB-Simulink. The field-weakening control is implemented as in [26] with some changes due to the particularity of the generator and the control strategy of the point absorber (passive loading control). The equations in this paragraph illustrate the field-weakening control strategy adopted in this thesis. From the equation (19) and (20) the next stedy-state equations are obtained [26]:

$$v_d = R\, i_d - L\, \omega_e i_q \tag{41}$$

$$v_q = R\, i_q + L\, \omega_e i_d + \omega_e \Psi_{pm} \tag{42}$$

The specific limits of current and voltage of the electrical machine and of the inverter have to be respected with the aim to avoid to compromise their life time and their performances, this has been made using equation (43) and (44) from [26].

$$i_d{}^2 + i_q{}^2 \leq I_{lim}{}^2 \quad (43)$$

$$v_d{}^2 + v_q{}^2 \leq V_{lim}{}^2 \quad (44)$$

The limit of current (I_{lim}) is represent by the peak value of the rated phase current of the electrical machine (Ip = 170 A), which is equal for the inverter. The limit of voltage (V_{lim}) is the maximum phase voltage in magnitude that the inverter can supply as output ($Vdc/2$ = 400 V), which respects the limit of phase voltage of the electrical machine. The equations (41) and (42) can be inserted in (44) obtaining equation (45), that represents the voltage constraint in terms of the stator currents [26].

$$\left(i_d + \frac{\omega_e^2 L \Psi_{pm}}{R^2+\omega_e^2 L^2}\right)^2 + \left(i_q + \frac{\omega_e R \Psi_{pm}}{R^2+\omega_e^2 L^2}\right)^2 \leq \frac{V_{lim}^2}{R^2+\omega_e^2 L^2} \quad (45)$$

Neglecting the stator resistance is obtained the following equation:

$$\left(i_d + \frac{\Psi_{pm}}{L}\right)^2 + \left(i_q\right)^2 \leq \frac{V_{lim}^2}{\omega_e^2 L^2} \quad (46)$$

Equation (46) is useful to understand the behaviour of the field-weakening control and with equation (43) allows to define the operating limits of the PMSG that are shown in figure 49 with the d-q currents as axes.

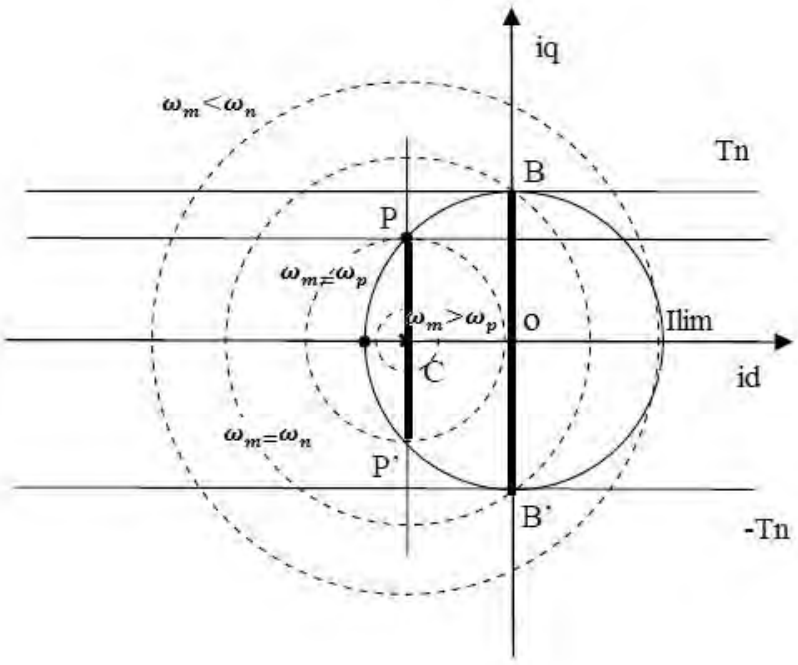

Figure 49 - Operating limits of the electrical machine; ω_n nominal angular velocity of the PMSG.

The limit of current, defined by equation (43), involves a torque limit and is represented by a circular area of radius $\boldsymbol{I_{lim}}$ delimited by a continuous line (with **o** as centre of the circle). The limit of voltage, defined by equation (46), is represented in figure 49 by several concentric circles that have as radius the inverse of the electromechanical speed ($\boldsymbol{\omega_e}$). The circles of the limit of voltage are represented by a dashed line and they imply limits of velocity. As it is shown in figure 49 the centre C of the circles of the limit of voltage is inside the circular area of the limit of current and its coordinates are $(-\frac{\Psi_{pm}}{L}, 0)$. When the generator works at a given speed of work respecting the limit of current and voltage, the functioning of the PMSG corresponds to a point of work inside of the circle of the limit of current and of the limit of voltage corresponding at that point of work. When the generator works at $\boldsymbol{\omega_m < \omega_n = \frac{2\,\pi\, n_n}{60} = 95,24\ rad/s}$ the field-weakening control is not activated and the electrical machine works on the segment BB', the point of work depends on the $\boldsymbol{i_{q,ref}}$ needed to produce $\boldsymbol{T_{ref}}$ as it is shown by equation (40). It is more convenient to work on the segment BB' because it represents the points of work for which there is the maximum ratio between the torque and the current, therefore when $\boldsymbol{\omega_m < \omega_n}$ the d-axis current is equal to 0. When $\boldsymbol{\omega_m \geq \omega_n}$ the field-weakening is activated, the direct current starts to be negative and the point of work of the generator is inside the area BB'P'P. When it is reached $\boldsymbol{\omega_p}$, which is the velocity that involves the $\boldsymbol{i_{d,ref} = -\frac{\Psi_{pm}}{L} = -163,43\ A}$, the points of work are on the segment PP'. In Figure 51 the flowchart of the filed-weakening control is shown. It allows to obtain the d-q reference currents of the current control loop and then to control the torque of the generator in each instant of the simulation. $\boldsymbol{i_{q,ref}}$, $\boldsymbol{\omega_m}$ and $\boldsymbol{i_{d,ref} = 0}$ are the input of the field-weakening block in Simulink and $\boldsymbol{i_{d,refnew}}$, $\boldsymbol{i_{q,refnew}}$ are the outputs. For explain the field-weakening operation regions of the electrical machine, the stator resistance has been neglected and equation (46) has been used. Instead, as in [26] in the field-weakening block in Simulink, the stator resistance has not been neglected and equation (45) is used. The limit of voltage is still defined by several concentric circles, but the centre of the circles is not anymore fixed and the radius is not inversely proportional of the electromechanical speed. $\boldsymbol{i_{d,FW}}$, $\boldsymbol{i_{q,FW}}$ are coordinates of the intersecting point between the circle of the limit of current (equation (43)) and the circle of the limit of voltage (equation (45)). They are calculated inside the field-weakening block in Simulink and will be defined in the next equations of this paragraph.

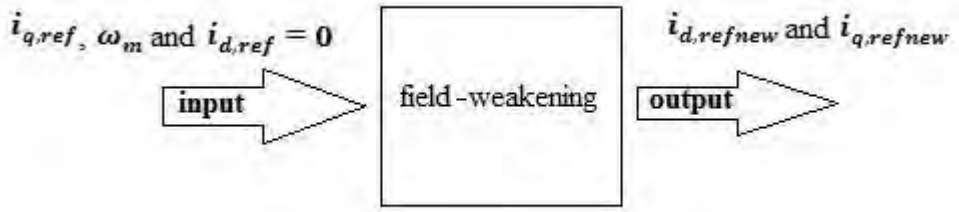

Figure 50 – Field-weakening block in MATLAB-Simulink

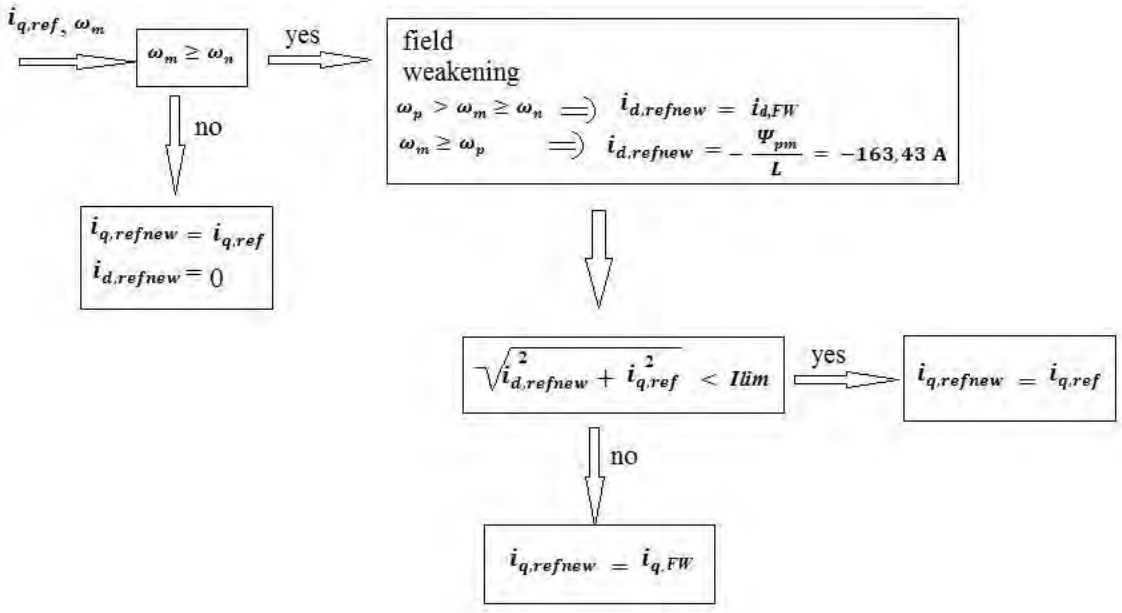

Figure 51 – Flowchart of field-weakening control, it involves the torque control

The power limit chosen (100kW), during the field-weakening operation region in the simulations, involves always a $i_{q,ref}$ which corresponds to a point of work in figure 49 outside the area BB'P'P. It means that the limit of current would not be respected, if the quadrature current of the electrical machine is equal to $i_{q,ref}$. For this reason $i_{q,refnew}$ is different from $i_{q,ref}$ and is equal to $i_{q,FW}$, which corresponds to the maximum available torque in the field-weakening operation region respecting the limit of current. In other words in the simulations that have been run the point of work in figure 49 is always on the borderline of the area BB'P'P and not inside. Therefore, in the field-weakening operation, the reference torque (***Torqueref***) is not equal to the torque generated by the PMSG but it is slightly minor in module with the goal to respect the limit of current of the electrical machine.

From equation (47) the procedure to obtain $i_{d,FW}$, $i_{q,FW}$ starts. The voltage constraint as a function of the velocity and of the d-axis current is obtained combining equation (43) with equation (45) as in [26]:

$$\left(i_d + \frac{\omega_e^2 L \Psi_{pm}}{R^2+\omega_e^2 L^2}\right)^2 + \left(\pm\sqrt{I_{lim}^2 - i_d^2} + \frac{\omega_e R \Psi_{pm}}{R^2+\omega_e^2 L^2}\right)^2 \leq \frac{V_{lim}^2}{R^2+\omega_e^2 L^2} \quad (47)$$

From equation (47) it is possible to calculate the d-axis current as it is illustrated in [26]:

$$i_{d1,2} = \frac{-b \pm \sqrt{b^2-4ac}}{2a} \quad (48)$$

As in [26] a,b,c are defined by the following expressions:

$$a = 4\left(i_{d,cen}^2 + i_{q,cen}^2\right) \quad (49)$$

$$b = 4 i_{d,cen}\left(\frac{V_{lim}^2}{R^2+\omega_e^2 L^2} - \left(I_{lim}^2 + i_{d,cen}^2 + i_{q,cen}^2\right)\right) \quad (50)$$

$$c = \left(\left(I_{lim}^2 + i_{d,cen}^2 + i_{q,cen}^2\right) - \left(\frac{V_{lim}^2}{R^2+\omega_e^2 L^2}\right)\right)^2 - 4 i_{q,cen}^2 I_{lim}^2 \quad (51)$$

$i_{d,cen}$ and $i_{q,cen}$ are the coordinates of the centre of the voltage constraint circle that is represented by equation (45) (wherein the stator resistance of the generator is not neglected). The coordinates are obtained from [26] and they are shown in equation (52) and (53). It can be noticed that also the rotor velocity is present in the expressions.

$$i_{d,cen} = -\frac{\omega_e^2 L \Psi_{pm}}{R^2+\omega_e^2 L^2} \quad (52)$$

$$i_{q,cen} = -\frac{\omega_e R \Psi_{pm}}{R^2+\omega_e^2 L^2} \quad (53)$$

In $b^2 - 4ac$ is always positive considering the operation area of the field-weakening control, therefore i_d depends only on the sign of the electromechanical speed as it is explained by equation (54) and (55) [26]:

$$if \quad \omega_e > 0 \quad i_{d,FW} = i_d = \frac{-b+\sqrt{b^2-4ac}}{2a} \quad (54)$$

$$if \quad \omega_e \leq 0 \quad i_{d,FW} = i_d = \frac{-b-\sqrt{b^2-4ac}}{2a} \quad (55)$$

Now it is possible to calculate the intersecting points between the circle of the limit of current (equation (43)) and the circle of the limit of voltage (equation (45)). The intersecting points have a quadrature current equal to $i_{q,FW}$ (defined by equation

(56)), which corresponds to the maximum available torque in the field-weakening operation region. As in [26] the quadrature current is equal to:

$$i_{q,FW} = i_q = \sqrt{I_{lim}^2 - i_d^2} \quad (56)$$

4.4 Simulations and results obtained

The simulations have been run in MATLAB-Simulink, with the Hydrodynamic WEC model of the simulations of the previous chapters and the Simulink model illustrated in figure 46 (which allows to control the PMSG). A general overview of the WEC model simulated is shown in figure 37. The control strategy implemented is the passive loading control with two constraints: the power limit (100 kW) and the torque limit (the module of the torque is limited to 850 Nm). The data of the PMSG, that have been used, are shown in table 8. The low, medium and high energy sea state (for 900 s) have been tested, each of them with the B_L coefficient which involves the highest average mechanical power. The damping coefficients are shown in the next table and are the same of table 7.

Table 9 - Damping coefficients used in the simulations

B_L coefficient [kg/s]	Energy sea state
400000	low
4300000	medium
3100000	high

An ideal three phase inverter (with ideal switches) has been used to control the generator with the switching frequency (f_s) equal to 2000 Hz. In this paragraph the efficiency of the electrical machine is calculated taking into account: the copper losses, the iron losses and the mechanical losses. The Simulink models used to calculate the losses of the generator are illustrated in appendix B. Subsequently the equations, that have been used, are shown and explained. From [29] equation (57) is obtained, it allows to calculate the electrical power (in real time) produced by the generator taking into account only the copper losses (P'_{el}).

$$P'_{el} = \frac{3}{2}\left(v_d i_d + v_q i_q\right) \quad [W] \quad (57)$$

The iron and mechanical losses are not included in the previous equation and have to be calculated separately. As there is written in [30] [31] the iron losses are usually calculated considering the flux density (B) sinusoidal in the core material (B is not perfectly sinusoidal, therefore it has been done an approximation that should not significantly affect the results). p_{iron} is the total iron-loss density (in real time) considering that the flux density varies sinusoidally with the angular velocity of the generator ω_m [30]:

$$p_{iron} = p_h + p_e = k_h B^{\beta} \omega_m + k_e B^2 \omega_m^2 \quad \left[\frac{W}{m^3}\right] \tag{58}$$

The total iron-loss density is composed by the hysteresis loss density (p_h) and by the eddy-current loss density (p_e). The following coefficients depend on the lamination material: β, k_h and k_e. They are respectively the Steinmetz, the hysteresis and eddy current constants. Typical values using silicon iron laminations, with ω_m given in rad/s, are in the following ranges [30]: k_h= 40-55, β = 1.8-2.2 and k_e= 0.04-0.07. Finally the total iron-loss (P_{iron}) is obtained multiplying the volume of the iron machine for the total iron-loss density. The mechanical losses (P_{add}) (in real time) are calculated as in [32]:

$$P_{add} = c\, A_n \sqrt{n} = c\, \frac{P_n}{cos\varphi} \sqrt{n} \qquad [W] \tag{59}$$

The losses are directly proportional to the nominal apparent power (A_n) and to the root of the velocity of the generator expressed in revolutions per minute (n). c is the mechanical constant and it has to be in the range 0.4-0.6 [32], $cos\varphi$ is the load factor. As it can be seen in equation (59), differently of the iron losses, the mechanical losses are obtained directly from the equation and they are represented in W. In table 10 the parameters used in the model to calculate the generator losses are shown.

Table 10 – Parameters of the PMSG losses.

Quantity	Value
Mechanical constant, c	0.5
Nominal power, P_n	80 kW
Load factor, $cos\varphi$	0.96
Magnetic flux density, B	0.8 T
Iron volume, $Volume$	0.05 m^3
Steinmetz constant, β	2
Hysteresis constant, k_h	48
Eddy current constant, k_e	0.055

At this point the electrical power P_{el} (in real time) produced by the PMSG can be calculated subtrahend to the P'_{el} the iron and mechanical losses:

$$P_{el} = P'_{el} - P_{iron} - P_{add} \qquad [W] \tag{60}$$

Hence the total losses P_{loss} (in real time) of the PMSG can be calculated and they are equal to:

$$P_{loss} = P_{mecc} - P_{el} \qquad [W] \tag{61}$$

The total losses of the generator are equal to the total losses of the transformation from the mechanical power to the electrical power, because the inverter used in the Simulink-model is ideal. As it has been said at the beginning of this paragraph the three representative energy sea states have been tested, each of them for 900 s. During this time the average value of the electrical power ($P_{el\text{-}average}$), of the mechanical power ($P_{mecc\text{-}average}$) and of the total losses ($P_{loss\text{-}average}$) has been measured. Finally the average efficiency ($\eta_{average}$) in 900 s of simulation can be calculated for each energy sea state using the following equation:

$$\eta = \frac{P_{el-average}}{P_{mecc-average}} \tag{62}$$

The results of the simulations are shown in the next table.

Table 11 – Results of the simulations

Energy sea state	Quantity	Value
low	Average mechanical power, $P_{mecc\text{-}average}$	17383 W
	Average electrical power, $P_{el\text{-}average}$	15310 W
	Average total losses, $P_{loss\text{-}average}$	2073 W
	Average efficiency, η	0.881
medium	Average mechanical power, $P_{mecc\text{-}average}$	64010 W
	Average electrical power, $P_{el\text{-}average}$	57861 W
	Average total losses, $P_{loss\text{-}average}$	6149 W
	Average efficiency, η	0.904
high	Average mechanical power, $P_{mecc\text{-}average}$	72291 W
	Average electrical power, $P_{el\text{-}average}$	65613 W
	Average total losses, $P_{loss\text{-}average}$	6678 W
	Average efficiency, η	0.908

It can be noticed some differences compared the results of table 7 (where in the simulations the electrical machine was considered ideal capable to follow the reference torque perfectly in each instant of the simulation). The average mechanical power obtained is more or less the same in the low energy sea state (about 17 kW) instead, in the high and medium energy sea state, is decreased about of the 3 % . This is due to the fact that, as it has been explained in previous paragraph, the PMSG in the field-weakening operation region doesn't follow perfectly the torque reference. With the aim to respect the circle of the limit of current (equation (43)), when $\omega_m \geq \omega_n$ during the 900 s of simulation, the module of the torque of the generator is equal to the maximum available torque in the field-weakening operation region which is lower than the torque reference (T_{ref}). The reduction of the average mechanical power is considerable (3 %) in the medium and high energy case, and almost null in the low energy case because the generator works very few times in the

field-weakening region in the low energy sea state. An increment of the energy content in the sea state implies an increase of the average efficiency ($\boldsymbol{\eta}$) of the PMSG. $\boldsymbol{\eta}$ is equal to 0.881 in the low energy sea state and achieves the value 0.904 and 0.908 respectively in the medium and high energy sea state. This can be justified observing figure 52, wherein the efficiency map of a common PMSM (permanent magnet synchronous motor) with SMPMs (surface mounted permanent magnets) and a wide field-weakening region is illustrated.

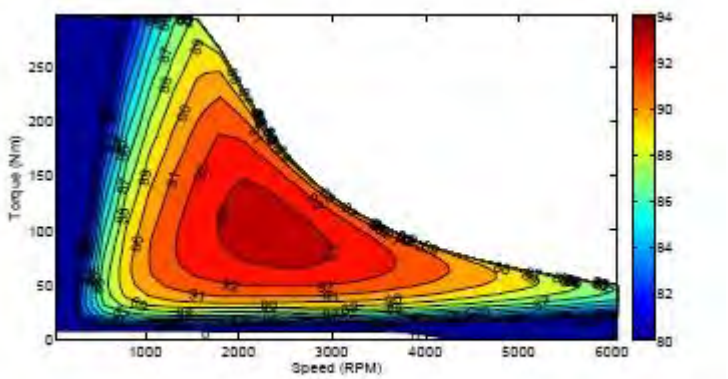

Figure 52 – [33] Example of a PMSM efficiency map with SMPMs and a quite high overspeed ratio

Obviously the values of efficiency, torque and speed in figure 52 should be ignored because they are referred to a different electrical machine compared that one used in the simulations. But the way that varies the efficiency in the plane $\boldsymbol{T}$- $\boldsymbol{n}$ (torque- rotor velocity) is similar for each PMSM with SMPM and a wide field-weakening region. It is known that the generator in the medium and high energy sea state works most of the time in the field-weakening operation region on the line of the maximum available torque. As it can be seen in figure 52 on that line the efficiency is not the maximum achievable, but is quite high. Instead in the low energy sea state the generator works very few time in the field-weakening operation region and almost always in the region where the rotor velocity is lower than the nominal. In this area the efficiency is lower especially if the rotor velocity is very low or the torque is quite high. This involves a lower average efficiency for the low energy case.

4.5 Final considerations

The case study simulated (shown in figure 37) is convenient to be applied if, in the scatter diagram of the location, the medium energy sea states and the high energy sea states prevail over the low energy ones. This is justified by the peak to average power ratios of table 7. The average efficiency, obtained using the damping coefficients of table 9 for each energy sea state, is higher in the medium and high energy sea state compared the low one. This is another advantage in favour of a location with many high and medium energy sea states. The conversion from the mechanical to the electrical power has been made successfully up to the DC side of the inverter that control the PMSG. The next step of this thesis regards the modelling of the grid connection. It allows to connect the wave-to-wire model to the electric grid and then it allows to produce electric energy by the sea waves to the electric grid.

5. CONNECTION TO THE GRID OF THE WAVE-TO-WIRE MODEL

5.1 Introduction

In this chapter an inverter, that has the task to connect the integrated wave-to-wire model to the grid, is added. In figure 53 the integrated wave-to-wire model with the grid connection is represented (AFE stands for active front end). For understanding better the behaviour of the system, the simplified model of the point absorber wave energy converter is shown in figure 54. $\boldsymbol{i}$, $\boldsymbol{u_g}$, $\boldsymbol{i_g}$ represent respectively the current of the PMSG, the grid voltage and the grid current.

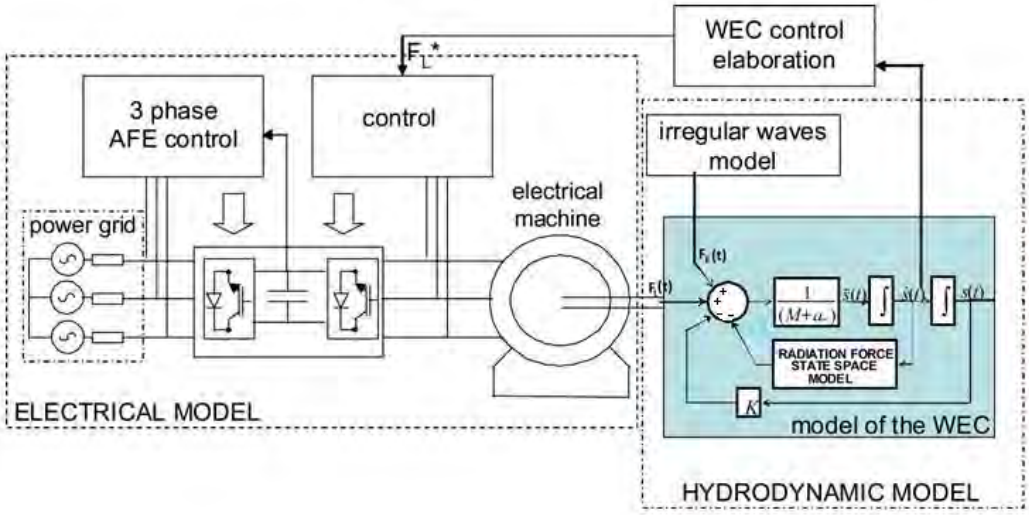

Figure 53 – Integrated wave-to-wire model with the grid connection, including hydrodynamic and electric model of the WEC [34]

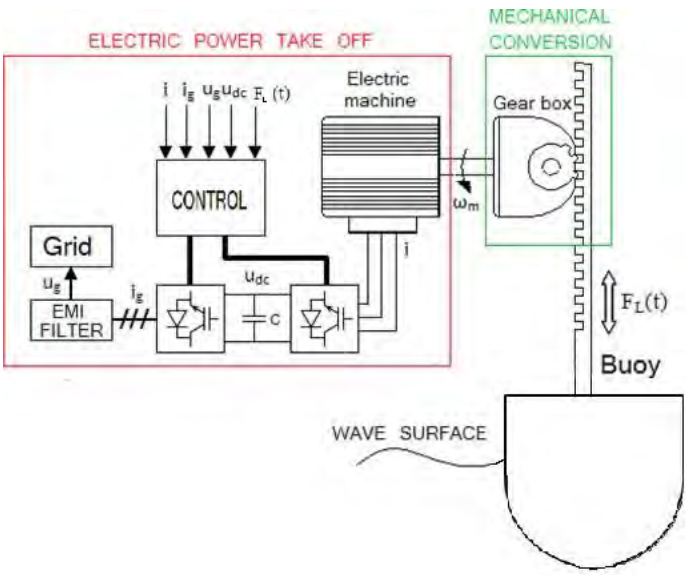

Figure 54 – Simplified model of the point absorber wave energy converter [34]

In the next paragraphs of this chapter it will be explained, as it has been made in detail, the connection to the grid of the wave-to-wire model and the control of the grid side converter.

5.2 Equations of the system and assumptions

Before to explain the control of the grid side converter, it is mandatory to introduce several equations and assumptions that will be used in the voltage oriented vector control explained in the next paragraph. The AC side of the inverter consists of three phases and the equivalent per phase grid side model is represented in the figure below.

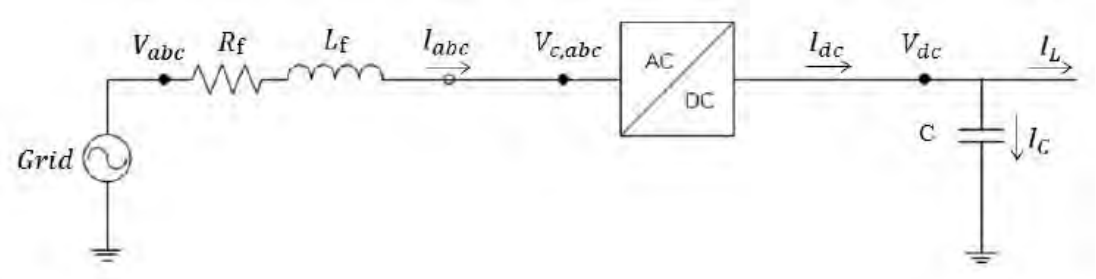

Figure 55 – Equivalent per phase grid side model [28]

$\boldsymbol{R_f}$, $\boldsymbol{L_f}$ and $\boldsymbol{C}$ represent respectively the filter resistance, the filter inductance and the capacity of the capacitor. $\boldsymbol{R_f}$ and $\boldsymbol{L_f}$ compose the grid side filter that has the goal to reduce the injection of harmonic currents into the electric grid. The resistance and inductance of the eventual transmission line are not taken into account in this thesis. A lossless converter and a balanced three-phase circuit are considered. The equations of the first part of this paragraph are referred to the **dynamics of the grid side.** The voltage change between $\boldsymbol{V_{abc}}$ and $\boldsymbol{V_{c,abc}}$ are equal to [28]:

$$\boldsymbol{V_{abc} - V_{c,abc} = R_f I_{abc} + L_f \frac{dI_{abc}}{dt}} \quad \textbf{(63)}$$

In the voltage oriented vector control the PI-controllers are needed with the own reference values in the *dq*-frame. Therefore, the voltage invariant transformation of appendix A is applied and equation (63) is transformed to the *dq*-frame [28]:

$$\boldsymbol{V_d - V_{c,d} = L_f \frac{dI_d}{dt} + R_f I_d - \omega L_f I_q} \quad \textbf{(64)}$$

$$\boldsymbol{V_q - V_{c,q} = L_f \frac{dI_q}{dt} + R_f I_q + \omega L_f I_d} \quad \textbf{(65)}$$

Equation (64) and (65) are both dependent on $\boldsymbol{I_d}$ and $\boldsymbol{I_q}$. With the goal to decouple the *dq*-axes, the following fictive voltages are defined:

$$\boldsymbol{V'_d = -V_{c,d} + V_{ff,d} = -V_{c,d} + \omega L_f I_q + V_d} \quad \textbf{(66)}$$

$$V'_q = -V_{c,q} + V_{ff,q} = -V_{c,q} - \omega L_f I_d + V_q \quad (67)$$

$V_{ff,d}$ and $V_{ff,q}$ are defined as feed forward terms. A voltage invariant transformation has been done and as result $V_q = 0$. Inserting equation (66) into (64) and (67) into (65) the following equations are obtained [28]:

$$V'_d = L_f \frac{dI_d}{dt} + R_f I_d \quad (68)$$

$$V'_q = L_f \frac{dI_q}{dt} + R_f I_q \quad (69)$$

Therefore the feed forward terms allow to decouple the d-q axes and then to obtain two independent equations. From now the **power balance** between the DC and the AC side is investigated. As in [28] the three phase apparent power (S) at the AC-side is defined:

$$S = \frac{3}{2} V_{dq} I^*_{dq} \quad (70)$$

$$S = \frac{3}{2} (V_d + jV_q)(I_d - jI_q) \quad (71)$$

$$S = \frac{3}{2} [(V_d I_d + V_q I_q) + j(-V_d I_q + V_q I_d)] \quad (72)$$

The losses in the conversion from the DC to the AC side are neglected and then it is possible to write [28]:

$$\mathrm{Re}(S) = P_{AC} = \frac{3}{2} (V_d I_d + V_q I_q) = P_{dc} = V_{dc} I_{dc} \quad (73)$$

P_{AC} is the active power produced by the converter and P_{dc} is the power on the DC side. $Vq = 0$ because of the voltage invariant transformation and then it is obtained [28]:

$$P_{AC} = \frac{3}{2} V_d I_d = V_{dc} I_{dc} \quad (74)$$

and:

$$I_{dc} = \frac{3}{2} \frac{V_d}{V_{dc}} I_d \quad (75)$$

From (72) the reactive power produced by the inverter is determined [28]:

$$Q = \mathrm{Im}(S) = \frac{3}{2}(-V_d I_q + V_q I_d) \quad (76)$$

simplifying:

$$Q = -\frac{3}{2} V_d I_q \quad (77)$$

From equation (77) and (74) it can be noticed that the active and reactive power produced by the inverter can be controlled independently: the active power is calculated by $\boldsymbol{V_d}$ and $\boldsymbol{I_d}$, instead the reactive power is determined by $\boldsymbol{V_d}$ and $\boldsymbol{I_q}$. It is enough to control only the *dq*-currents because the direct voltage ($\boldsymbol{V_d}$) is considered stiff. The specifications of [35] impose null reactive power at the point of common coupling for normal conditions of work. This is obtained fixing $\boldsymbol{I_q}$=0. The last part of this paragraph regards the **DC-link**: the current balance on the DC side is equal to [28]:

$$\boldsymbol{C\ \frac{dV_{dc}}{dt} = I_C = I_{dc} - I_L} \tag{78}$$

If it is inserted equation (75):

$$\boldsymbol{C\ \frac{dV_{dc}}{dt} = \frac{3}{2}\ \frac{V_d}{V_{dc}}\ I_d - I_L} \tag{79}$$

5.3 Voltage oriented vector control

The control strategy used in this thesis involves an inner current controller connected in cascaded to an outer voltage controller. The keys of the control strategy are the following: the DC-link voltage is controlled exploiting its relation with the d-axis current and the reactive power is controlled using its relation with the q-axis current. Therefore the reference input of the d-axis of the inner current controller is equal to the output signal of the outer voltage controller. Instead the reference input of the q-axis of the inner current controller is the q-axis current ($\boldsymbol{I_q}$**= 0** in this thesis) which is linked with the reactive power produced by the converter. The proposed control strategy is shown in figure 56. The PLL (Phase Lock Loop) is a block which senses the phase ($\boldsymbol{\theta}$) of the input signal. As there is written in appendix A, the phase angle $\boldsymbol{\theta}$ is required for the dq-transformation. In the paragraph 5.3.1 and 5.3.2 will be explained respectively the inner current controller and the outer voltage controller.

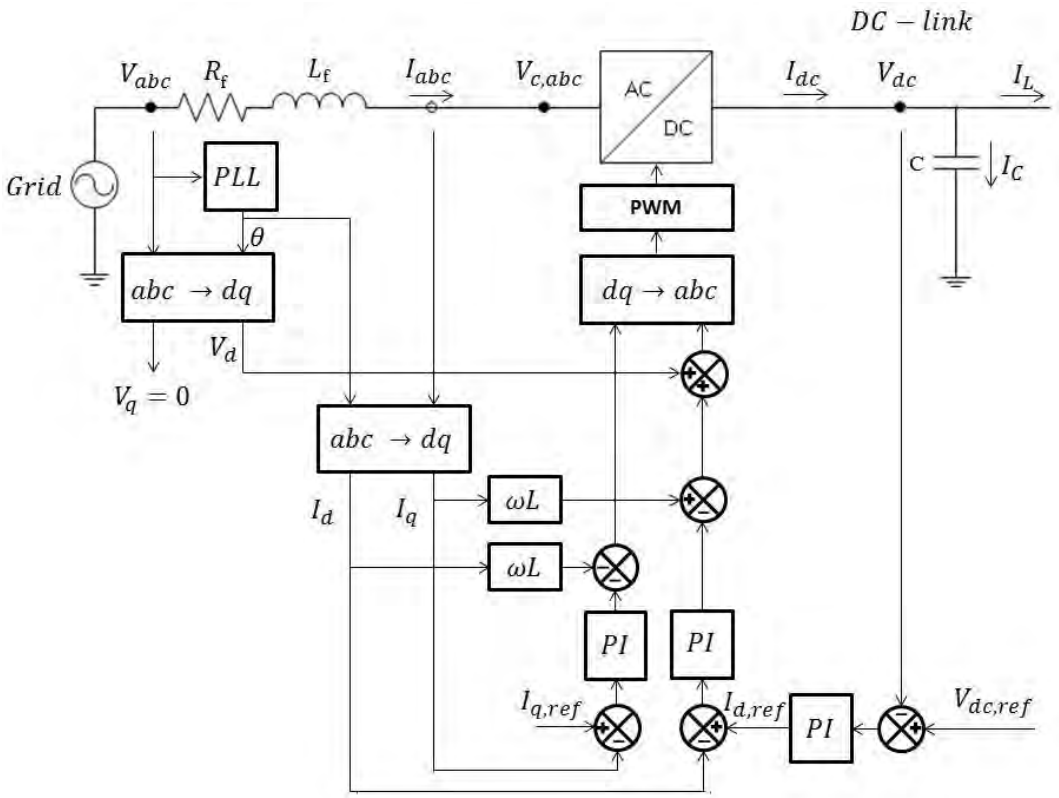

Figure 56 – Overview of the control system [28]

5.3.1 Inner current controller

Before showing the complete block diagram of the inner current controller some transfer functions have to be defined. The decoupling of the *dq*-axes introduced in the paragraph 5.2 allows to see an RL circuit. Equation (68) and (69) are equal, but one regards the d-axis and the other the q-axis. Hence a general transfer function will be defined for both the axes. Using the Laplace transformation equation (68) becomes [28]:

$$\boldsymbol{V'(s) = L_f I(s) s + R_f I(s) = I(s)(L_f s + R_f)} \quad \textbf{(80)}$$

We get:

$$\frac{\boldsymbol{I(s)}}{\boldsymbol{V'(s)}} = \frac{1}{\boldsymbol{(L_f s + R_f)}} \quad \textbf{(81)}$$

Equation (82) defines the system transfer function [28]:

$$\frac{\boldsymbol{I(s)}}{\boldsymbol{V'(s)}} = \frac{1}{\boldsymbol{R_f(\tau_f s + 1)}} \quad \textbf{(82)}$$

$\boldsymbol{\tau_f}$ is defined as the ratio between the filter inductance and the filter resistance ($\boldsymbol{\tau_f = L_f/R_f}$).

The inverter controlled by the PWM involves a time delay which is taken into account by the following transfer function [28]:

$$\boldsymbol{J = \frac{1}{1+Ts}} \tag{83}$$

$\boldsymbol{T_s}$ is the switching time delay of the inverter in seconds and $\boldsymbol{T}$ is defined as $\boldsymbol{T_s/2}$ [28]. As in the current control loop of the PMSG also here the PI controllers are needed. As in [28] a regulator is defined by the following transfer function:

$$\boldsymbol{PI = k_p + \frac{k_i}{s} = \frac{k_p\, s + k_i}{s} = k_p \left(\frac{1+\frac{k_p}{k_i}s}{\frac{k_p}{k_i}s} \right) = k_p \left(\frac{1+T_i s}{T_i s} \right)} \tag{84}$$

$\boldsymbol{k_p}$ is the proportional gain and $\boldsymbol{k_i/s}$ is the integral term in parallel. $\boldsymbol{T_i}$ is defined as the time constant of the controller, it is equal to $\boldsymbol{k_p/k_i}$. The transfer functions defined by equation (82), (83) and (84) allow to introduce the block diagram of the current controller.

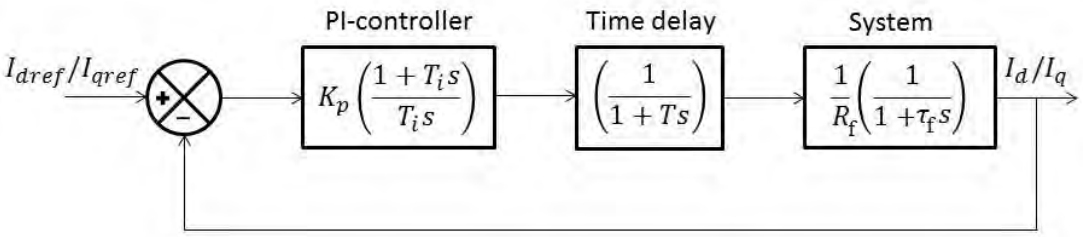

Figure 57 – Block diagram of the current controller [28]

From figure 57 the open loop transfer function obtained is equal to [28]:

$$\boldsymbol{h_{0,cc}(s) = k_p \frac{1+T_i s}{T_i s} \frac{1}{1+Ts} \frac{1}{R_f} \frac{1}{1+\tau_f s}} \tag{85}$$

Setting $\boldsymbol{T_i = \tau_f}$ the cancellation of the dominant pole $\boldsymbol{(1+\tau_f s)}$ is obtained and the following closed loop transfer function is found [28]:

$$\boldsymbol{M_{0,cc}(s) = \frac{h_{0,cc}(s)}{h_{0,cc}(s)+1} = \frac{k_p}{T\,\tau_f R_f s^2 + \tau_f R_f s + k_p}} \tag{86}$$

The complete block diagram with d-axis, q-axis and the feed forward terms is shown in figure 58. The feed forward terms allow to decouple the *dq*-axes.

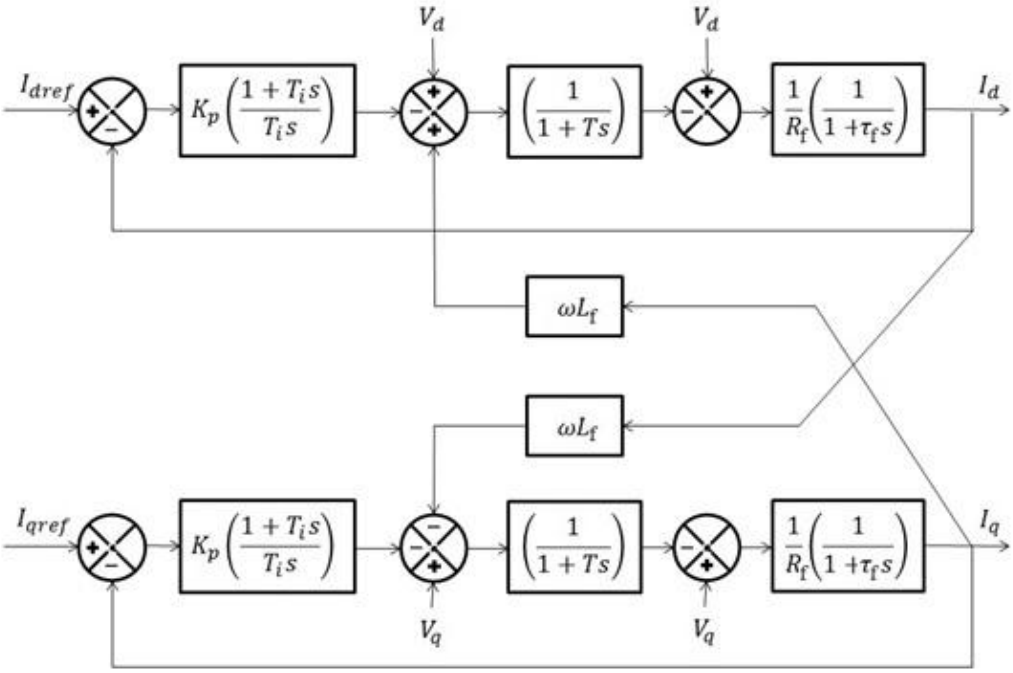

Figure 58 – Inner current controller with both the *dq*-axes

5.3.2 Outer Voltage controller

The DC-link voltage is regulated by the outer voltage controller to the wanted value ($\boldsymbol{V_{dc,ref}}$) with the goal to produce the $\boldsymbol{I_{dref}}$ (reference value of the direct-axis current). Equation (79) defines the current balance of the DC-link. It can be observed that is a non-linear equation and it must be linearised in order to find the stability condition of the DC side of the converter. The stationary conditions of the DC-link involve an almost constant voltage ($\boldsymbol{V_{dc}}$), therefore it is possible to linearize the system model near the operating point using the reference voltage ($\boldsymbol{V_{dc,ref}}$) [28]. As in [37] it has been made a linearization based on a Taylor series expansion:

$$\boldsymbol{C}\,\frac{\boldsymbol{dV_{dc}}}{\boldsymbol{dt}} = \frac{\boldsymbol{3}}{\boldsymbol{2}}\,\frac{\boldsymbol{V_{d,0}}}{\boldsymbol{V_{dc,ref}}}\,\boldsymbol{I_d} \tag{87}$$

Using the Laplace transformation it can be obtained [37]:

$$\boldsymbol{V_{dc}(s)} = \frac{\boldsymbol{3}}{\boldsymbol{2}}\,\frac{\boldsymbol{V_{d,0}}}{\boldsymbol{V_{dc,ref}}}\,\frac{\boldsymbol{1}}{\boldsymbol{sC}}\boldsymbol{I_d}(s) \tag{88}$$

The DC-link voltage ($\boldsymbol{V_{dc}}$) can be controlled controlling the d-axes current ($\boldsymbol{I_d}$), because $\frac{\boldsymbol{V_{d,0}}}{\boldsymbol{V_{dc,ref}}}$ is a constant quantity and hence the d-axes current is directly proportional to the DC-link voltage through equation (88). For this reason the

reference value of the *d*-axes current (input of the current controller) is calculated by the outer voltage controller. A cascaded control system is obtained and therefore it is important that the inner current controller works faster than the outer voltage controller. Analyzing equation (86) it can be observed which the transfer function of the inner current controller is of the second order. The analysis of the operation of the voltage controller can be facilitated simplifying the closed loop transfer function of the current controller with a first order transfer function. The simplification of the transfer function has been done as in [28] so that the time integral of the controller's error signal is the same for the original second order model and the first order model (the approximated one). The simplification of the closed loop current controller transfer function is the following [28]:

$$\frac{k_p}{T\,\tau_f R_f s^2+\tau_f R_f s+k_p} \cong \frac{1}{1+s\,T_{eq}} \tag{89}$$

Setting k_p as explained in paragraph 5.3.3 it is obtained [28]:

$$T_{eq} = 2\,T \tag{90}$$

A cascaded control system involves a slow response to disturbances that, in our control system, are represented by I_L. A feed forward term is introduced with the goal to reduce the disturbance of I_L on the system. Considering an ideal situation, with the introduction of the feed forward term, the perceived overall disturbance by the cascaded control system should be equal to zero. A stable condition involves a constant DC-link voltage and a current of the capacitor null ($I_c = 0$). Hence, under stable conditions, starting from equation (79) the feed forward term is obtained [28]:

$$I_d = \frac{2}{3}\frac{V_{dc}}{V_d} I_L \tag{91}$$

At this point the block diagram of the outer voltage controller can be introduced. It is shown in the next figure. T_{iv} is the time constant of the controller, k_{pv} is the proportional gain and k_{iv}/s is the integral term in parallel.

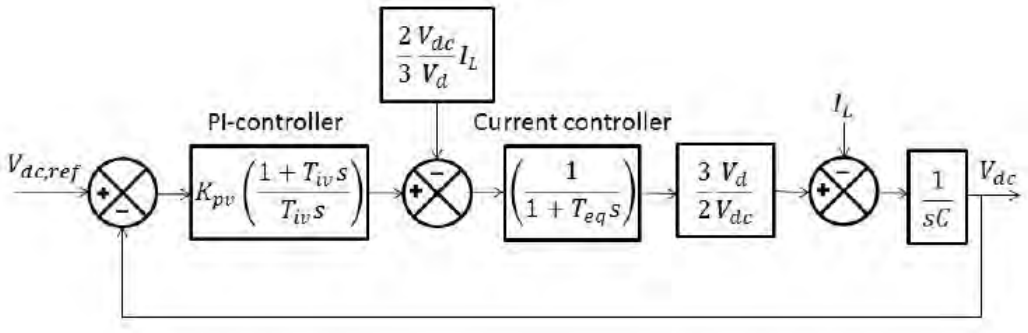

Figure 59 – Block diagram of the outer voltage controller [28]

From the block diagram the open loop transfer function of the outer voltage controller is obtained [28]:

$$\boldsymbol{h_{0,vc} = k_{pv}\left(\frac{1+T_{iv}s}{T_{iv}s}\right)\left(\frac{1}{1+T_{eq}s}\right)\frac{3}{2}\frac{V_d}{V_{dc}}\frac{1}{C\,s}} \quad \textbf{(92)}$$

5.3.3 Tuning of the controllers

Inner current controller

The closed loop transfer function of the inner current controller represented by equation (86) is equal to equation (30), which is the closed loop transfer function of the current control loop of the electrical machine. The only difference between the two transfer functions is that, in equation (86) the filter resistance ($\boldsymbol{R_f}$) and the filter inductance ($\boldsymbol{L_f}$) are considered, instead in equation (30) there are the stator resistance ($\boldsymbol{R}$) and the stator inductance ($\boldsymbol{L}$). This analogy allows to tune the PI-controllers (one for the *d*-axis and the other one for the *q*-axis) in the same way as it has been made in the paragraph 4.3.2 (using the **modulus optimum** method). The first step, the cancellation of the dominant pole (setting $\boldsymbol{T_i = \tau_f}$), it has been already made passing from equation (85) to equation (86). After which it is imposed the closed loop transfer function equal to 1 as high as possible in the frequency spectrum:

$$\boldsymbol{\left|M_{0,cc}(s)\right| = 1} \quad \textbf{(93)}$$

The procedure is the same of paragraph 4.3.2 and the following $\boldsymbol{k_p}$ and $\boldsymbol{k_i}$ are obtained:

$$\boldsymbol{k_p = \frac{\tau_f R_f}{2\,T}} \quad \textbf{(94)}$$

$\boldsymbol{k_i}$ can be obtained from $\boldsymbol{T_i}$:

$$\boldsymbol{k_i = \frac{R_f K_p}{L_f}} \quad \textbf{(95)}$$

Outer voltage controller

There are two poles at the origin in the open loop transfer function represented by equation (92), hence the modulus optimum method cannot be used and a different method is applied: the **symmetrical optimum**. The advantage of this method is the maximization of the phase margin ($\boldsymbol{\psi_m}$) which involves a system that can tolerate more delays (important characteristic for a control system). The phase margin of $\boldsymbol{h_{0,vc}}$ can be obtained from the following equation:

$$\boldsymbol{\langle h_{0,vc}\,(j\omega) = arctan(T_{iv}\omega) - 90° - arctan(T_{eq}\omega) - 90° = \psi_m - 180°} \quad \textbf{(96)}$$

$\langle \boldsymbol{h_{0,vc}}\,(\boldsymbol{j\omega})$ is the phase of $\boldsymbol{h_{0,vc}}\,(\boldsymbol{j\omega})$ expressed in degrees. The Nyquist-criterion imposes the stability of the control system for an open loop transfer function without poles in the right half plane, if the next two conditions are verified [28]:

$$\langle \boldsymbol{h_{0,vc}}\,(\boldsymbol{j\omega_c}) > -180° \tag{97}$$

$$\left|\boldsymbol{h_{0,vc}}\,(\boldsymbol{j\omega_{180}})\right| < \mathbf{1} = \mathbf{0}[\mathbf{dB}] \tag{98}$$

Therefore, the phase margin ($\boldsymbol{\psi_m}$) is defined as the negative phase that can be added when $\left|\boldsymbol{h_{0,vc}}\,(\boldsymbol{j\omega})\right| = \mathbf{1} = \mathbf{0}\,[\boldsymbol{dB}]$ (at the crossover frequency $\boldsymbol{\omega_c}$) without compromise the stability of the system. As written in [38] for a good dynamic response the phase margin must be higher than 45°.

$\boldsymbol{\psi_m}$ is maximized and $\boldsymbol{\omega_c}$ extracted as following [28]:

$$\frac{\boldsymbol{d\psi_m}}{\boldsymbol{d\omega_c}} = \frac{\boldsymbol{T_{iv}}}{\mathbf{1}+(\boldsymbol{T_{iv}\omega_c})^2} - \frac{\boldsymbol{T_{eq}}}{\mathbf{1}+(\boldsymbol{T_{eq}\omega_c})^2} = \mathbf{0} \tag{99}$$

$$\boldsymbol{\omega_c} = \frac{\mathbf{1}}{\sqrt{\boldsymbol{T_{iv}T_{eq}}}} \tag{100}$$

Substituting the (100) into (96) the phase margin is equal to [28]:

$$\boldsymbol{\psi_m} = \mathbf{arctan}\left(\boldsymbol{T_{iv}}\frac{\mathbf{1}}{\sqrt{\boldsymbol{T_{iv}T_{eq}}}}\right) - \mathbf{arctan}\left(\boldsymbol{T_{eq}}\frac{\mathbf{1}}{\sqrt{\boldsymbol{T_{iv}T_{eq}}}}\right) \tag{101}$$

$$\boldsymbol{\psi_m} = \mathbf{arctan}\left(\sqrt{\frac{\boldsymbol{T_{iv}}}{\boldsymbol{T_{eq}}}}\right) - \mathbf{arctan}\left(\sqrt{\frac{\boldsymbol{T_{eq}}}{\boldsymbol{T_{iv}}}}\right) \tag{102}$$

It is defined [28]:

$$\boldsymbol{\theta} = \boldsymbol{arctan}\left(\sqrt{\frac{\boldsymbol{T_{iv}}}{\boldsymbol{T_{eq}}}}\right) \tag{103}$$

Hence [28]:

$$\boldsymbol{arctan}\left(\sqrt{\frac{\boldsymbol{T_{eq}}}{\boldsymbol{T_{iv}}}}\right) = \mathbf{90°} - \boldsymbol{\theta} \tag{104}$$

Therefore, inserting equation (104) and (103) into (102), the next equation is obtained:

$$\boldsymbol{\psi_m} = \boldsymbol{\theta} - (\mathbf{90°} - \boldsymbol{\theta}) = \mathbf{2}\boldsymbol{\theta} - \mathbf{90°} \tag{105}$$

The sine of the phase margin can be represented as [28]:

$$\boldsymbol{sin}(\boldsymbol{\psi_m}) = \mathbf{sin}(\mathbf{2}\boldsymbol{\theta} - \mathbf{90°}) = -\mathbf{cos}\,(\mathbf{2}\boldsymbol{\theta}) \tag{106}$$

From equation (103) and using equation (106):

$$\sqrt{\frac{T_{iv}}{T_{eq}}} = \boldsymbol{tan(\theta)} = \sqrt{\frac{\mathbf{1-cos(2\theta)}}{\mathbf{1+cos(2\theta)}}} = \sqrt{\frac{\mathbf{1+sin(\psi_m)}}{\mathbf{1-sin(\psi_m)}}} \quad \textbf{(107)}$$

Hence, the time constant of the controller can be written as [28]:

$$\boldsymbol{T_{iv} = T_{eq}\frac{1+sin(\psi_m)}{1-sin(\psi_m)} = a^2 T_{eq}} \quad \textbf{(108)}$$

$\boldsymbol{a}$ is a constant calculated from the phase margin. When $\boldsymbol{\psi_m = 0° \rightarrow a = 1}$. Therefore it is intuitive that the system is stable when $\boldsymbol{a \geq 1}$. But, if it is wanted a satisfactory dynamic response, $\boldsymbol{\psi_m}$ and $\boldsymbol{a}$ should be:

$$\boldsymbol{\psi_m} > 45° \rightarrow a > 2.41 \quad \textbf{(109)}$$

As it has been said previously: $\boldsymbol{\left|h_{0,vc}(j\omega)\right| = 1}$ at the crossover frequency. Therefore, substituting $\boldsymbol{s = j\omega}$ into equation (92), it is obtained [28]:

$$\boldsymbol{\left|h_{0,vc}(j\omega_c)\right| = \frac{3\,k_{pv}\,V_d}{2\,V_{dc}} \frac{|1+T_{iv}\omega_c j|}{|T_{iv}\omega_c j - T_{iv}T_{eq}\omega_c^2|} \left|\frac{1}{j\omega_c C}\right| = 1} \quad \textbf{(110)}$$

$$\boldsymbol{\left|h_{0,vc}(j\omega_c)\right| = \frac{3\,k_{pv}\,V_d}{2\,V_{dc}} \frac{\sqrt{1^2+(T_{iv}\,\omega_c)^2}}{\sqrt{(T_{iv}\omega_c)^2+\left(-T_{iv}T_{eq}\omega_c^2\right)^2}} \frac{1}{\omega_c C} = 1} \quad \textbf{(111)}$$

$$\boldsymbol{\left(\frac{3\,k_{pv}\,V_d}{2\,V_{dc}\omega_c C}\right)^2 = \frac{(T_{iv}\omega_c)^2+\left(-T_{iv}T_{eq}\omega_c^2\right)^2}{(1^2+(T_{iv}\omega_c)^2)}} \quad \textbf{(112)}$$

Inserting equation (100) and after several simplifications:

$$\boldsymbol{\left(\frac{3\,k_{pv}\,V_d}{2\,V_{dc}\omega_c C}\right)^2 = \frac{\frac{T_{iv}}{T_{eq}}+1}{1+\frac{T_{iv}}{T_{eq}}} = 1} \quad \textbf{(113)}$$

Therefore the proportional gain obtained is equal to [28]:

$$\boldsymbol{K_{pv} = \frac{2}{3}\frac{V_{dc}}{V_d}\omega_c C = \frac{2}{3}\frac{V_{dc}}{V_d}\frac{1}{\sqrt{T_{iv}T_{eq}}}C} \quad \textbf{(114)}$$

5.4 Simulation, results and final consideration

The integrated wave-to-wire model with the grid connection illustrated in figure 53 has been simulated in MATLAB-Simulink, the results are shown in this paragraph. The Simulink models, that have been used, are illustrated in Appendix B. In figure 53 it can be seen that the wave-to-wire model, up to the DC link, is equal to the model used in the simulations of paragraph 4.4. Indeed only the grid connection has been added in the model with utilization of a capacitor, a three-phase inverter and a grid filter. The medium energy sea state is tested with the damping coefficient equals to 4300000 kg/s. In the next table the data of the grid connection, which have been used in the simulation, are shown.

Table 12 – Data of the grid connection

Quantity	Value
peak amplitude of the grid voltage, Vg	230 V
grid frequency, f	50 Hz
swiching frequency of the inverters, f_s	2000 Hz
filter resistance, R_f	0.028 Ω
filter inductance, L_f	0.0009 H
capacity of the capacitor, C	0.033 F
DC link voltage, V_{dc}	800 V

The data of the generator tested are shown in table 8, they are the same data of the simulations of the chapter 4. Therefore the power limit is 100 kW and the module of the torque limit 850 Nm. Both the inverters are considered ideal and the switching frequency of the grid side inverter has been chosen equal to the switching frequency of the inverter that controls the PMSG. The filter resistance, the filter inductance, the capacity of the capacitor and the DC link voltage have been chosen in accordance with [34]. The goals of the simulation of the wave-to-wire model with the grid connection are: find the trend over the time of several important quantities of the system, prove that the power generated by the PTO can be effectively injected into the grid and prove that the current is injected into the grid with a unity power factor. The simulation time of 50 s has been considered enough to prove the goals. In figure 60 the trend over the time of the position of the buoy, the torque of the generator, the generator speed, the mechanical power, the DC link voltage and the grid current are plotted.

Figure 60 – Trend over the time of important magnitudes of the wave-to-wire model with grid connection

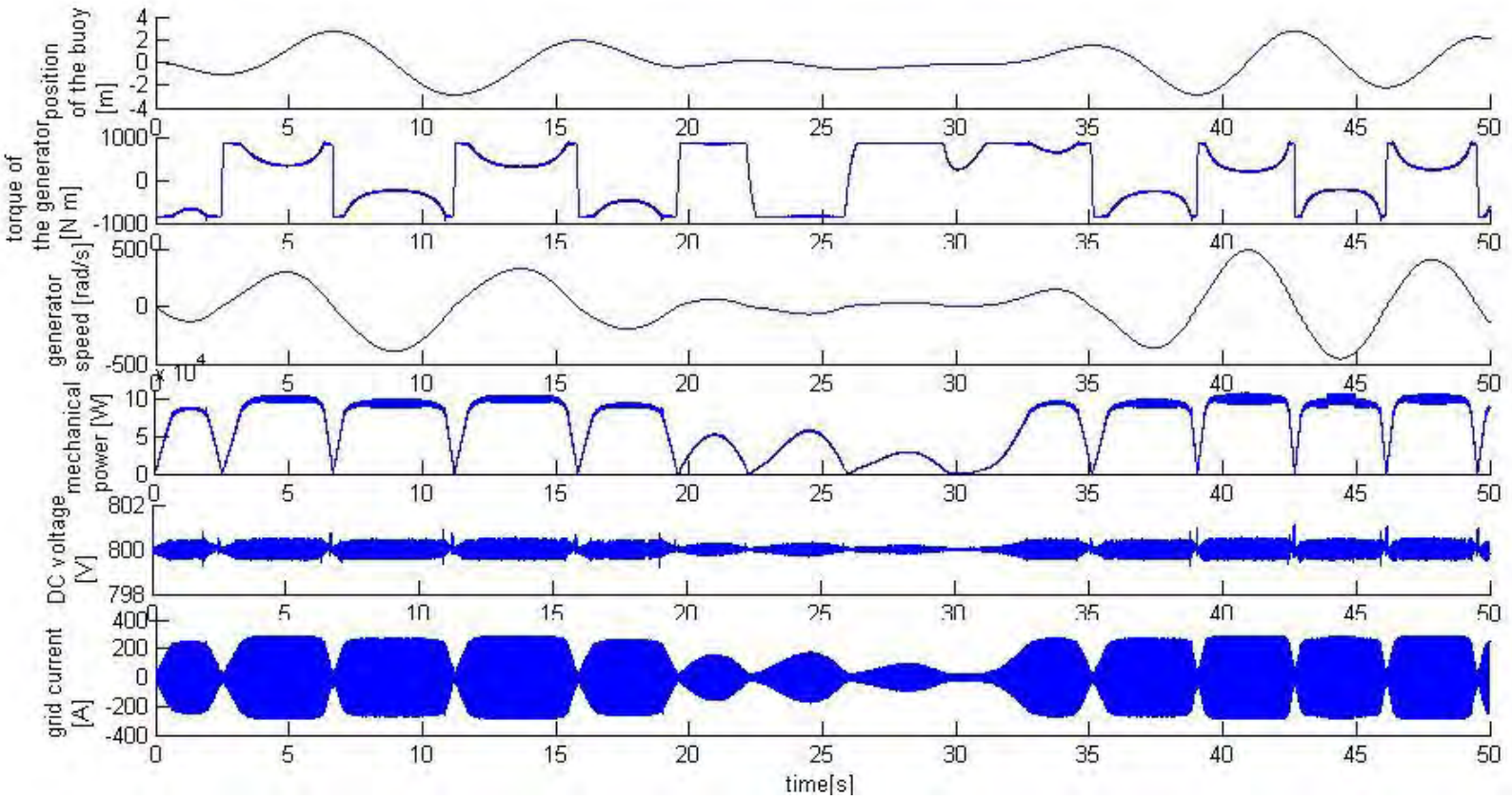

As in [34] it can be noticed in figure 60 a correlation between the DC link voltage, the grid current and the low-frequency oscillations of the sea waves. It can be seen that the oscillations of the generator speed correspond to fluctuations in the DC link voltage and in the grid current waveform. Also the trend over the time of the generator torque, generator speed and mechanical power are plotted. As expected the torque and the speed of the generator have always the same sign and the mechanical power produced is always positive. It can be seen clearly the influence of the torque limit and the power limit on the trend of the waveforms. It is true that there are fluctuations in the DC link voltage waveform, but they are low compared 800 V. Therefore the DC link voltage of the capacitor can be considered roughly constant proving that the DC voltage control is working properly and that the power generated by the PTO is directly injected into the grid (a constant DC link voltage involves a constant energy storage over the time in the capacitor).

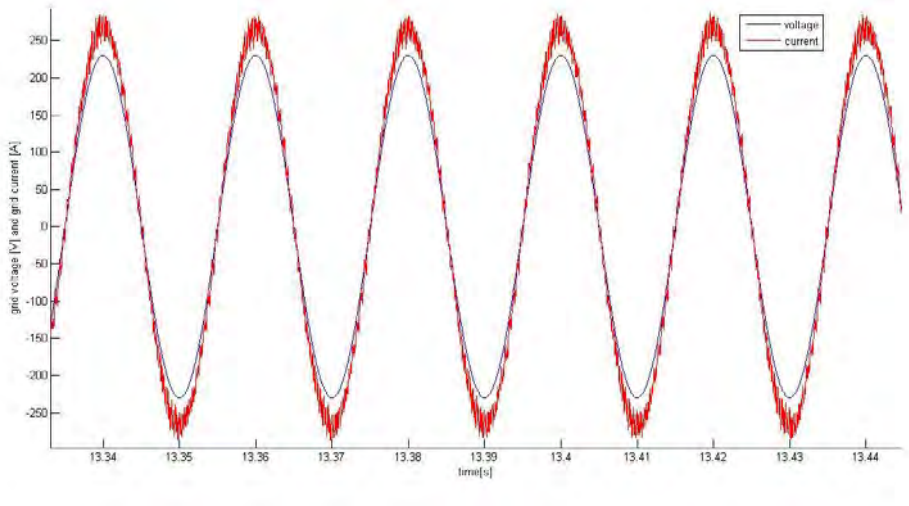

Figure 61- Detail of the grid voltage and grid current over the time

In figure 61 the voltage and the current of phase *a* at the grid section are plotted in detail in order to check the power factor. The red line represents the current and the blue one the voltage. It can be seen that the two waveforms are sinusoidal and especially in phase. This proves that the current has been successfully injected into the grid with a unity power factor as wanted.

6. CONCLUSIONS AND FURTHER WORKS

6.1 Conclusions

In the first part of the thesis the goal was to analyze the behaviour of the WEC adopted considering an ideal PTO (without losses), and testing the expected control performance as a preliminary step to design a specific PTO. The control strategy used is the passive loading and the low, medium and high energy cases are the reference sea states tested for 900 s, in order to get an overview of the system operation on all the different sea conditions. Several power limits (75kW, 100kW and 200kW), which allow to obtain a more realistic behaviour of the WEC, have been tentatively applied. The average mechanical power extracted and peak to average power ratio obtained for each case imply the following considerations. All the power limits tested are not convenient for a location with many low energy sea states, and due to the high values of the peak to average power ratios obtained, a reduction of the power limit is suggested. If in the scatter diagram of the location the medium energy sea states prevail over the low and the high energy ones, as it was mostly assumed in this thesis, 100 kW as power limit is the most convenient. Finally whether in a specific location the high energy sea states prevail over the medium and low energy ones, the most convenient case is 200 kW as power limit.

The goal of the second part of the thesis was to test the wave-to-wire model of the considered point absorber WEC for each energy sea state. 100 kW is the power limit adopted and a corresponding SMPMSG with 80 kW as rated power has been chosen. Also 850 Nm as module of the torque limit, corresponding to the maximum torque of the electrical machine, is applied and implemented in the model. The addition of the power limit involves not only a lower peak to average power ratio, but also less fluctuation in power production and the utilization of an electrical machine with a higher over-speed ratio. For this reason, the generator chosen has a high overspeed ratio and a wide constant power region. It has to work most of the time in the field-weakening operation region, therefore a field-weakening control needs to be used, as shown in the simulations. The torque of the generator has been controlled using an ideal three phase inverter and an electric drive model. A real time-model which calculates the total losses of the PMSG has been made and simulated in the low, medium and high energy sea state respectively. The $\boldsymbol{B_L}$ coefficient tested for each energy case is the one that allows to obtain the maximum average electrical power. The average efficiencies obtained are equal to: 0,881 for the low energy case, 0.904 for the medium energy case and 0.909 for the high energy case. Hence it can be said that, with the considered PTO design, the increment of the energy content in the sea state implies an increase of the average efficiency of the wave-to-wire model of the point absorber WEC.

The grid connection of the wave-to-wire model of the point absorber WEC was the last goal of this thesis, it has been made using the voltage oriented vector control. In order to complete the grid connection from the DC-link voltage an ideal three phase inverter, a grid side filter and a capacitor have been used. The last one is implemented in the model with the aim to maintain a constant DC link voltage during the production of electric energy. For 50 s the wave-to-wire model of the WEC has been tested for the medium energy sea state with the $\boldsymbol{B_L}$ coefficient which allows to obtain the maximum average electrical power. The grid current is injected into the grid at grid frequency and in phase with the grid voltage, therefore there is not exchange of reactive power at the converter output as wanted. The simulations prove that all the control loops implemented are working properly and that the power generated by the PTO is directly injected into the grid as desired, inasmuch the DC link voltage is maintained nearly constant. At last the trend over the time of important electrical quantities of the system has been obtained and analyzed. It is proved and confirmed a correlation between the grid current and the low-frequency oscillations of the sea waves. As a matter of fact the oscillations of the generator speed correspond to low-frequency fluctuations in the grid current waveform.

6.2 Further works

- The wave-to-wire model of the WEC works correctly for the passive loading control strategy. It would be interesting to test (and in case refine) the model for operation with other control strategies, for instance for the complex-conjugate (reactive) control. To do it the field-weakening control has to be modified and several changes has to be introduced in the model.
- The grid connection has been made without consider the resistance and inductance of the eventual transmission line until the point of common coupling. It would be interesting to include them in the model and study the interaction of the grid, for example with different grid strengths.
- In this thesis a single inductance filter at the grid side has been used with the goal to approximate sinusoidal conditions. If it is wanted a further reduction of the harmonic content, the sizing of the R-L filter or of a different filter could be studied. As it is explained in [39] the utilization of an LCL-filter, two inductors in series and a shunt capacitor, could be another solution.
- An outer reactive power controller was not treated in this thesis. It could be introduced on the grid side converter control system to supply the q-axis reference current. The strategy is similar to the outer voltage controller applied in this thesis.
- In this thesis the wave-to-wire model of the WEC has been tested for three representative energy sea states. It would be very interesting to take into

consideration a scatter diagram of a specific location (or several locations) and calculate the yearly electric energy produced using the wave-to-wire model developed.

- In the model the two power electronics devices have been considered with ideal switches (without losses). The utilization in the simulation of two real IGBT power electronics converters could be an interesting further work. In this way if the losses of the two inverter are added to the generator losses, a more realistic behaviour of the wave-to-wire model of the WEC would be obtained.

Bibliography:

[1] K.Burman, A. Walker, "Ocean Energy Technology Overview", *Prepared for the U.S. Department of Energy - Office of Energy Efficiency and Renewable Energy - Federal Energy Management Program*, July 2009.

[2] International Energy Agency, "World Energy Outlook", 2010.

[3] Clemente "Wave Energy in Europe: current status and perspectives", 2002

[4] H. Andrews e N. Jelly, "Energy Science: Principles, Technologies and Impacts", *Oxford: Oxford University Press*, 2007.

[5] A.F. de O. Falcao, "Wave energy utilization: A review of the technologies", *Renewable and Sustainable Energy Reviews*, n. 14, pp. 899-918, 2010.

[6] B. Czech, P. Bauer "Wave Energy Converter Concepts, Design Challenges and Classification'' *IEEE INDUSTRIAL ELECTRONICS MAGAZINE,* June 2012.

[7] B. Drew, A. R. Plummer, M. N. Sahinkaya "A review of wave energy converter technology", *Department of Mechanical Engineering, University of Bath (UK),* 2009.

[8] Lewis T., "A strategic review of the wave energy resource in Ireland'', "Wave Energy-Moving towards commercial viability'', *IMECHE Seminar*, London (UK), 1999.

[9] J.Lucas, S.Salter, J. Cruz, J. Taylor, I. Bryden, "Performance optimisation of a modified Duck through optimal mass distribution", *the 8th European Wave and Tidal Energy Conference*, Uppsala, Sweden, 2009.

[10] D. Vicinanza, L.Cappietti, V.Ferrante, P. Contestabile "Estimation of the wave energy in Italian Offshore", Journal of Coastal Research, 2011.

[11] A. Bozzetto, "Modeling, control and performance assessment of a Wave Energy Converter equipped with an All-Electric Power Take-Off*", Master Thesis in Electrical Engineering*, supervisor: N. Bianchi, co-supervisor: E. Tedeschi, Università degli studi di Padova, NTNU, 2013.

[12] Skyne Holcombe Henley, "Ocean Energy in Europe's Atlantic Arc, an overview of policy and market conditions in Denmark, France, Ireland, Portugal, Spain and the United Kingdom", *Co-funded by the Intelligent Energy Europe (Programme of the EU),* March 2013.

[13] "Enel Green Power's wave energy converter developed by 40south energy: second test phase under way", Press Release*, www.enel.com* , 31th January 2014.

[14] L. Alberti, E. Tedeschi, N. Bianchi, M. Santos and F. Alessandro, "Effect of the generator sizing on wave energy converter", *The international Journal for Computation and Mathematics in Electrical and Electronic Engineering*, vol.32, no.1, pp.233-247, 2013.

[15] W. Cummins, "The impulse response function and ship motions", *Schiffstechnik,* n. 1662, pp. 101-9, 1962.

[16] A. Bozzetto, E. Tedeschi, "Wave Power Extraction with Constrained Power Take-Off: Single Capture vs. Double Capture Point Absorbers", *Ninth International Conference on Ecological Vehicles and Renewable Energies (EVER),* 2014.

[17] E. Tedeschi e M. Molinas, "Wave-to-wave buoys control for improved power extraction under electro-mechanical constraints" *Suitable Energy Technologies (ICSET), 2010 IEEE International Conference,* 2010

[18] M. M.S., B. H. e L. Louze, "Sliding Mode Control (SMC) Of Permanent Magnet Synchronous Generators (PMSG)'' *Energy Procedia,* pp. 43-52, 2012.

[19] I. Boldea, ''Synchronous Generators'', Polytechnical Institute, Temisoara, Romania: Taylor & Francis Group, 2006.

[20] Richard C. Dorf, ''The Engineering Handbook, Second Edition'', CRC Press, 2004

[21] M. Chinchilla, S. Arnaltes, J. C. Burgos, ''Control of Permanent-Magnet Generators Applied to Variable-Speed Wind-Energy Systems Connected to the Grid'', *IEEE Transactions on Energy Convertion, march 2006.*

[22] E. Tedeschi, M. Molinas, M. Carraro, P. Mattavelli, "Analysis of power extraction from irregular waves by all-electric power take off", *Energy Conversion Congress and Exposition (ECCE), IEEE,* 2010.

[23] M. W. H., «Sea Spectra Revisited,» *Marine Technology,* vol. 36, n. 4, pp. 211-227, 1999.

[24] K. Nielsen e T. Pontes, «Report T02-1.1 OES IA Annex II Task 1.1 Generic and Site-related Wave Energy Data,» September 2010.

[25] J. Sjolte, I. Bjerke, E. Hjetland, G. Tjensvoll and F. Olsen, "All-Electric Wave Energy Power Take Off Generator Optimized by High Overspeed", *European Wave and Tidal Energy Conference*, EWTEC, 2011.

[26] Ching-Tsai Pan, Jen-Horng Liaw, “A Robust Field-Weakening Control Strategy for Surface-Mounted Permanent-Magnet Motor Drives”, *IEEE Transactions on Energy Convertion,* vol. 20, no.4, December 2005.

[27] J.Sjolte, C.M. Sandvik, E. Tedeschi, M. Molinas, ”Exploring the Potential for Increased Production from the Wave Energy Converter Lifesaver by Reactive Control”, *ENERGIES,* ISSN 1996-1096*,* 2013.

[28] J. C. Ulvin, “Grid Integration of the Wave Energy Converter Bolt2, Control of the Grid Side Converter with Energy Storage”, *Master Thesis in Energy and Environmental Engineering,* supervisor: M. Molinas, NTNU, 2012.

[29] Silverio Bolognani, “Dispense di azionamenti elettrici”, Padova, 2005.

[30] C. Mi, G. R. Slemon, R. Bonert, “Modeling of Iron Losses of Permanent-Magnet Synchronous Motors”, *IEEE TRANSACTIONS ON INDUSTRY APPLICATIONS,* VOL. 39, NO. 3, 2003.

[31] C. C. Mi, G. R. Slemon, R. Bonert, “Minimization of Iron Losses of Permanent Magnet Synchronous Machines”, *IEEE TRANSACTIONS ENERGY CONVERTION,* VOL. 2, NO. 1, march 2005

[32] G. Someda, “Elementi di costruzione delle macchine elettriche : principi di similitudine geometrica, sovrariscaldamento, i materiali usati nelle costruzioni elettromeccaniche, trasformatori ... ”, *Bologna: Casa Editrice Prof. Riccardo Patron*, 1954.

[33] J. Goss, M. Popescu, D.Staton, ”Implications of real-world drive cycles on efficiencies and life cycle costs of two solutions for HEV traction: Synchronous PM motor vs Copper Rotor-IM”, *www.motor-design.com*, 11th October 2012, Stuttgart (Germany).

[34] E. Tedeschi, M. Carraro, M. Molinas, P. Mattavelli “Effect of Control Strategies and Power Take-Off Efficiency on the Power Capture From Sea Waves”, *IEEE TRANSACTIONS ON ENERGY CONVERTION,* VOL.26, NO. 4, 2011.

[35] South West of England Regional Development Agency, “WEC Connection Specification, Wave Hub” Revision number 4, 2011.

[36] “Park, Inverse Park and Clarke, Inverse Clarke Transformations MSS Software Implementation”, www.microsemi.com, Unser Guide.

[37] C. Bajracharya, “Control of VSC-HVDC Wind Power”, Master’s Thesis, NTNU, 2008.

[38] Ned Mohan, “Electric Drives - An Interactive Approach”, MNPERE, Minneapolis,2003.

[39] V. Valdivia, J. Pleite, C. Gonzalez, R. A. Salas, “New approach to integrate an LCL filter and a transformer for grid connected converters following a simple design procedure”, *The 33rd Annual Conference of the IEEE Industrial Electronics Society (IECON)*, Nov. 5-8, 2007, Taipei, Taiwan.

[40] E. Tedeschi, M. Molinas, "Impact of control strategies on the rating of electric power take off for wave energy conversion." *Industrial Electronics (ISIE) Interational Symposium on. IEEE*, 2010.

[41] E. Tedeschi , M. Molinas, "Tunable control strategy for wave energy converters with limited power takeoff rating" *IEEE transactions on industrial electronics,* vol. 59 , no.10, October 2012.

[42] E. Tedeschi, M. Molinas, "Control strategy of wave energy converters optimized under power electronics rating constraints" *3rd international Conference on Ocean Energy (ICOE10), Bilbao (SP)*, 2010.

Appendix A

Clark and Park transformation

The dq0-transformation (or direct-quadrature-zero) is the Clark transformation followed by the Park transformation. It is a mathematical transformation which simplifies the analysis of a three-phase circuit. If there is a balanced three-phase circuit the dq0-transformation converts the three sinusoidal signals into two constant signal (and the zero-axis component is equal to 0). It is frequently used for the control of a three phase electrical machine or a three phase inverter.

The Clark transformation involves the projection of three phase quantities (*abc*) onto *αβ* (two stationary axes) [28]:

$$\begin{bmatrix} X_\alpha \\ X_\beta \end{bmatrix} = k \begin{bmatrix} 1 & -\frac{1}{2} & -\frac{1}{2} \\ 0 & \frac{\sqrt{3}}{2} & -\frac{\sqrt{3}}{2} \end{bmatrix} \begin{bmatrix} X_a \\ X_b \\ X_c \end{bmatrix} \quad \textbf{(A.1)}$$

So it can be obtained:

$$X_\alpha = k\,(X_a - \frac{1}{2}X_b - \frac{1}{2}X_c) \quad \textbf{(A.2)}$$

$$X_\beta = k\,(\frac{\sqrt{3}}{2}X_b - \frac{\sqrt{3}}{2}X_c) \quad \textbf{(A.3)}$$

k is a constant and X_a, X_b, X_c are the three-phase quantities (for instance the currents or the voltages).

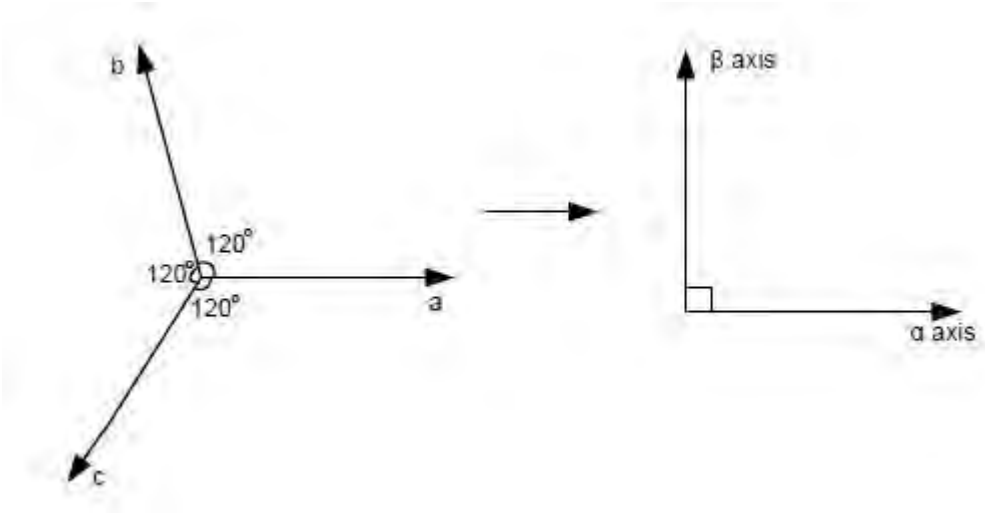

Figure 62 – Clark transformation from the *abc* stationary frame to the *αβ* orthogonal stationary frame [36].

The transformation from $\alpha\beta$ stationary axes to the dq rotating axis is called Park transformation [28]:

$$\begin{bmatrix} X_d \\ X_q \end{bmatrix} = \begin{bmatrix} \cos\theta & \sin\theta \\ -\sin\theta & \cos\theta \end{bmatrix} \begin{bmatrix} X_\alpha \\ X_\beta \end{bmatrix} \quad \textbf{(A.4)}$$

This gives:

$$X_d = X_\alpha \cos\theta + X_\beta \sin\theta \quad \textbf{(A.5)}$$

$$X_q = -X_\alpha \sin\theta + X_\beta \cos\theta \quad \textbf{(A.6)}$$

θ is the rotation angle and is shown in the next figure.

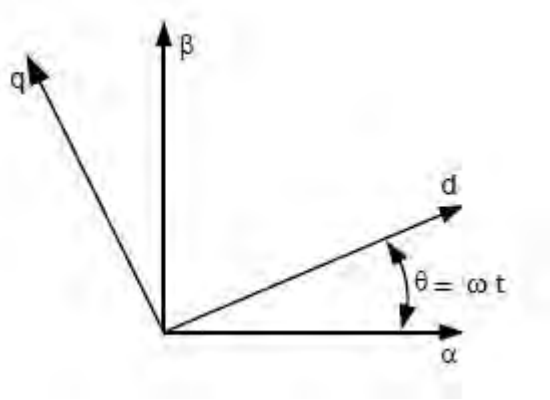

Figure 63 – Park transformation [36]

The total transformation from the *abc* stationary reference frame to the *dq* rotating frame is equal to [28]:

$$\begin{bmatrix} X_d \\ X_q \end{bmatrix} = k \begin{bmatrix} \cos\omega t & \cos\left(\omega t - \frac{2}{3}\pi\right) & \cos\left(\omega t + \frac{2}{3}\pi\right) \\ -\sin\omega t & -\sin\left(\omega t - \frac{2}{3}\pi\right) & -\sin\left(\omega t + \frac{2}{3}\pi\right) \end{bmatrix} \begin{bmatrix} X_a \\ X_b \\ X_c \end{bmatrix} \quad \textbf{(A.7)}$$

This gives:

$$X_d = k\left(X_a \cos\omega t + X_b \cos\left(\omega t - \frac{2}{3}\pi\right) + X_c \cos\left(\omega t + \frac{2}{3}\pi\right)\right) \quad \textbf{(A.8)}$$

$$X_q = k\left(-X_a \sin\omega t - X_b \sin\left(\omega t - \frac{2}{3}\pi\right) - X_c \sin\left(\omega t + \frac{2}{3}\pi\right)\right) \quad \textbf{(A.9)}$$

If three-phase balanced voltages are taken into account [28]:

$$V_a = V \cos\omega t \quad \textbf{(A.10)}$$

$$V_b = V \cos\left(\omega t - \frac{2}{3}\pi\right) \quad \textbf{(A.11)}$$

$$V_c = V \cos\left(\omega t + \frac{2}{3}\pi\right) \quad \textbf{(A.12)}$$

$\boldsymbol{V}$ is the peak amplitude. If $\boldsymbol{k}$ is equal to 2/3, the following voltages are obtained in the $\boldsymbol{dq}$ rotating frame [28]:

$$\boldsymbol{V_d = V} \quad \textbf{(A.13)}$$

$$\boldsymbol{V_q = 0} \quad \textbf{(A.14)}$$

This is the voltage invariant transformation and, as it can be seen in equation (A.13) the d-axis voltage is constant and equal to $\boldsymbol{V}$.

If $\boldsymbol{k}$ is equal to $\sqrt{\frac{2}{3}}$ the power-invariant transformation is applied. It ensures which the *dq*-power is equal to the *abc*-power.

In this thesis **k** =2/3 and the voltage invariant transformation has been used.

Appendix B

Simulink models

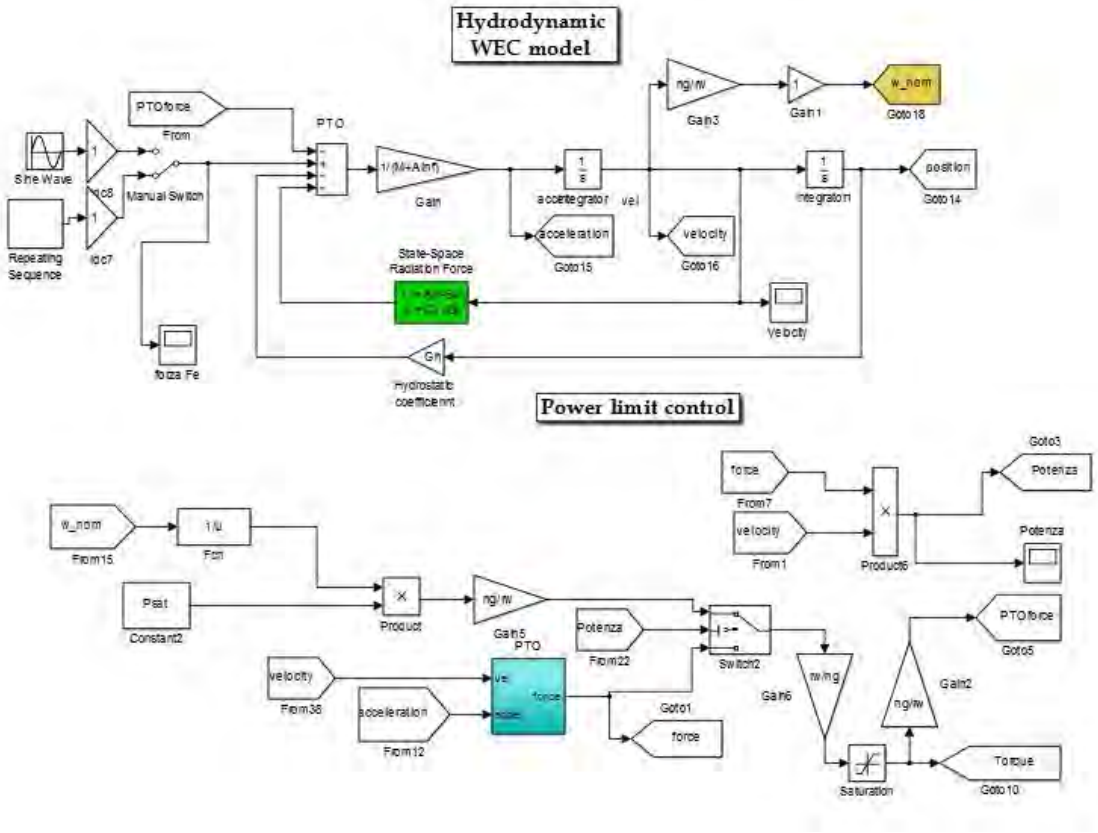

Figure 64 – Simulink model with the generator considered ideal with power limit and torque limit applied simultaneously

Figure 65 – Simulink model of the control of the generator

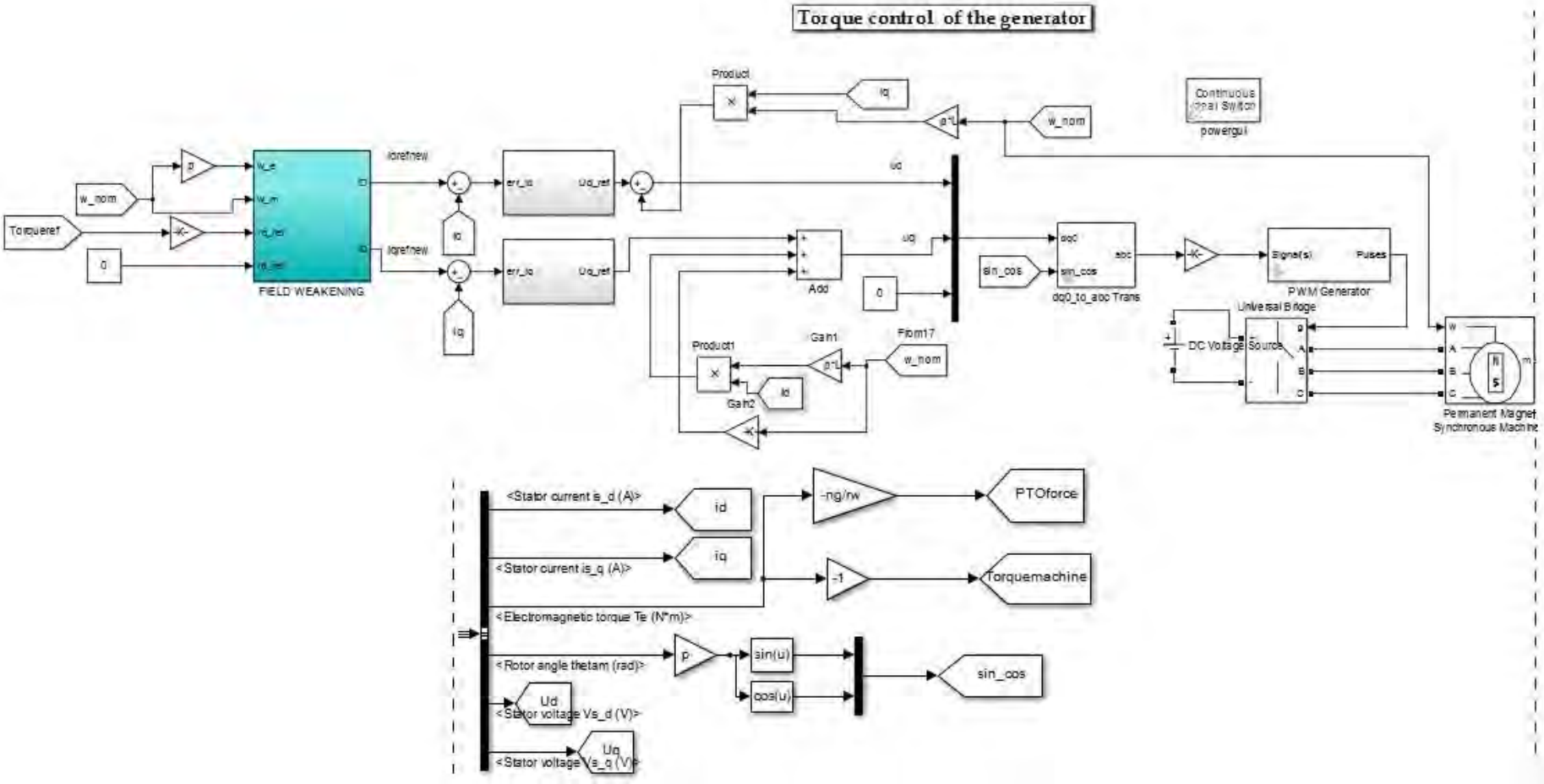

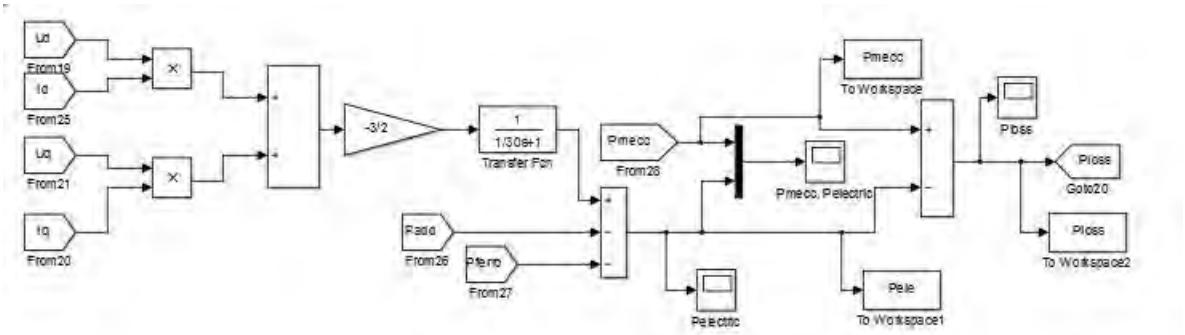

Figure 66 – Simulink model showing the calculation of the electrical power and the total losses of the generator

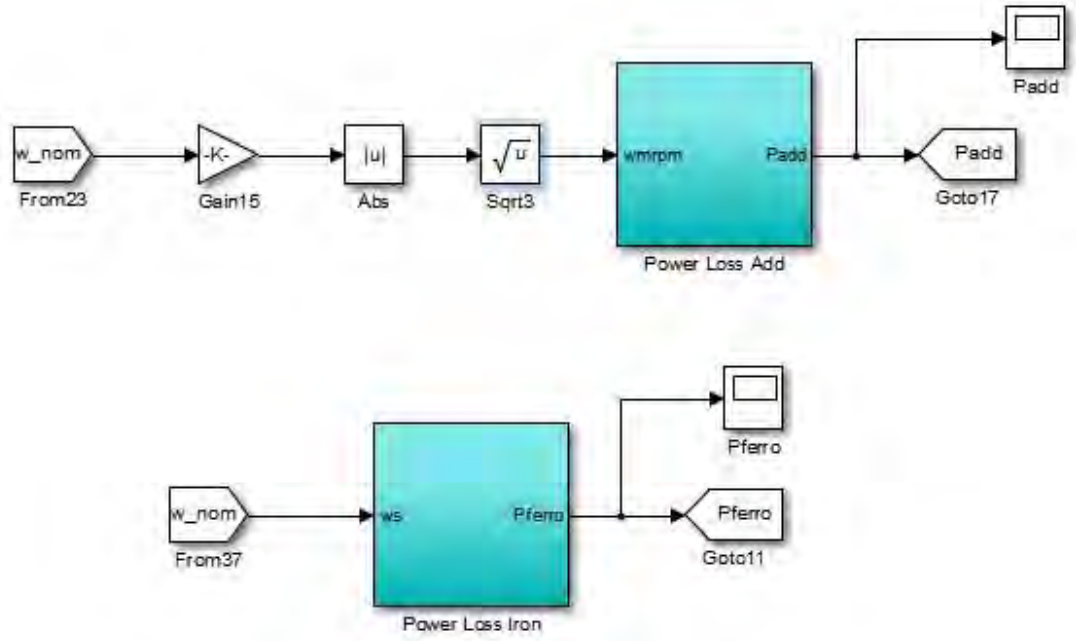

Figure 67 – Simulink blocks that calculate the mechanical and the iron losses

Figure 68 - Simulink model of the grid connection from the DC link

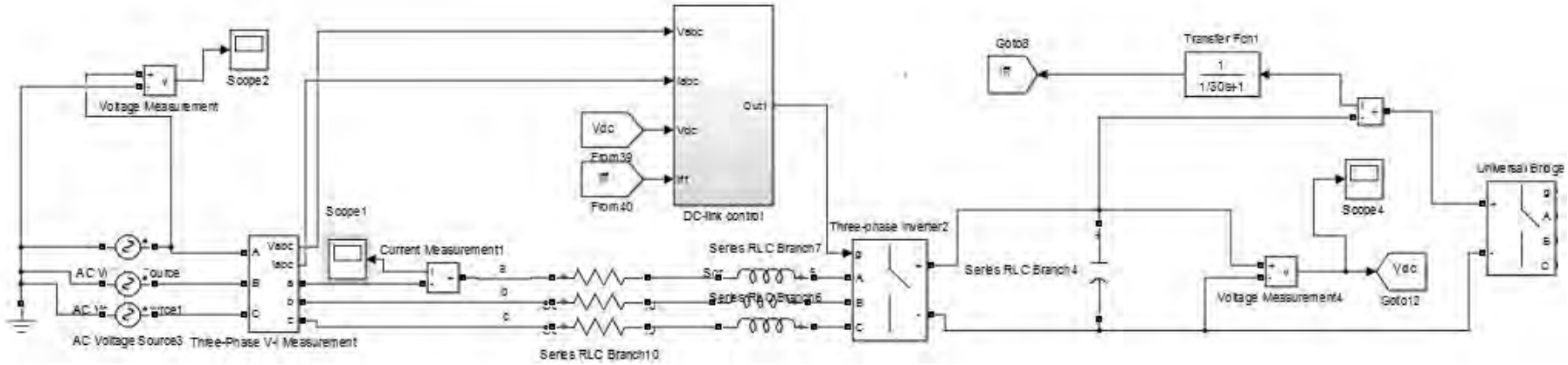

Figure 69 – Simulink subsystem of the DC-link control